


Winter 2017

Design, modeling, fabrication, and testing of a multistage micro gas compressor with piezoelectric unimorph diaphragm and passive microvalves for microcooling applications

Shawn Thanhson Le
Louisiana Tech University

Follow this and additional works at: <https://digitalcommons.latech.edu/dissertations>

 Part of the [Other Electrical and Computer Engineering Commons](#), and the [Other Mechanical Engineering Commons](#)

Recommended Citation

Le, Shawn Thanhson, "" (2017). *Dissertation*. 75.
<https://digitalcommons.latech.edu/dissertations/75>

This Dissertation is brought to you for free and open access by the Graduate School at Louisiana Tech Digital Commons. It has been accepted for inclusion in Doctoral Dissertations by an authorized administrator of Louisiana Tech Digital Commons. For more information, please contact digitalcommons@latech.edu.

**DESIGN, MODELING, FABRICATION, AND TESTING OF A MULTISTAGE
MICRO GAS COMPRESSOR WITH PIEZOELECTRIC UNIMORPH
DIAPHRAGM AND PASSIVE MICROVALVES FOR MICROCOOLING
APPLICATIONS**

by

Shawn Thanhson Le, B.S., M.S.

A Dissertation Presented in Partial Fulfillment
of the Requirements of the Degree
Doctor of Philosophy

COLLEGE OF ENGINEERING
LOUISIANA TECH UNIVERSITY

February 2017

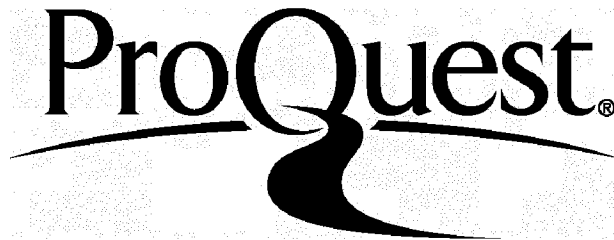
ProQuest Number: 10612795

All rights reserved

INFORMATION TO ALL USERS

The quality of this reproduction is dependent upon the quality of the copy submitted.

In the unlikely event that the author did not send a complete manuscript and there are missing pages, these will be noted. Also, if material had to be removed, a note will indicate the deletion.



ProQuest 10612795

Published by ProQuest LLC(2017). Copyright of the Dissertation is held by the Author.

All rights reserved.

This work is protected against unauthorized copying under Title 17, United States Code.
Microform Edition © ProQuest LLC.

ProQuest LLC
789 East Eisenhower Parkway
P.O. Box 1346
Ann Arbor, MI 48106-1346

LOUISIANA TECH UNIVERSITY

THE GRADUATE SCHOOL

NOVEMBER 10, 2016

Date

We hereby recommend that the dissertation prepared under our supervision by

Shawn Thanhson Le

entitled Design, Modeling, Fabrication, and Testing of a Multistage

Micro Gas Compressor with Piezoelectric Unimorph Diaphragm and Passive

Microvalves for Microcooling Applications

be accepted in partial fulfillment of the requirements for the Degree of

Doctor of Philosophy Engineering

[Signature]

Supervisor of Dissertation Research

[Signature]

Head of Department

Engineering

Department

Recommendation concurred in:

[Signature]

[Signature]

[Signature]

[Signature]

Advisory Committee

Approved:

[Signature]

Director of Graduate Studies

Approved:

[Signature]

Dean of the Graduate School

[Signature]

Dean of the College

ABSTRACT

This dissertation investigates the development of a multistage micro gas compressor utilizing multiple pump stages cascaded in series to increase the pressure rise with passive microvalves and piezoelectric unimorph diaphragms. This research was conducted through modeling, simulation, design, and fabrication of the microcompressor and its components. A single-stage and a two-stage microcompressor were developed to demonstrate and compare the performance and effectiveness of using a cascaded multistage design.

Steady fluid flow through static microvalves structure was studied to gain insight on its gas flow dynamics and characteristics. Transient analysis combined with the structure's interaction was investigated with an analytical model and FEM model. The static analysis and transient analysis enabled lumped model parameter extraction for modeling and simulations. The transient FEM solution of the microvalve fluid-structure interaction (FSI) allows for extraction of the damping ratio for the lumped model. The microvalves were fabricated with MEMS microfabrication methods and integrated into a machined microcompressor housing. Study from the simulation of the microvalve fluid-structure dynamics in Simulink showed the frequency of the microvalves, at which frequency the microvalve is more prone to leakage. Simulation indicated that the reverse

leakage from the sealing of the microvalve can have a significant impact on the pressure rise performance of the compressor.

A model of the single- and the two-stage microcompressor were developed with Simulink to observe the dynamics and performance of the multistage microcompressor. The simulation shows the dead volume between the two chambers to decrease in the overall pressure rise of the multistage microcompressor. Operating scenarios with different frequency and in phase and out of phase actuation between stages were simulated to understand the dynamics and performance of the multistage design. The fabricated single- and two-stage microcompressor produced a maximum pressure rise of 10 kPa and 18 kPa, respectively, and a maximum flow rate of 32 sccm for both. To obtain these maximum pressure rises, the microcompressors were operated at high frequency at the resonance of the piezoelectric diaphragm. This dissertation investigated the feasibility and operation of a multistage gas microcompressor with passive microvalves, allowing the exploration of its miniaturization.

DEDICATION

This dissertation is dedicated to the memory of my father, who risked his life to get everyone here to the United States and made sure that I took advantage of the best opportunities available to me. I will always remember his dedication and sacrifices to get our family to where we are.

TABLE OF CONTENTS

ABSTRACT.....	iii
DEDICATION.....	vi
LIST OF TABLES.....	xi
LIST OF FIGURES	xii
NOMENCLATURE	xix
ACKNOWLEDGEMENT	xxi
CHAPTER 1 INTRODUCTION	1
1.1 Objectives	2
1.2 Thesis Organization	3
CHAPTER 2 MECHANICAL MICROCOMPRESSOR FOR MICRO CRYO COOLING TECHNOLOGY	5
2.1 Mechanical Compression Pump	5
2.2 Literature Review on Micropumps	7
2.2.1 Micropump Fabrication and Assembly.....	11
2.2.2 Multistage Micropump and Gas Microcompressor	12
2.2.3 Micro Actuation Mechanism Literature Review	16
2.2.4 Vacuum Pump: Knudsen Type	18
2.2.5 Microvalves.....	20
2.3 Micro Cooling Technology Summary and Requirement.....	22
2.3.1 Joule-Thomson Principle Operation	23
2.3.2 Microcompressor Integration with JT Cooler.....	24

CHAPTER 3 PIEZOELECTRIC DIAPHRAGM ACTUATOR AND TETHER MICROVALVE DESIGN PARAMETERS	26
3.1 Piezoelectric Unimorph Diaphragm	27
3.1.1 Piezoelectric Unimorph Diaphragm Principle of Operation.....	29
3.1.2 Literature Review of Piezoelectric Diaphragm Design Configuration.....	29
3.1.3 Piezoelectric Material	32
3.1.4 PZT Synthesis and Fabrication of Piezoelectric Review.....	33
3.1.5 Diaphragm Geometric Design Optimization Parameters	34
3.1.6 Diaphragm Test Characterization	35
3.2 Microvalve Model and Design	44
3.2.1 Flow Conditions.....	45
3.2.2 Pressure-Flow Rate Model.....	47
3.2.3 Microvalve Fluid-Structure Characterization	49
3.2.4 Pressure-Flow Microvalve Test Characterization.....	60
3.2.5 Tethered Arm Model.....	66
3.2.6 Transient Couple Fluid Structure FEM Analysis of Microvalve.....	67
3.3 Summary.....	72
CHAPTER 4 SINGLE AND MULTISTAGE MICROCOMPRESSOR MODELING AND SIMULATION	74
4.1 Principle of Operation.....	76
4.1.1 Theoretical Pump Performance.....	77
4.1.2 Compressor Model.....	80
4.1.3 Microvalve Model and Analysis.....	83
4.1.4 Microvalve Simulink Architecture	86
4.1.5 Steady-State Fluid Structure Interaction (FSI) Analysis	88
4.2 Microcompressor Lumped Model Simulations	95

4.2.1	Single-Stage Microcompressor Simulink Architecture	96
4.2.2	Compressor Chamber Model and Simulink Architecture.....	98
4.3	Simulink Simulation Results	99
4.3.1	Single-Stage Dynamic Simulation Results	99
4.3.2	Two-Stage Simulink Model Configuration A.....	102
4.3.3	Two-Stage Dynamic Simulation Results	104
4.3.4	Two-Stage Drive Operational Scenarios	106
4.3.5	Two-Stage Simulink Model Configuration B.....	108
4.4	Simulation Conclusion.....	114
CHAPTER 5 DEVELOPMENT OF THE SINGLE AND MULTISTAGE MICROCOMPRESSOR DEVICE		116
5.1	Introduction.....	116
5.2	Microvalve Fabrication.....	117
5.3	Single-Stage Design.....	118
5.3.1	Single-Stage Fabrication Process.....	118
5.3.2	Single-Stage Microcompressor Design - Final Version	123
5.3.3	Single-Stage Performance with Model Fit.....	126
5.4	Multistage Two-Stage Design	130
CHAPTER 6 MICROCOMPRESSOR TESTING, RESULTS, AND DISCUSSION...		134
6.1	Test Setup	134
6.2	Single-Stage Microcompressor Test Results	136
6.3	Two-Stage Microcompressor Test Results	139
6.4	Microcompressor Efficiency.....	143
6.5	Conclusion	145
CHAPTER 7 SUMMARY, CONCLUSIONS, AND FUTURE WORK		147
7.1	Summary	147

7.2	Conclusion	151
7.2.1	Dissertation Contributions	151
7.3	Future Work and Recommendations	152
7.3.1	Microactuator Improvement	153
7.3.2	Microvalve Improvement.....	153
7.3.3	Improvement in the Characterization of Microvalve Fluid-Structure Interaction	154
7.3.4	Lumped Model Simulation Improvements	155
7.3.5	Device Characterization Test Recommendation.....	156
7.3.6	Redesign for a True Microscale Multistage.....	156
APPENDIX A	CLASSICAL LAMINATE THEORY WITH MATLAB	157
APPENDIX B	MICROCOMPRESSOR SIMULINK MODEL.....	162
B.1	Single-Stage Microcompressor Simulink Model.....	163
APPENDIX C	MICROCOMPRESSOR DESIGN DRAWINGS	171
BIBLIOGRAPHY	177

LIST OF TABLES

Table 2-1: Summary of microcompressors and micro gas pumps.....	13
Table 3-1: Summary of different types of piezoelectric actuators.....	32
Table 3-2: Piezo disc parameters.	37
Table 3-3: Comparison of the results from Figure 3-9 of the center deflection magnitude.....	40
Table 3-4: Comparison of the results from Figure 3-10 of the center deflection magnitude under pressure load.	40
Table 3-5: Summary of piezoelectric diaphragm frequency response analysis.....	41
Table 3-6: Microvalve parameters	45
Table 3-7: Pressure-flow polynomial fitted coefficients.....	55
Table 3-8: Reverse flow coefficients of the experimental test from Figure 3-32	63
Table 3-9: Summary of microvalve pressure-flow model and experimental parameters.65	
Table 3-10: Differential equation parameters of microvalve structure determined from static and transient analysis.....	71
Table 4-1: Theoretical pressure ratio of a single and multistage	80
Table 4-2: Theoretical pressure ratio comparison to the simulated pressure ratio from Simulink.	106
Table 4-3: Pressures ratio validation for two-stage microcompressor between Simulink and analytical results.	114
Table 5-1: Parameter for simulation model.	128

LIST OF FIGURES

Figure 2-1: Micropump made from silicon and microfabrication [2].	7
Figure 2-2: Micro mold injection micropump [7].	8
Figure 2-3: [15] Valveless diffuser micropump schematic.	9
Figure 2-4: [16] Valveless micropump in parallel.....	10
Figure 2-5: Peristaltic micropump [17].	11
Figure 2-6: Stack piezoelectric actuator from PiezoDrive.....	17
Figure 2-7: Stack piezoelectric actuator with flexure structure to amplify displacement.	18
Figure 2-8: [3],[53] 48-stage Knudsen pump schematic and picture.	19
Figure 2-9: Piezoelectric hydraulic amplification for microvalve.....	20
Figure 2-10: Left: JT MCC cold stage developed by Lerou [71]. Right: JT MCC cold stage developed by Ma <i>et al.</i> [77]......	23
Figure 2-11: Schematic of a Joule-Thomson MCC system [71].	24
Figure 2-12: The proposed concept of an electrostatic Stirling cooler by Guo [78].	25
Figure 3-1: Piezoelectric unimorph schematic.	28
Figure 3-2: Polyimide piezoelectric membrane [81].	30
Figure 3-3: Illustration of interdigitated piezoelectric cantilever [85].	31
Figure 3-4: IDT unimorph diaphragm developed by Hong <i>et al.</i> [79].	31
Figure 3-5: Schematic of screen printing PZT [100].	33
Figure 3-6: Piezo disc diaphragm actuator.	36
Figure 3-7: Boundary conditions (BCs) for the piezoelectric diaphragm.	37
Figure 3-8: Unimorph diaphragm deflection test setup.	38

Figure 3-9: Static analysis of piezoelectric unimorph diaphragm deflection profile comparing FEA and CLPT method at zero pressure load.	39
Figure 3-10: Static analysis of piezoelectric unimorph diaphragm deflection profile comparing FEA and CLPT method under pressure load at 60 V	40
Figure 3-11: Frequency response of the diaphragm deflection at resonant frequency driven at 20 V _{pp} with no pressure load.	41
Figure 3-12: Extrapolated dynamic stroke volume.....	42
Figure 3-13: Preliminary measured center deflection of piezoelectric diaphragm under pressure load.	44
Figure 3-14: Microvalve model.	45
Figure 3-15: 2D schematic of microvalve model.	45
Figure 3-16: Schematic of the pressure-flow through the microvalve fixed-plate model with an initial gap height, h_1	49
Figure 3-17: Calculated flow rate from Eq. 3-21 with $\xi = 1$	50
Figure 3-18: Reynolds number for air flow through microvalve.....	51
Figure 3-19: Mach number at different gap height with a fixed valve plate height.	51
Figure 3-20: Plot of the pressure loss due to viscous effect from the fixed microvalve model.....	52
Figure 3-21: Plot of the pressure loss due to inertia effect for the fixed microvalve model.....	53
Figure 3-22: Pressure loss from the microvalve at different gap height and flow rate from FEM analysis. These curves are fitted with second order polynomial to determine the viscous and inertia loss coefficient.	54
Figure 3-23: Flow rate vs. pressure of steady flow through microvalve. Comparison between analytical and FEM result.....	54
Figure 3-24: Viscous loss factors.....	56
Figure 3-25: Inertia loss factors.	56
Figure 3-26: Pressure-flow relation with corrected loss factors for a 30 μm gap height. 57	
Figure 3-27: (a) Schematic of the microvalve plate in the close position. (b) Schematic of the steady gas flow of the microvalve deflecting the microvalve to an equilibrium gap height.....	58

Figure 3-28: Valve plate gap height for flexible valve model, Q_2	59
Figure 3-29: Pressure-Flow characteristic curve for flexible valve model, Q_2	59
Figure 3-30: Microvalve test jig.	60
Figure 3-31: (a) Microvalve pressure-flow test set up for forward flow. (b) Microvalve pressure-flow test set up for reverse leakage flow.....	61
Figure 3-32: Microvalve pressure-flow test for forward and reverse flow.....	62
Figure 3-33: Comparison of experimental pressure-flow curve to model for a 0.5 mm inlet hole.....	64
Figure 3-34: Comparison of experimental pressure-flow curve to model for a 0.5 mm inlet hole.....	64
Figure 3-35: Schematic of valve spring model.....	67
Figure 3-36: FSI FEM boundary conditions setup.	68
Figure 3-37: (Top left) quadrilateral mesh for the microvalve. (Top right) Deflection of the microvalve with fluid force. (Bottom left) tetrahedral mesh for fluid with the top boundary hidden. (Bottom right) tetrahedral mesh for fluid with the bottom boundary hidden.....	69
Figure 3-38: Microvalve plate structural displacement response to transient FSI simulation.....	70
Figure 3-39: Pressure distribution of microvalve at steady state.....	72
Figure 4-1: Flow chart for the design of microcompressor architecture and simulation results.	75
Figure 4-2: (a) single-stage microcompressor schematic. (b) multistage, two-stage, microcompressor schematic.....	77
Figure 4-3: Theoretical pressure ratio for a given number of stages given by the volume ratio.	80
Figure 4-4: Compressor chamber control volume	81
Figure 4-5: Schematic of the microvalve structure.....	82
Figure 4-6: Flow chart of the microvalve Simulink simulation design.	84
Figure 4-7: FEA result of the microvalve spring force constant.	85
Figure 4-8: Microvalve force versus displacement.....	86

Figure 4-9: Microvalve architecture of fluid-structure dynamics with step pressure input.	87
Figure 4-10: Step response of the microvalve Simulink simulation. (a) step input of the pressure at 7 kPa. (b) velocity response of the valve plate. (c) the response of the valve plate mass flow rate. (d) the response of the valve plate height.....	88
Figure 4-11: Fluid-structure interaction of microvalve with steady steady pressure-displacement, showing the cross section of the velocity magnitude and displacement of the microvalve with 7 kPa at the inlet.	89
Figure 4-12: FSI result of the valve plate displacement at various constant inlet pressures.....	90
Figure 4-13: Comparison of the adjusted microvalve plate Simulink simulation result to the FEA FSI transient analysis result.....	91
Figure 4-14: FSI result of the mass flow rate through the microvalve at various inlet pressure.	91
Figure 4-15: Microvalve lumped model dynamic simulation.	93
Figure 4-16: Frequency response of the valve plate height.	94
Figure 4-17: Simulation result of mass flow rate through the passive microvalve as a function of chamber pressure frequency.....	95
Figure 4-18: Flow chart of the variables and its relationship to each block in Simulink.	97
Figure 4-19: Simulink model of a single-stage microcompressor which include the pump chamber, volume chamber control, inlet and outlet microvalves block.	98
Figure 4-20: The Simulink architecture for a compressor chamber representing Eq. 4-9 and Eq. 4-10.	99
Figure 4-21: Dynamics of single-stage microcompressor. The chamber pressure is monitored along with the valve height and mass flow rate for the inlet and outlet valve, respectively.....	100
Figure 4-22: Performance curve for single stage microcompressor at different operation frequency.	101
Figure 4-23: Summary of the single-stage microcompressor performance.....	102
Figure 4-24: Schematic of a two-stage multistage microcompressor for configuration A and configuration B.	103
Figure 4-25: Simulink dynamic model of a two-stage multistage microcompressor.	103

Figure 4-26: Dynamic simulation for a two-stage microcompressor. (a) volume for the 1 st stage (in black) and volume for the 2 nd stage (violet). (b) shows the current pressure in each chamber. (c) the mass flow rate through the interconnect microvalve and outlet microvalve. (d) shows the total flow rate out from stage 1 and 2.....	105
Figure 4-27: Performance curve for a two-stage microcompressor in series operating in phase. Stage 1 and 2 are operating at the same frequency.....	106
Figure 4-28: Simulated results of maximum pressure ratio generated. (a) Stage 1 operates at a higher frequency than stage 2. (b) Stage 2 operates at a higher frequency than stage 2.	108
Figure 4-29: Multistage two-stage schematic of configuration B with an interconnecting chamber.....	109
Figure 4-30: Simulink Architecture for a two-stage microcompressor configuration B.....	110
Figure 4-31: Internal architecture of the 1 st stage Simulink block of the multistage microcompressor Simulink architecture.	111
Figure 4-32: Interconnect chamber architecture.....	111
Figure 4-33: The internal architecture of the 2 nd stage Simulink block of the multistage microcompressor Simulink architecture.....	112
Figure 4-34: Performance curve simulation result for two-stage microcompressor with various interconnected volume (configuration B).	113
Figure 5-1: Microvalve fabrication steps.....	117
Figure 5-2: Image of microvalve structure on silicon substrate.	118
Figure 5-3: 3D printed model of single stage microcompressor.	120
Figure 5-4: 3D printed microcompressor performance curve.	122
Figure 5-5: CNC single-stage microcompressor.	124
Figure 5-6: Dead volume of single-stage microcompressor.....	128
Figure 5-7: Modeled performance curve compared to the experimental curve of single-stage with various back pressure leak rate.	130
Figure 5-8: Cross-section and exploded view of the two-stage microcompressor design.	131

Figure 5-9: Injection of epoxy into the cavity for bonding and sealing. Assembly is screwed together and clamped at the center to ensure no epoxy flow into the valve surface.	132
Figure 5-10: Photograph of the two-stage micro gas compressor.	133
Figure 6-1: Performance curve and deflection test set-up.	135
Figure 6-2: The pressure-flow performance curve of the single and two-stage microcompressors.	137
Figure 6-3: The pressure rise of the compressor at its maximum resonant frequency with different voltage applied to the maximum operating voltage of the piezoelectric diaphragm of 60 V _{pp}	138
Figure 6-4: Maximum pressure rise occurs at resonant frequency of the piezo diaphragm actuator.	139
Figure 6-5: Stage 1 of the two-stage microcompressor device frequency.	141
Figure 6-6: Stage 2 of the two-stage microcompressor device frequency response.	141
Figure 6-7: Frequency sweep of the two-stage microcompressor.	143
Figure 6-8: Measured pressure-flow performances and compressor efficiencies of the single-stage and two-stage microcompressors.	145
Figure 7-1: Microvalve future recommendation.	154
Figure A-1: Deflection profile of the piezoelectric diaphragm actuator from the Matlab source code using the CLPT method.	161
Figure B-1: Single-stage top level Simulink model.	164
Figure B-2: Single-stage inlet microvalve sub-level model.	165
Figure B-3: Single-stage outlet microvalve Simulink sub-level model.	166
Figure B-4: Single-stage outlet microvalve Simulink sub-level model.	167
Figure B-5: Two-stage microcompressor Simulink top level model.	168
Figure B-6: 1 st Stage Simulink model sub-level model of the two-stage model.	169
Figure B-7: 2 nd Stage Simulink model sub-level model of the two-stage model.	170
Figure C-1: Housing body of single-stage microcompressor, Part IV	172

Figure C-2: Dimensions of single-stage microcompressor for part I, part VI, piezo disc and O-ring.....	173
Figure C-3: Bottom housing of 2-stage microcompressor, body 3.	174
Figure C-4: Top housing of 2-stage microcompressor, body 1.....	175
Figure C-5: Middle housing of 2-stage microcompressor, body 2.....	176

NOMENCLATURE

A_{in}	Cross sectional area of air flow for inlet microvalve
A_o	Cross sectional area of air flow for outlet microvalve
A_v	Surface area of microvalve for pressure load
c	Damping coefficient of microvalve dynamic
C_f	Coefficient of flow friction
D_{in}	Microvalve inlet cross section area diameter
D_o	Microvalve outlet cross section area diameter
f_1	Drive Frequency of the volume stroke in stage 1
f_2	Drive Frequency of the volume stroke in stage 2
m_c	Mass in chamber
k_v	Spring constant of tethered microvalve
\dot{m}_{in}	Mass flow rate in
\dot{m}_o	Mass flow rate out
m_v	Mass of valve
n	Polytropic constant of air, 1.41
P_{in}	Inlet pressure to chamber
P_c	Chamber pressure
P_{co}	Initial chamber pressure

\dot{Q}_o	Flow Rate out of stage
V_c	Current volume chamber
V_d	Dead volume of chamber
V_{max}	Maximum volume of chamber
V_{min}	Minimum volume of chamber
V_s	Stroke volume
w	Volume stroke actuation frequency
z	Microvalve height
\dot{z}	Microvalve velocity
\ddot{z}	Microvalve acceleration
ρ_c	Density of gas in chamber
ρ_{in}	Density of gas at inlet

ACKNOWLEDGEMENT

This author acknowledges the financial support from the LaSPACE Grant Graduate Research Assistance (GSRA).

I would like to thank my advisor, Dr. Hegab, who has given me the opportunity to join his research team. He is always open to new ideas and always supported and allowed me to try different ideas. I would like to thank him for finding time out of his busy schedule to sit with me and provide advising for my research work.

I would like to thank all the staff members at the Louisiana Tech Institute for Manufacturing facility (IFM). Davis Bailey has been an invaluable help to me in getting the training and for the cleanroom equipment. He is always willing to help and give technical advice on the micro fabrication processes in the clean room. Ji Fang was also great with providing training and advices on the cleanroom equipment. I would like to thank Debrah Wood for her support as well. I would like to thank my group member, Naveen Gangaraju, for getting me started in our lab.

I owe a great deal to my family, fiancé, and friends for supporting me and being there for me throughout these years. I would not have made it without their daily encouragement, support, and love. Special thanks to:

My mother who always makes sure I get my favorite Vietnamese dish when I come home.

My sister Trisha for always making sure I have everything I need.

My friends: Sayeed, Vu, Khang, Quang, and Henry for always being there for me, even when times were tough.

My fiancé, Christina Huynh, to whom I am grateful to have in the past 11 years for the time that we shared together and the struggles in the last 4 years of being apart while we were focusing on our careers.

CHAPTER 1

INTRODUCTION

Since the emergence of Micro Electromechanical System (MEMS), researchers have adapted this technology towards the development of micropumps due to their potential use in many life sciences, biological, and microfluidic applications. Miniaturization of micropumps allow for more precise control of fluids that are needed in some applications; it also allows for portability, low power consumptions, and small footprint integration. As micropump technology matures with liquids, researchers are using this technology to develop micro gas pumps and micro gas compression applications.

Electronics such as infrared sensors, low-noise amplifiers, and superconducting devices require cryogenic temperatures to improve their performance. Signal-to-noise ratios and bandwidth improve as thermal noise decreases under cryogenic temperature conditions. Electronics that operate in space such as microsatellite systems would benefit from active cooling due to the lack of air molecules in vacuum space. Micro cryogenic cooling can provide the solution to these applications by miniaturizing a vapor compression system such as a Joule-Thomson (JT) cooling system, which is currently investigated for miniaturization. JT MCC successful development is still hindered by a lack of a successful micro gas compressor (microcompressor) closed cycle operation.

Microcompressors are needed to pressurize the gas to flow through an orifice valve for the expansion process in the vapor compression system. One of the challenges for microcompressors has been the large pressure and pressure ratio requirement for such systems. Work has been done on improving the technology of the JT MCC system. To meet the high gas pressure demand for thermal cooling, a cascaded multistage microcompressor connected in series is investigated to enhance the performance of the microcompressor. Passive microvalves are used as check valves to control the flow between each stage.

1.1 Objectives

The objective of this dissertation is to investigate the feasibility and develop a multistage microcompressor design using a piezoelectric diaphragm and passive microvalve cascaded in series to produce large pressure and pressure ratio for micro cooling applications. To accomplish this objective, modeling, prototyping and experimental tests are conducted in this dissertation.

The modeling and simulation of the multistage microcompressor used a lumped model approach and is simulated with Matlab Simulink tool. To first develop this model, an understanding of the characteristics of the microvalve and piezoelectric unimorph actuator in the microcompressor are necessary. Interaction of the microvalve structure with the gas flow is first modeled with a static and quasi-steady flow approach. Steady-state and transient analysis of the valve plate response to the flow through the valve is analyzed with finite element method to determine the fluid-structure parameters for the lumped model. The piezoelectric unimorph diaphragm is characterized with FEM,

analytical method and experimentally to extract the proper volume stroke in response to various input parameters.

The compressor is modeled as a lumped model. With the test data of the valve sealed reverse leak, the reverse leak model is incorporated into the lumped model to provide a better fit to validate the microcompressor's performance. A single-stage and multistage microcompressor is designed, fabricated, assembled, and tested to be compared with the model. The assembled multistage and microcompressor is used to validate the feasibility of the utilizing multistage design with passive microvalves.

1.2 Thesis Organization

Chapter 2 discusses the different variation and operating principles of previously developed micropumps and their characteristics. Micropumps are typically designed for incompressible fluids such as water. It is worth discussing these because they share similar operation principles, fabrications, and assembly methods. A review of the previous microcompressors, multistage microcompressors, microactuators, and microvalves are also discussed. The Joule-Thomson cooling is also discussed to understand the requirements needed from a microcompressor.

Chapter 3 is divided into two sections to study the components in the microcompressor. The first half of the chapter deals with the study and characterization of the piezoelectric unimorph diaphragm. The second half deals with the study of the microvalve fluid-flow interaction model and transient analysis. Testing and finite element analysis is also presented to aid with the characterization processes.

Chapter 4 presents the lumped model and simulation of the microvalve, the single-stage and the two-stage microcompressors. The simulation studies include the

dynamic of these systems and the performance curve of the microcompressors. The two-stage simulation also includes a model of the dead volume of the interconnect chamber which exists between the two chambers. In phase and out of phase actuation between stage one and stage two of the two-stage device were carried via simulation.

Chapter 5 presents the fabrication and assembly processes of the single-stage and two-stage microcompressor devices.

Chapter 6 presents the test results of the two fabricated devices including its characterization results.

Chapter 7 summarizes the findings and discusses future works and improvements of the microcompressor to satisfy the microcooling requirements.

CHAPTER 2

MECHANICAL MICROCOMPRESSOR FOR MICRO CRYO COOLING TECHNOLOGY

2.1 Mechanical Compression Pump

Since the introduction of Micro Electro Mechanical Systems (MEMS), efforts have been made to develop micropump for precise control of the fluid in the micro and nano liter range. The silicon bulk microfabrication techniques have made it possible to realize many different variations of micropumps for various applications. One of the earliest device reported by Lintel [1] in 1988 was made of piezoelectric disc and silicon check valves. Micropumps are typically configured as a mechanical compression pump that utilizes a mechanical actuator to displace the fluid in the chamber, transferring the fluid from an inlet port to the outlet port. Early micropumps were designed for incompressible fluid such as water, making it more suitable for many applications in the biological, pharmaceutical, and chemical applications. As micropump technology mature in the last two decades, researchers are currently exploring the gas domain applications, expanding into other areas such as gas chromatography and microelectronic cooling, which would require a micro gas compressor.

Micro gas compression pumps (microcompressors) operate within the same principle as a micropump. They still require a pump chamber to compress the gas and check valves for the inlet and outlet ports to prevent a reverse gas flow. Although

micropumps can pump liquids due to the incompressibility property of liquids, it can become incapable of pumping a liquid when a gas bubble is introduced and trapped in the chamber. Bubble toleration can be possible with increases in the compression ratio of the pump chamber. Linnemann [2] reported a micropump that is bubble tolerant by maximizing the stroke volume and minimizing the dead volume. Gas compression pumps are more of a challenge than liquid micropumps due to the compressibility of gas. Additionally, micro actuators produce little volume displacement and generate low force, displacing lesser volume at high back pressure. The low stroke volume from the actuator makes the microcompressor more sensitive to the dead volume that is a challenge to eliminate completely. Furthermore, reverse leakage from the microvalve can attenuate the pressure rise in the compressor. To develop a microcompressor, a review of micropumps is needed to understand its limitations and applications.

In the last decades, there have been extensive research in utilizing different strategies in developing micropumps. Many micropumps except for the Knudsen pump [3] rely on a moving membrane to pump fluids mechanically or compress gas in the chamber. With the exception of using diffuser valves [4], mechanical micro check valves are typically used for the inlet and outlet port of the pump chamber. Micropumps have many different designs and actuation mechanisms. Most of these technologies are transferrable and compatible for designing a multistage microcompressor. In this chapter, a review and identifications of the various micropump technologies are that are useful in developing a multistage micro gas compressor are presented. The first review includes some of the general forms of micropumps that were initially designed for liquid handling, different variations of the micropumps, the advantages and limitations of these various

types of micropumps, and the microvalves and microactuation methods. The second review presents various micro gas pumps and compressors that have been developed, and the multistage configurations that have been developed.

2.2 Literature Review on Micropumps

Previous work on micropumps with piezoelectric membrane and passive microvalves can be seen in [2], [5]–[13]. In one example, Linneman *et al.* [2] developed a micropump made from silicon using piezoelectric diaphragm actuator as shown in **Figure 2-1**. Linneman was able to maximize the dead volume making the pump tolerant to gas bubbles trapped in the chamber. Kamper [7] developed a piezoelectric micropump from injection molding as shown in **Figure 2-2**. The micropump delivered a maximum flow rate of 400 $\mu\text{l}/\text{min}$ and maximum pressure rise of 2.1 kPa for water, and a maximum flow rate of 3.5 ml/min and 0.5 kPa for air.

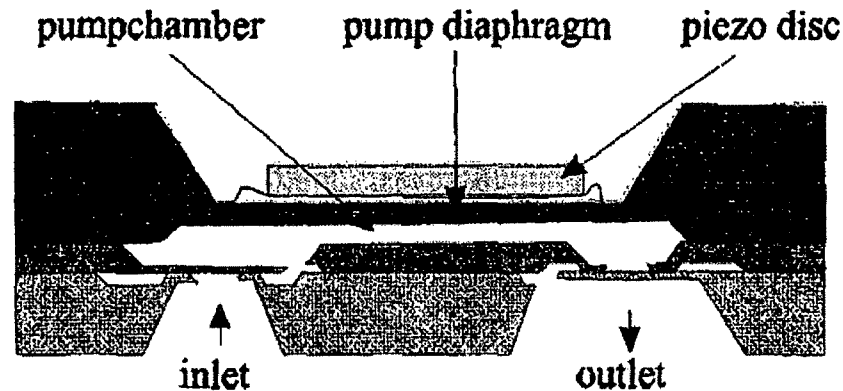


Figure 2-1: Micropump made from silicon and microfabrication [2].

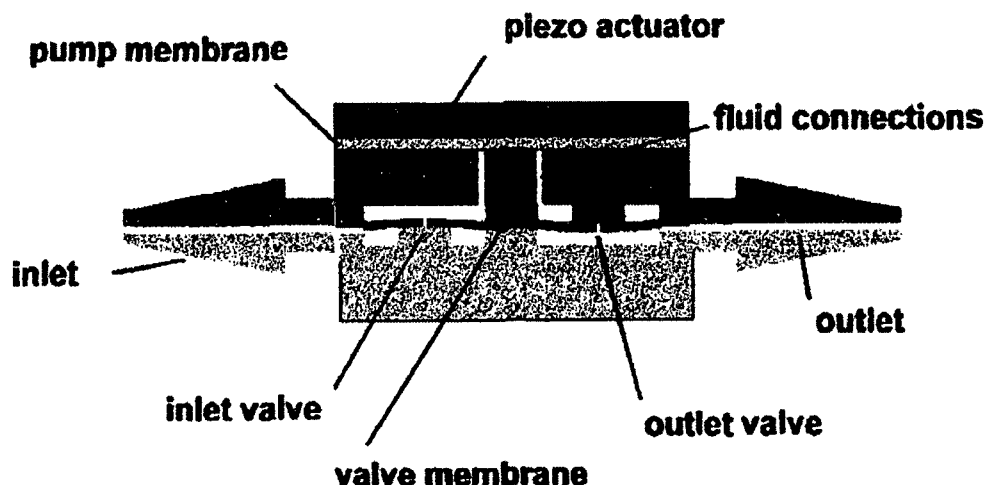


Figure 2-2: Micro mold injection micropump [7].

One of the undesirable effect of a micropump is the sensitivity of trapped gas bubble in the pump chamber. This situation may limit the reliability of the pump and its performance. These pumps developed by Linneman and Kamper, have self-priming capability and are bubble-tolerant due to the high compression ratio. The compression ratio is the ratio of the stroke volume to the dead volume of the pump chamber. Compression ratio of more than 1.13 [2] was suggested by Linneman.

Stemme [4] developed a valveless micropump with no moving parts for the inlet and outlet microvalves. This type of microvalve used converging and diverging shape ducts which can behave like a diffuser or a nozzle, depending on the mode of the pump as shown in **Figure 2-3**. During the supply mode, the inlet behaves as a diffuser when it has less flow restriction going into the chamber than the outlet nozzle, thus allowing net flow into the chamber. In the pump mode, the outlet valve has less flow restriction for fluid to flow out of the chamber than the inlet, thus resulting in net flow out of the outlet duct. Gerlach [14] reported successful gas pumping using a

diffuser type pump similarly shown in **Figure 2-3**. Maximum pressure rise of 2.8 kPa and maximum flow rate 7.5 ml/min at zero load were achieved at a resonance operating frequency of 12.1 kHz.

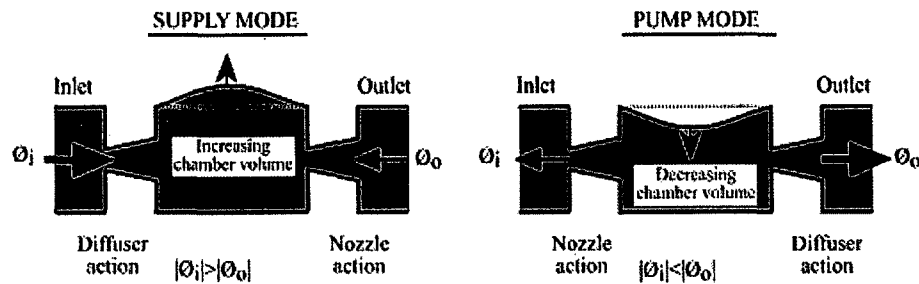


Figure 2-3: [15] Valveless diffuser micropump schematic.

These pump designs produced pressure fluctuation and oscillating flow. In **Figure 2-4** Olsson [16] suggested using a two-pump chamber operating in parallel with the antiphase operation to reduce these effects and to enhance the performance of the micropump. The performance of the valveless micropumps in **Figure 2-4** can be less than the conventional micropump with valves. However, the valveless micropump can be more robust and reliable compared to the micropump with microvalves. Furthermore, it may be more suitable for biological applications where micro particles may be present in the fluid and that would interfere with mechanical microvalves.

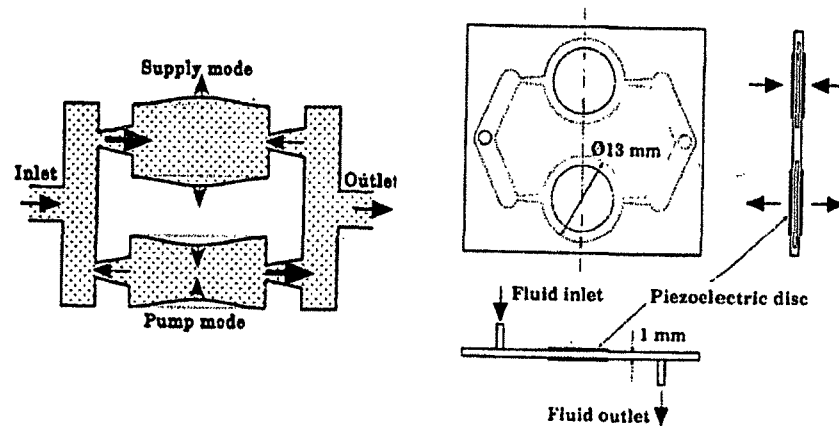


Figure 2-4: [16] Valveless micropump in parallel.

Peristaltic micropumps similar to the one shown in **Figure 2-5** can be classified as a multistage micropump. These types are comprised of three chambers that operate in peristaltic sequence to drive the fluid, eliminating the need for a check valve. Each chamber is actuated by its own actuator, and depending on its sequence, it acts either as a valve or pump. Jang and Yu [17] developed a piezoelectric peristaltic pump made from Pyrex glass and silicon that can pump air at a flow rate of 17.58 $\mu\text{l}/\text{min}$ with no back pressure reported. With a similar design, Hsu [18] generated 217 l/min and 9.2 kPa with water. This type of pump requires a microcontroller to control the action sequence of each pump to drive the fluid peristaltically.

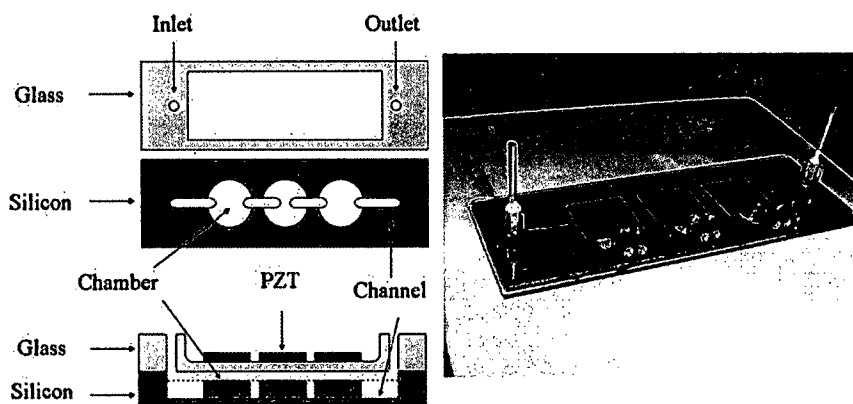


Figure 2-5: Peristaltic micropump [17].

2.2.1 Micropump Fabrication and Assembly

Micropumps are typically fabricated using MEMS fabrication made from silicon and glass substrate. This involves bulk micromachining of the substrate and bonding multiple wafer substrates together [19] through methods such as anodic bonding, adhesive bonding with an intermediate layer, eutectic bonding, and fusion bonding [20]. Yoon bonded silicon substrate-based micropump with Au as the intermediate layer [21]. This method is also useful with heterogeneous materials, such as copper [22] and gold [23]. Adhesive bonding may involve an intermediate layer such as evaporated glass, resist, or polyimides providing lower temperature bonds that are not suitable for certain MEMS application.

In micropump, certain components can be sensitive to the high temperature bond method. Piezoelectric materials lose their piezoelectric properties beyond the Curie temperature starting above 200°C. Bonding methods that require high temperature with the piezoelectric layer already attached to the substrate would limit the selection of bonding methods. Bulk micromachining of the substrate to make the valve features, channel, and chamber feature often requires wet etching or the DRIE etch method. This

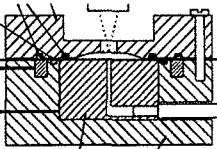
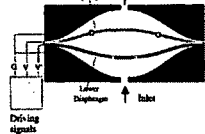


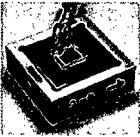

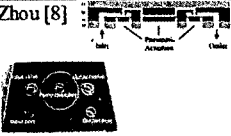

involves the photolithography process. Utilizing microfabrication methods can be complex and involve many processes. Additionally, this method can still be very expensive due to equipment and labor intensive processing.

There are other means of fabrication and assembly of microcompressor using the mass manufacturing method such as injection molding. Kamper has produced a piezoelectric injection mold micropump [7] and Cabuz produced a dual diaphragm pump using electrostatic actuation with injection mold [24]. New techniques and methods of micro injection molding can provide plastic and metal parts with features down to 100 μm size [25]–[27]. With the capability of micro machining such as micro-electrical-discharge-machining (μEDM), focused ion-beam milling (FIB), high resolution mold inserts can be fabricated and integrated into the mold for high resolution molded parts [28], [29].

2.2.2 Multistage Micropump and Gas Microcompressor

This section provides a review of the different microcompressors including some with multistage configurations. A summary of the microcompressors in this section is provided in **Table 2-1**. Review in literature showed the type of actuation micro gas pumps and microcompressors that have shown success are the electrostatic diaphragm, piezoelectric diaphragm, stack piezoelectric pump, and the Knudsen pump type. The overview and operation of principle for these types of pumps is discussed in the later section of this chapter. Thus far, the search in the literature has shown micro gas pump development has been focused on vacuum pumping for micro gas analyzer [30] such as micro gas chromatography (μGC) [31], whereas micro gas compressor is focused on micro cooling applications.

Table 2-1: Summary of microcompressors and micro gas pumps.

Gas Micro compressor							
Author	Configuration	Fluid	Pressure	Flow Rate	Pressure Ratio	Voltage/Power	Size
Sathe [35] 	Electrostatic	R123	23 kPa			420 V	
Cabuz [24] 	Electrostatic	R123	2 kPa	28 sccm			1.5 x 1.5 x 0.1 cm
Kim [36] 	Electrostatic, multistage, active microvalves	air	17.7 kPa, 18 stage	4 sccm		57 mW	25.1 x 19.1 x 1 mm ³
Besharati [45] 	Electrostatic, multistage, active microvalves	air	4.4 kPa	0.36 sccm		<100V 10 mW	4 mm ²
Yoon [21] 	Piezoelectric diaphragm, passive microvalve	R123	17 kPa			1.17, 1.31	
Vanapalli [38] 	Stack flexure piezoelectric	nitrogen gas	2.5 MPa		1.11	100 V 2.73 W	
Zhou [8] 	External pneumatic pressure	gas unknown	21.8 kPa (Vacuum Pressure)				
Lewis [39] 	Stack piezoelectric, passive microvalves	air	0.4 MPa	20 sccm	4:1	42 V _{pp} 1 W	~4 cm ³

In 1999 and 2001, Shannon [32] and Cabuz *et al.* [24] developed a dual diaphragm gas micropump utilizing electrostatic actuation consisting of metallized Kapton diaphragms for the actuation and valve's mechanisms. Their design achieved 2 kPa of pressure and a flow rate of 28 ml/min. To achieve larger pressure rises, Cabuz suggested an array of stages (multistage) to increase the pressure head of the pump. Sathe [33]–[35] designed a similar electrostatic gas pump focusing on the application of micro vapor compression cooling. The pump reached 23 kPa at actuation voltage of 420 V. According to Sathe, the pump can theoretically compress the gas to 315 kPa, but limitations on the elastic strain of the diaphragm can prevent operating against a high back pressure.

Kim *et al.* [36] developed multiple multistage electrostatic gas pumps each consisting 2-, 4-, and 18-stages. When operating at 15 kHz, the multistage utilized fluidic resonance that occurs in the chamber to achieve a high flow rate and pressure rise of 2.5, 7, and 17.7 kPa, respectively. The maximum flow rate achieved respective to the number of stages are 2.1, 3, and 4 ml/min. This micro gas pump is smaller in scale compared to previous electrostatic pump mentioned by Cabuz, Sathe and Shannon. It employs separate chambers for electrostatic active valves to control the gas transfer between each stage. The active valves in the device are critical to the gas pumping operation by serving as control valves. In a closed position, the active valves wait for the pressure to build up in the diaphragm chamber and open up at an optimized time to allow gas flow into the next stage. Active valves increase the complexity of the overall device but can be valuable in minimizing the valve leakage.

Yoon *et al.* [37] developed a micro gas compressor and arranged the two compressors in series with a connecting tube and showed that the pressure ratio can be improved. Passive cantilever valves were used between the pump chambers. The maximum pressure ratio achieved at zero flow rate was 1.17 for a single stage and 1.31 for a two-stage with refrigerant 134a as the test gas. Yoon *et al.* demonstrated that the pressure ratio can be increased with micro gas compressors in series.

In 2008, Vanapalli *et al.* [38] developed a micro gas microcompressor to power a micropulse tube cryocooler. The device was capable of delivering pressure of 2.5 MPa and pressure ratio of 1.11. The large pressure generated was contributed from the stacked piezoelectric actuator amplifying the displacement with a flexure structure integrated to the piezoelectric. It provided large a stroke volume in combination with high force generation. These types of compressors require a stack piezoelectric integrated to a flexure structure, which can make the overall compressor a little bit larger in size, being approximately $\varnothing 50$ mm X 45 mm. Lewis *et al.* [39] from the University of Colorado Boulder developed an improved micro gas compressor with a similar configuration. No flexure structure was incorporated to the stacked piezoelectric actuator. The maximum back pressure the pump can deliver is 0.4 MPa with a pressure ratio of 4:1. This device was one of the first successful micro gas compressor integrated into a JT microcooler.

Yoon and Lewis developed a multistage microcompressor using passive microvalves to increase the pressure rise in each stage [21], [39]. An integrated cascaded multistage micro gas compressor has not yet been developed. Not much is known how the interaction of the microvalves between the pump chambers and the phase of the pump would affect the performance of the microcompressor.

Zhou [8] developed a silicon micro vacuum pump capable of pumping down to 164 torr of absolute pressure, equivalent to a pressure difference of 79 kPa. It was one of the first to achieve such high pressure for gas pumping, although external pneumatic pressure was used to actuate the diaphragm and to actively control the microvalves. Similar to previous pumps, dead volume reduction in the pump chamber was the key to having a successful pump.

2.2.3 Micro Actuation Mechanism Literature Review

One of the limitations for a high performance microcompressor is the availability for an actuator to have all the needed characteristics: high actuation force, large volume displacement, small in size, fast response time, low thermal losses, and minimal power consumption. When designing a micro gas pump or microcompressor, the actuation mechanism is crucial to the design. It can dictate the size of the compressor, its configuration, operation, and the overall performance of the compressor. Here a discussion of the operation principle for different types of actuation mechanisms that have been developed for a microcompressor are presented. Numerous variation of actuation mechanisms have been seen in the literature. The one that are viable for gas compression will be focused on in the discussions.

2.2.3.1 Electrostatic Actuation

Electrostatic actuation is widely used in MEMS. Zengerle [40] was one of the first to adopt electrostatic actuation to a micropump. The micropump utilized electrostatic attraction between two oppositely charged electrode plates to generate displacement from the plate. The electrode is typically configured with a rigid body and a deformable

diaphragm. When a voltage V is applied, the electrostatic force pulls the deformable towards the other rigid electrode. The electrostatic force is given as

$$F = \frac{\epsilon AV^2}{2h^2} \quad \text{Eq. 2-1}$$

where ϵ is the permittivity of free space, A is the surface area, h is the gap between the two plates. When the actuation voltage is removed, the deformable membrane is released. This creates a reciprocating pump cycle. The performance with electrostatic micropump and gas micropump have improved with recent advances made by [36], [41]–[46].

2.2.3.2 Stack Piezoelectric

Several researchers have integrated stack piezoelectric into their micropumps for diaphragm actuation [47], [48]. This type of actuation requires piezoelectric stacked together forming a longer length to achieve a larger force and displacement as shown in **Figure 2-6**. Despite the increase in displacement, a 10 mm length actuator from PiezoDrive could only produce a stroke of 14 μm with 330 N of force.

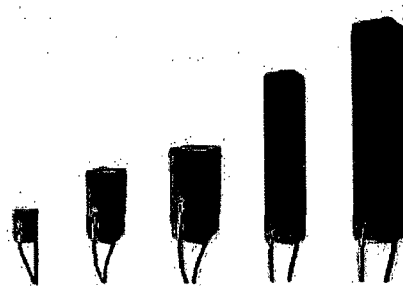


Figure 2-6: Stack piezoelectric actuator from PiezoDrive.

To increase the displacement of these actuators, flexure structure are connected to the actuator as shown in **Figure 2-7** to amplify the displacement, making it more suitable for micro gas compression. However, this can make the overall size of the compressor larger.

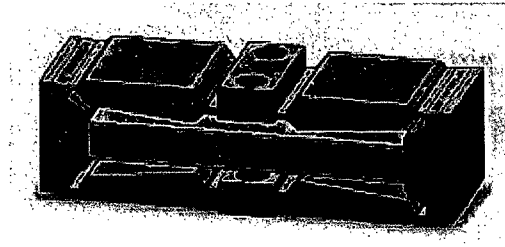


Figure 2-7: Stack piezoelectric actuator with flexure structure to amplify displacement.

2.2.4 Vacuum Pump: Knudsen Type

Micropump is also developed for the vacuum needed application for portable chemical and biological analytical instruments. The Knudsen pump [3], [49]–[52] is a thermal molecular pump that relies on the temperature difference in two chambers, one cold chamber and a hot chamber to produce a forward flow of gas from the hot to the cold chamber. The temperature difference between the two chambers generates a pressure differential from the difference in the rate of the molecular flux [51]. This type of pump consists of a wide channel and a narrow channel for each alternating stages as shown in **Figure 2-8**. The wide narrow channel is used to generate the temperature difference between each stage to transport the gas in the viscous regime from the hot to the cold chamber, and the narrow channel needs a hydraulic diameter less than the mean free path of the gas.

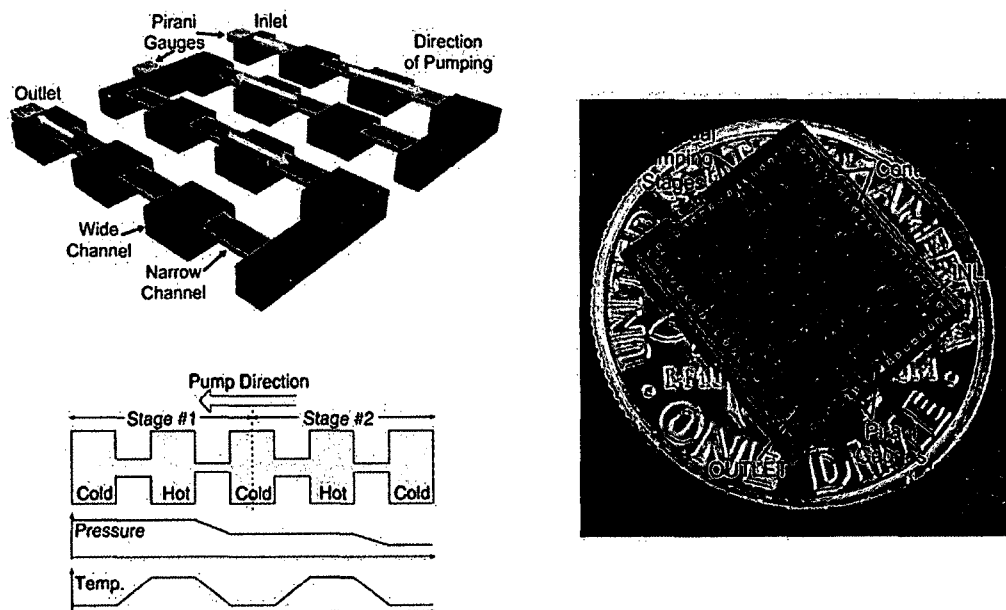


Figure 2-8: [3],[53] 48-stage Knudsen pump schematic and picture.

While these pumps have been designed to generate vacuum pressure down to only 50 Torr, it may be worthwhile to review its design because of its attractive characteristics. The pump requires no moving parts and can be kept at a microscale level. Developed by the University of Michigan [3], [50], the multistage cascaded stages devices were 48- and 168-stage, capable of generating a vacuum pressure of < 50 Torr.

2.2.4.1 Hydraulic Amplification

Hydraulic amplification [54], [55] is a method used to overcome small displacement in micro actuators with a large force. Steyn *et al.* [56] and Robert *et al.* [6] utilized stacked piezoelectric with silicone oil to amplify the stroke of a microvalve from $0.65 \mu\text{m}$ to $26 \mu\text{m}$, resulting in 40x amplification as shown in **Figure 2-9**. It was designed and intended for active valves. However, it is feasible to utilize this method for gas compression. This device can be complicated to fabricate at the microscale level, but is a viable option that meets most of the criteria in a micro actuator.

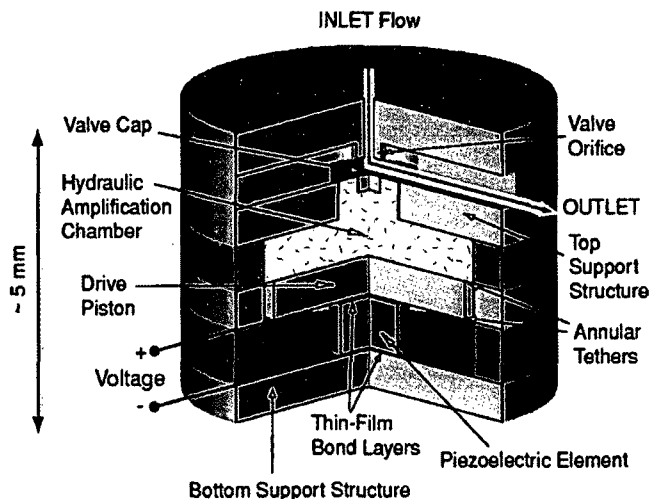


Figure 2-9: Piezoelectric hydraulic amplification for microvalve.

2.2.5 Microvalves

Microvalves are used as check valves to allow the flow of gas or fluid flow in a forward direction and restrict the flow in the reverse direction. It controls the gas flow between the ambient conditions and the pump chamber, and it is crucial for the function of a microcompressor. It is also needed for use in multistage chambers, where the microvalves are used to control the flow and pressure between each stage. With positive bias pressure, the microvalve opens for forward gas flow and closes when there is negative bias pressure to prevent reverse flow. Microvalves can be categorized as passive or active valves. Each has its own inherent advantages and disadvantages.

Passive microvalves are dependent on the pressure difference generated by the pump chamber to control the open and close position. If not designed properly, the microvalves cannot open due to its high cracking pressure which stems from high stiffness and stiction between the microvalve surface and the seat. Reverse leakage can cause the pump chamber to lose some of the generated pressure. Reverse leakage occurs

when the microvalve is still open due to the lag in the dynamic of the structure in response to the fast rate of change of chamber pressure, allowing gas to flow in the reverse direction.

Microvalve designed for gas application requires better valve sealing between the valve's surface and its seats. Smooth surface and larger sealing surface is needed due to the large mean free path of the gas passing through the sealing surface. A larger surface area can provide better gas sealing, but it would generate more stiction force. This can become a trade-off between the sealing and the stiction force [57].

2.2.5.1 Passive Microvalve and its Literature

Passive microvalves designed in the microscale are configured as a cantilever, tether, and ball valves [58]. Materials ranging from silicon/nickel [59], [60], aluminum [61] parylene, PDMS [62], SU8 [63], to polyimide [12] have been used to fabricate microvalves. Feng [5] made a comparison between a cantilever and tethered type valves made from parylene microvalves and noted the [60] effect of how the two types of structures would have on the flow rate of the micropump. The cantilever had a lower resonant frequency than the tether microvalves. At a certain frequency range, the inlet and outlet microvalve can come out of phase with the pump chamber actuation frequency and decrease the flow rate of the fluid. Microvalves developed by Li *et al.* [59] is robust enough to withstand pressure of up to 350 psi and up to 10 kHz of pumping frequency.

2.2.5.2 Active Microvalve and its Literature

Active microvalves can diminish reverse leakage and require extra control through other means of actuation for the open and close operation. The holding forces of the microvalve can be limited to the forces generated by the actuator. Electrostatic

microvalves have been demonstrated by Yang [57] and Kim [36]. Micro-hydraulic is one of the means for actuation for active valves to amplify the displacement of the microvalve and provide high force and high deflection [64]. Piezoelectric diaphragm [65] and stacked piezoelectric actuator [59], [66] have also been used for active valves.

2.3 Micro Cooling Technology Summary and Requirement

Several groups have been working on developing micro cryogenic cooler (MCC) since the inception of micro technology. Jeong [67] identified one of the key challenges in the development of an MCC is the miniaturization of a mechanical compressor. Other groups from [68]–[74] have previously developed the cold stages for a JT MCC. Examples of the JT MCC shown in **Figure 2-10** have no moving parts (except for the microcompressor), making it easy for miniaturization [75]. Previous pressure requirement for the JT MCC was in the range of 20 MPa. In a recent effort by Lewis *et al.* [76], there has been success in lowering the pressure requirement for a JT cooling system. Lewis *et al.* demonstrated a JT MCC using a new different mixture of hydrocarbons to lower the high pressure requirement to 0.4 MPa, cooling down to 200 K, lowering the current minimum pressure ratio down to 4:1 for a JT MCC. Previous JT MCC [71] developed were incomplete MCC devices, in which the device would operate in an open loop system using a pressurized gas tank to drive the refrigerant into the system. Additional recent advances by Lewis [39] utilized a closed-loop system with the integration of a miniaturized compressor.

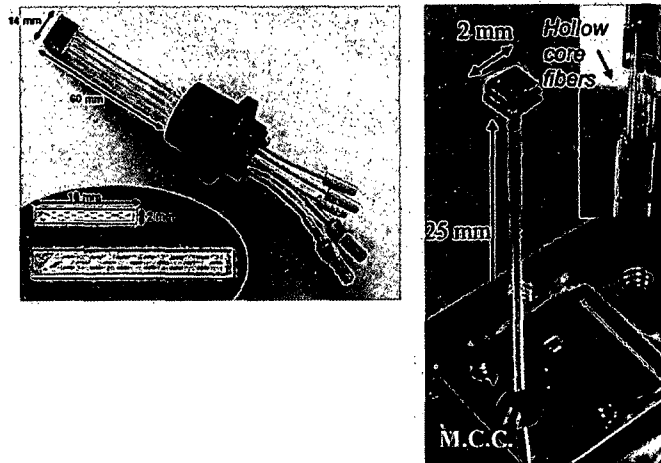


Figure 2-10: Left: JT MCC cold stage developed by Lerou [71]. Right: JT MCC cold stage developed by Ma *et al.* [77].

2.3.1 Joule-Thomson Principle Operation

In a JT MCC system, with the schematic shown in **Figure 2-11**, the gas compressor pressurizes the gas through a counter flow heat exchanger, and heat is exchanged with the low pressure side. The low pressure side absorbs heat from the high pressure side. Isenthalpic expansion occurs as gas from the high pressure line expands through a restriction valve to the low pressure side. The refrigerant changes phase from a liquid to a gas and cools to a low temperature. The cooled liquid goes through the evaporator and absorbs heat from its surroundings where it is interfaced with the electronic component [70]. At this stage, the cooled liquid is heated and is evaporated back into the cold stage line to flow through the counter flow heat exchanger. This cools the high pressure side and the fluid is fed back into the compressor to complete the cycle.

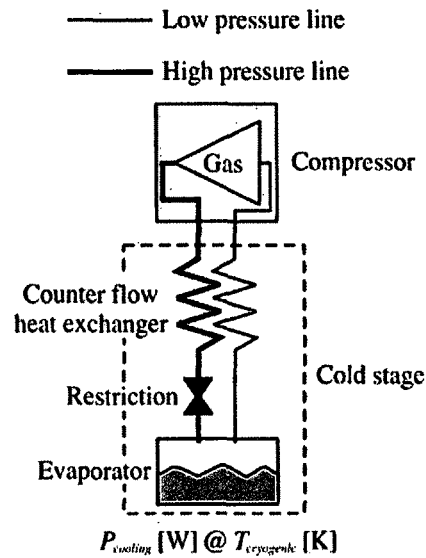


Figure 2-11: Schematic of a Joule-Thomson MCC system [71].

2.3.2 Microcompressor Integration with JT Cooler

Lewis *et al.* [72] successfully integrated a miniature sized compressor to a JT microcooler. Improvement on the mixture of hydrocarbon gas [73], [76] allows for the reduction of maximum operation pressure and pressure ratio to 0.4 MPa and a 4:1 ratio, respectively. Miniaturized oscillator piston pumps and stacked piezoelectric pump have shown to be successfully integrated into a JT MCC system [39], [72]. Check valves were needed to interface and control the gas between the compressor and the JT microcooler. MEMS based fabrication methods were used to produce the microvalves and JT-microcooler components.

Guo *et al.* [78] proposed a conceptual MEMS-based Stirling cooler by utilizing an array of electrostatic diaphragm actuator integrated with the cooling system as shown in **Figure 2-12**. The device can generate 200 kPa with helium. As of

date, the design still remains a concept, due to the challenges in recovering fluid from the cold side to the hot side in an actual device.

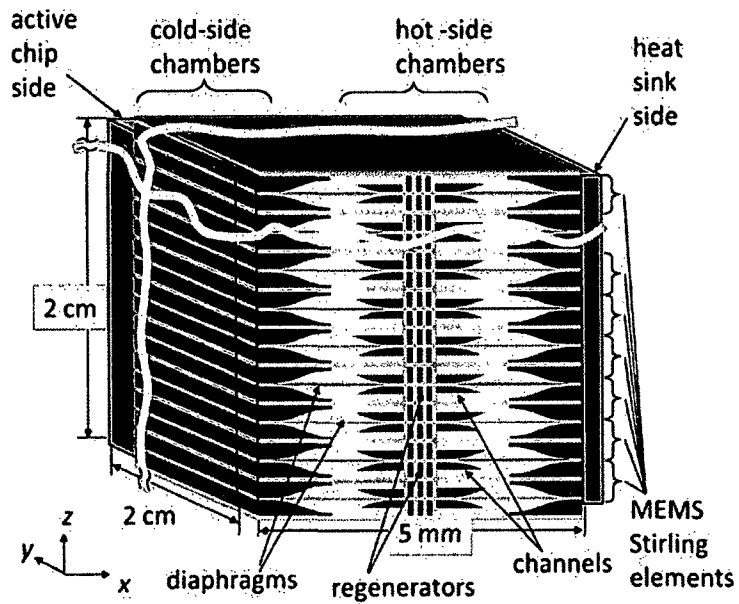


Figure 2-12: The proposed concept of an electrostatic Stirling cooler by Guo [78].

CHAPTER 3

PIEZOELECTRIC DIAPHRAGM ACTUATOR AND TETHER MICROVALVE DESIGN PARAMETERS

The review of the different types of micropumps, microcompressors and components in Chapter 2 allows for various approaches in designing the multistage device. Components such as the stack piezoelectric actuator provide large force generation with very small displacement. Electrostatic actuation requires large voltage to operate against high back pressure. Piezoelectric diaphragm provide small deflection and unknown force generation. Although the force generation from a piezoelectric is unknown, it is well studied and proven to be integrable into a micropump at the microscale.

Microvalves component is also discussed in Chapter 2 with various types, i.e. cantilever, tether and electrostatic types, which are all integrable at the microscale level. The cantilever and tether type belongs in the passive valves category and is less complex to integrate into a microcompressor. There are disadvantages of utilizing these passive valves that rely on the pressure difference to open and close itself, which may result in the reverse leakage and reduction of the flow rate at high frequency operation. However, SU8 tether microvalves is chosen for its ease of microfabrication on a silicon wafer and integration into a machined compressor housing.

This chapter discusses the analysis of the microcompressor components and its design parameters, which consists of a piezoelectric diaphragm and a tether microvalve.

First, a literature review of the various piezoelectric diaphragm configurations and fabrication methods are discussed. Testing, analytical modeling and finite element analysis are performed to characterize the piezoelectric diaphragm volume strokes under static and dynamic conditions. In the second part of this chapter, analytical modeling of the tether microvalve is presented and compared with the experimental result of the pressure-flow relations. Finite element analysis is used to aid in the characterization of the fluid-structure interaction and extract the lumped model parameters of the microvalve.

3.1 Piezoelectric Unimorph Diaphragm

A piezoelectric unimorph diaphragm is composed of a piezoelectric layer bonded to a passive layer as shown in **Figure 3-1**. This type of diaphragm has been widely used for microactuation in micropumps. Consequently, there is a depth of study in literature on this type of microactuator. The diaphragm has been used for micropumps where typical operational frequencies are below 1 kHz of operation. The microcompressor developed in this work utilized high frequency operation to obtain large deflection resulting in larger stroke volume and less dead volume. In this microcompressor design, a \varnothing 20 mm piezodisc buzzer is utilized for the investigation of a multistage microcompressor.

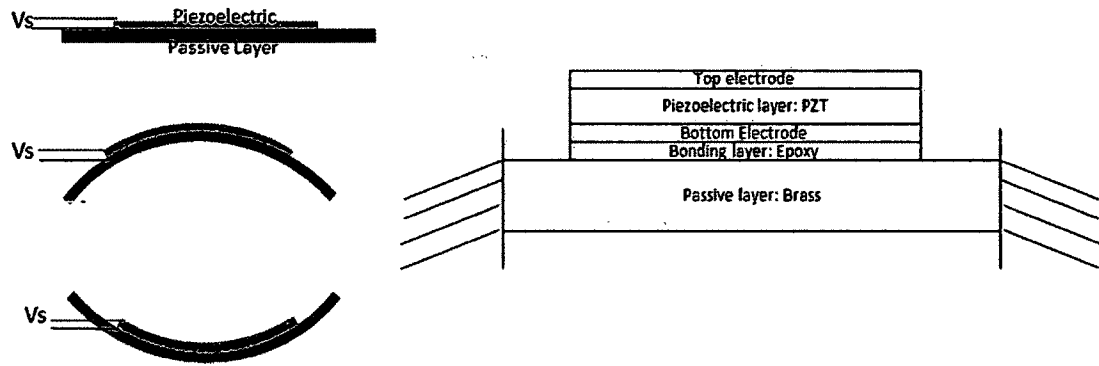


Figure 3-1: Piezoelectric unimorph schematic.

There are several parameters to improve the performance of a unimorph diaphragm design that will be further explained in this chapter. The design parameters include:

1. **Design configuration** – There are several design configurations in literature that are potential candidates in improving the performance of a microscale piezoelectric diaphragm in terms of improving the deflections or force generation.
2. **Design Parameters** – Several researchers developed an analytical model of the diaphragm, and discussed the optimization method to improve its performance through:
 - a. improvement in the piezoelectric material,
 - b. improvement in the synthesis of PZT and the microfabrication method,
and
 - c. geometric design parameters.
3. **Operational Parameters** - Different operational parameters affect the performance of the diaphragm and can improve the diaphragm's performance such as the:

- a. drive voltage,
- b. resonant frequency, and
- c. pressure load.

3.1.1 Piezoelectric Unimorph Diaphragm Principle of Operation

For a piezodisc, there is an adhesive layer to bond the piezoelectric layer to the passive layer. Thin layers of electrode exist at the top and bottom of the piezoelectric. The bending of the diaphragm occurs when voltage is applied to the top and bottom electrode of the piezoelectric generating an electric field in the z-direction, the piezoelectric material strained in the both z and radial direction. The piezoelectric material is bonded to the passive layer; therefore, the strain in the radial direction generates a bending moment on the passive layer. Applied alternating voltage causes the piezoelectric to contract and elongate in the radial direction, generating bending in an upward or downward direction as shown in **Figure 3-1**.

3.1.2 Literature Review of Piezoelectric Diaphragm Design Configuration

Piezoelectric unimorph diaphragm is known to generate small deflections, which can lead to small stroke volume compromising the pressure ratio of the microcompressor. A 9 mm x 9 mm x 200 μm square PZT-silicon unimorph diaphragm developed for a micropump by Feng and Kim [5] generated a maximum deflection of 6 μm at 200 V Hong *et al.* [79] generated a larger deflection of 7 μm using interdigitated PZT diaphragm (at 100 V) with only a 800 μm diameter diaphragm. The diaphragm stroke was limited to 10 kPa of pressure load. There have been several designs to improve the performances of a piezoelectric unimorph diaphragm.

Yao *et al.* [80] developed a multimorph piezoelectric actuator which consists of multiple layers of piezoelectric to increase the force generated to bend the passive later actuator, increasing the displacement and resonant frequency of the actuator. Although the actuator was designed as a cantilever, multilayer composition can be utilized for a diaphragm with the same benefit. Another method is to design a unimorph diaphragm with a low Young's modulus passive layer to increase the flexibility of the diaphragm. The piezoelectric microspeaker developed by Cho *et al.* shown in **Figure 3-2** utilized a polyimide material and PZTs at the outer quadrant of the membrane. This added low residual stress and produced large displacement. Flexible material such as polyimide material can reduce the high pressure load the diaphragm can withstand.

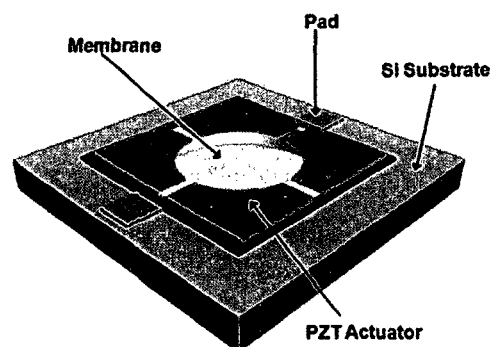


Figure 3-2: Polyimide piezoelectric membrane [81].

Interdigitated electrodes (IDE) have been recently developed as another form to generate bending in piezoelectric unimorph cantilevers [82] and diaphragms [79], [83], [84]. This design takes advantage of the piezoelectric constant in the d_{33} mode by removing a bottom electrode layer and placing the electrode on the same plane with the top electrode with an interdigitated spacing as illustrated in **Figure 3-3**, where both electrodes are shaped and spaced in a comb like manner. The interdigitated electrodes

create an electric field in the lateral direction for a cantilever case and the radial direction of the circular membrane. Since the electric field generated is in the parallel or radial direction, the resulting piezoelectric coupling coefficient utilizes the d_{33} mode.

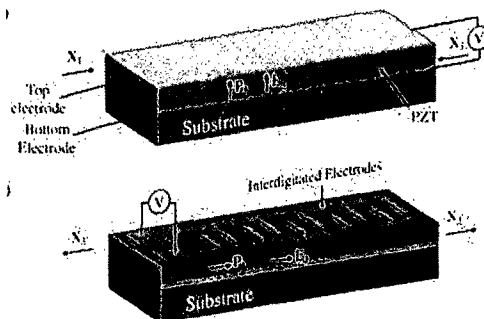


Figure 3-3: Illustration of interdigitated piezoelectric cantilever [85].

The d_{ij} constant is the ratio of the free strain to the applied electric field, where i is the direction that the electric field is applied and j is the utilized direction for the displacement or force of the piezoelectric. Hong *et al.* [79] noted the circular IDE piezoelectric actuation for the circular membrane in **Figure 3-4** generated strain in the, d_{31} and d_{33} mode. The d_{33} constant is typically 2-3 times larger than the d_{31} constant. Myer *et al.* [84] developed a 650 μm diameter IDE PZT unimorph membrane and achieved center deflection of 10 μm .

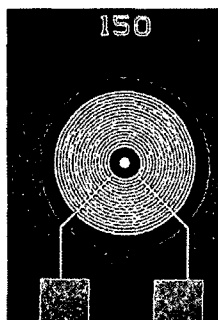


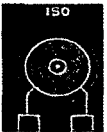




Figure 3-4: IDT unimorph diaphragm developed by Hong *et al.* [79].

Thus, numerous variations of piezoelectric diaphragms have been analyzed and tested for different application purposes, i.e. micropumps, microphones and microtransformer applications. A summary of the various types of piezoelectric diaphragm actuators is given in **Table 3-1**. Each of these piezoelectric diaphragm are designed either specifically to increase the resonance frequency [86], displacement, or generate large pressure output [81].

Table 3-1: Summary of different types of piezoelectric actuators.

Author	Description	Material layers	Ri	Ro	Deflection	Voltage
Cho [82] 	Square with PZT at outer edges	PZT/ Polyimide		2 mm	large displacement	
Feng [5] 	Square 8 x 8 mm ² , unimorph	PZT/ silicon			6 μm	200
Hong [80] 	Circular, interdigitated	PZT/ silicon oxide		800 μm	7 μm	100
Myer [85] 	Circular, interdigitated	PZT/ silicon oxide	150 μm	650 μm	7 μm	180
Yao [81] 	Rectangular Multilayer Bimorph	PZT/ Al ₂ O ₃				

3.1.3 Piezoelectric Material

Lead Zirconate Titanate (PZT) is commonly employed as the piezoelectric layer due to its higher transverse piezoelectric constant, d_{31} of around -190 pC/N. Other piezoelectric materials such as Aluminum Nitride (AlN) and ZnO have lower values of -1.3 pC/N and -2.87 pC/N, which will result in smaller deflection magnitude. These materials can be grown with a low sputtering temperature (300°C), making it suitable to

deposit more of a flexible layer such as a polymer material that has low glass transition temperature. PZT requires a high anneal temperature of 650°C to epitaxially crystallize the perovskite structure of PZT. This is beyond the melting temperature of most flexible polymers. Therefore, a transfer process is required and involves removing the thin film PZT from the substrate and attaching it to the plastic substrate.

3.1.4 PZT Synthesis and Fabrication of Piezoelectric Review

Currently, the methods to deposit PZT on diaphragm are: sol gel [87]–[90], screen print [90]–[93], aerosol [94] and direct-write [95]. Currently, the two main methods feasible for micro size integration feasible allow fast and low cost manufacturing processes are sol gel and screen printing.

The sol gel method [87], [89], [96] provides a maximum layer thickness of up to 1 μm and requires a maximum deposition of 250 nm layer thickness at a time via spin coating and rapid annealing temperature at around $\sim 600^\circ\text{C}$ range. The screen print method [90], [97]–[99] requires a screen mesh and a squeegee to apply the PZT paste on a substrate as illustrated in **Figure 3-5** to pattern the PZT directly without etching. This method provides thicknesses in the 20-110 μm range.

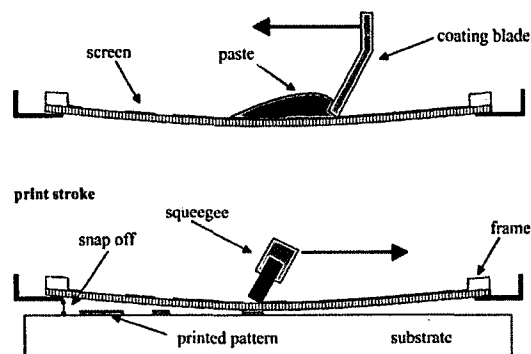


Figure 3-5: Schematic of screen printing PZT [100].

The aerosol method [94], [101] deposit PZT at room temperature and is annealed at high temperature to form PZT on a substrate with thicknesses ranging from 1-500 μm . PZT particles in the submicron range are mixed with a carrier gas such as helium to form an aerosol through a nozzle and depositing the PZT on the substrate surface. Liftoff method is used to form a patterned PZT microstructure. Direct-write method can utilize sol-gel [95] or PZT paste [93] using a deposition pen such as a MicroPen™ to deposit complex pattern of the PZT on a 2D surface producing thickness comparable to screen printing. This method is cheaper, but more suitable for small-scale production.

3.1.5 Diaphragm Geometric Design Optimization Parameters

The piezoelectric unimorph diaphragm generates the stroke volume in the compressor chamber. Therefore, it is an integral part in the generation of the compressor pressure. Mo *et al.* [102] and Herz *et al.* [103] studied the geometric optimization of a piezoelectric unimorph diaphragm to maximize the volume stroke. The optimized thickness ratio was determined analytically by Herz using the classical laminate plate theory (CLPT). For a pin support at the outer edge of the actuator, the optimal thickness ratio is given as

$$\frac{T_p}{T_d} = \sqrt{\frac{Y_d}{Y_p}} \quad [103] \text{ Eq. 3-1}$$

where T_p and T_d is the piezoelectric thickness and diaphragm thickness, and Y_d and Y_p is the Young's modulus for the diaphragm and piezoelectric, respectively. Herz also points out that maximizing the radius of the piezoelectric layer to the radius of the passive layer will maximize the stroke volume. This is limited by the clamp area and strain at the outer rim of the diaphragm.

The CPLT method provides the stroke volume of the actuator as a function of the input voltage to the piezoelectric layer and the pressure load on the actuator given as

$$V_{stroke} = C_P P + C_E V \quad [103], [104] \text{ Eq. 3-2}$$

where C_P and C_E is the fluidic capacitance and volumetric-electrical coupling. P is the pressure load on the diaphragm and V is the input voltage to the piezoelectric material.

These coefficients are calculated in Appendix A using the CLPT method from Desphande [104].

3.1.6 Diaphragm Test Characterization

To characterize the piezoelectric diaphragm, the following analysis method are conducted:

- 1) **Quasi-static:** Due to the limitation in the availability of the experimental measurement in measuring the deflection profile of the piezoelectric diaphragm. Furthermore, a Laser Doppler Vibrometer (LDV) can only measure the dynamic deflection of the diaphragm. Thus, FEA and the CLPT method are used both to determine the deflection profile of quasi-static study and used to validate their results.
- 2) **Dynamic analysis:** The piezoelectric diaphragm operates in the dynamic mode at high frequencies to generate the stroke. A frequency sweep of the diaphragm center deflection is determined with FEA and compared against the frequency sweep measurement of the LDV to determine its accuracy.

Due to the limitation of the two mode of analyses, the stroke volume at the resonance peak is determined by correlating the center magnitude of static deflection profile to the dynamic measurement of the center deflection peak.

The diaphragm is modeled using a quasi-static analysis with input voltage to the top and bottom electrode of the piezoelectric. The thin layer of electrodes and the bonding layer between the piezoelectric and passive layer were neglected in the FEA analysis to simplify the meshing to provide easier convergence. **Figure 3-7(b-c)** illustrate a clamp plate and an O-ring for the mounting that represent the compressor and test fixture. A simplified fixed constraint model is used at the outer radial surface of the diaphragm as illustrated in **Figure 3-7(a)** for the FEA model and CLPT model. Static pressure load was also applied to the diaphragm.

A commercially available piezo disc bender in **Figure 3-6** with parameters from **Table 3-2** is used as the diaphragm actuator for the microcompressor.

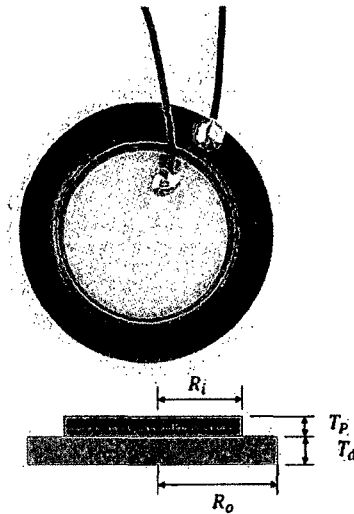
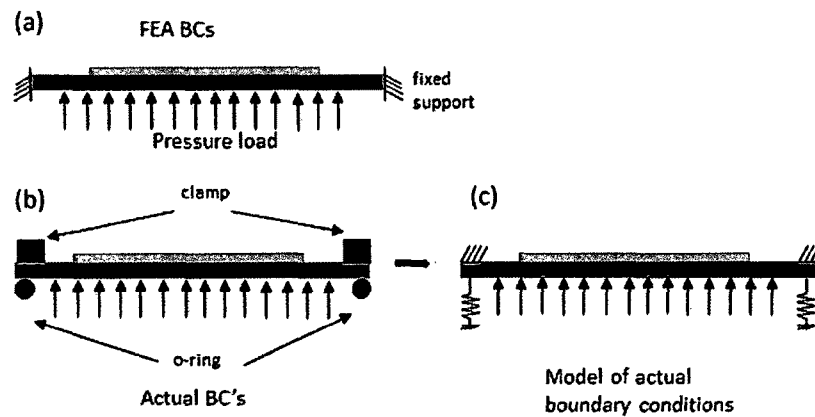


Figure 3-6: Piezo disc diaphragm actuator.

Table 3-2: Piezo disc parameters.

	R_i (mm)	R_o (mm)	T_p (mm)	T_d (mm)	d_{31} (C/N)	Y Young's Modulus (GPa)
PZT-5A	7.5	-	0.21	-	-	63
Brass	-	10	-	0.21	175×10^{-12}	110

**Figure 3-7:** Boundary conditions (BCs) for the piezoelectric diaphragm.

A test rig in **Figure 3-8** was used to characterize the diaphragm deflection in response to the applied voltage and drive frequency using a Polytec LDV. A pressure manometer was used to measure the pressure load in the chamber generated from the syringe pump. A LDV was used to measure the center diaphragm deflection. An O-ring seal was installed to replicate the actual compressor design and seal the diaphragm under air pressure load.

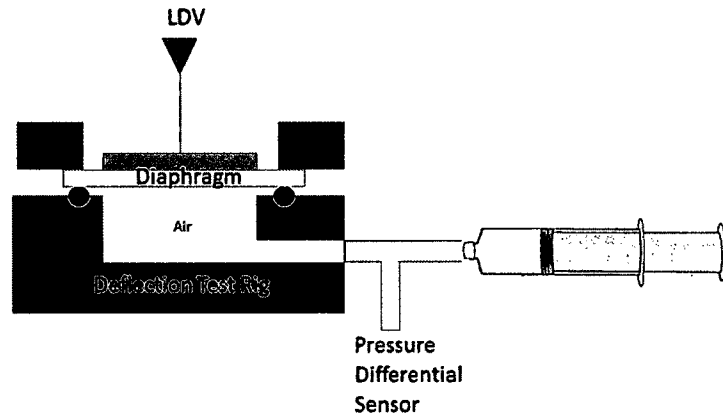


Figure 3-8: Unimorph diaphragm deflection test setup.

It is difficult to measure the deflection profile of the diaphragm from a single point measurement using a LDV without a 2D or 3D surface laser profilometer to determine the stroke volume of the actuator. Additionally, the stroke volume of the diaphragm from a static analysis may be different from the dynamic stroke volume as observed in **Figure 3-11**, where the deflection change as a function of the drive frequency. FEA and the CLPT analysis offers a quasi-static deflection profile of the diaphragm. Details of the CLPT analysis is given in Appendix A with the deflection plot given in **Figure A-1**. These deflections depends on the voltage and the pressure load given in [103], [104] **Eq. 3-2**. From **Figure 3-9**, the static deflection of the brass-PZT disc requires 400 V to achieve 35 μm of center deflection. Additionally, from **Figure 3-10**, it can be seen that the diaphragm can only withstand up to 10 kPa of pressure load at 60 V of static actuation before collapsing under pressure.

The percentage difference between the results CLPT and FEA results are summarized in **Table 3-3** and **Table 3-4** for **Figure 3-9** and **Figure 3-10**, respectively. The percent difference is compared at the center deflection of the piezoelectric

diaphragm, and the two methods are within a 5% difference except where the diaphragm experienced 10 kPa of pressure load, which resulted in a 28.9% difference. Note that the magnitude for the deflection at 10 kPa is only 0.4 μm difference between the two methods. Due to the small magnitude in the deflection of only 0.128 and 0.165 μm , the 0.4 μm contribute to a larger percent difference.

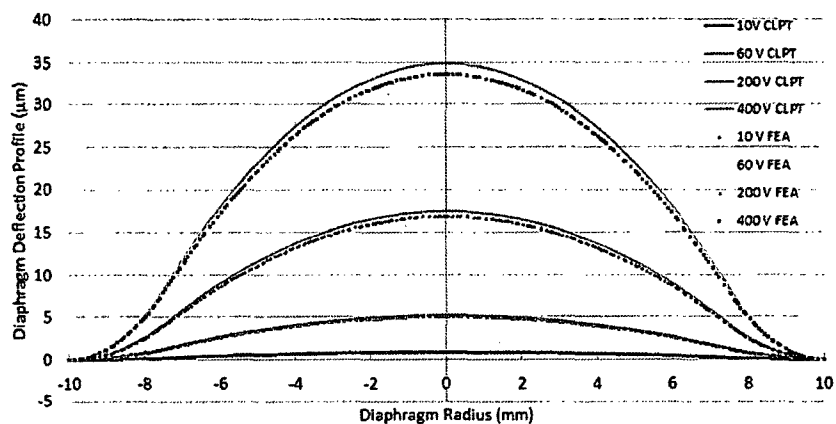


Figure 3-9: Static analysis of piezoelectric unimorph diaphragm deflection profile comparing FEA and CLPT method at zero pressure load.

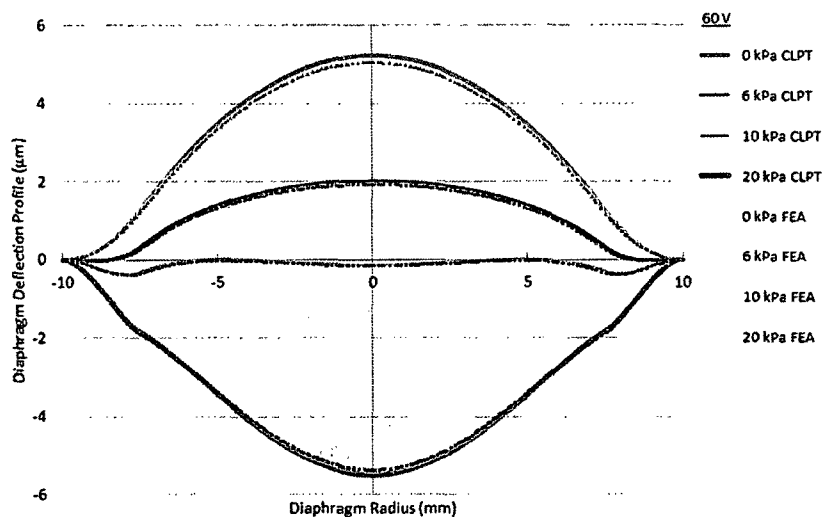


Figure 3-10: Static analysis of piezoelectric unimorph diaphragm deflection profile comparing FEA and CLPT method under pressure load at 60 V

Table 3-3: Comparison of the results from **Figure 3-9** of the center deflection magnitude.

Voltage (V)	CLPT (μm)	FEA (μm)	% Difference
10	0.872	0.84	3.7%
60	5.23	5.04	3.6%
200	17.4	16.8	3.4%
400	34.89	33.63	3.6%

Table 3-4: Comparison of the results from **Figure 3-10** of the center deflection magnitude under pressure load.

Under Load, at 60 Vpp			
Pressure (kPa)	CLPT (μm)	FEA (μm)	% Difference
0	5.23	5.04	3.6%
6	2.01	1.91	5.0%
10	-0.128	-0.165	-28.9%
20	-5.49	-5.377	2.1%

3.1.6.1 Diaphragm Frequency Response

Due to the dynamic cycling operation of the actuator in the compressor, a dynamic analysis is needed to determine the dynamic stroke volume. A frequency response of the diaphragm, gives a more accurate evaluation of the stroke deflection during compressor operation. With the same test rig as set up in **Figure 3-8**, and without pressure load from the syringe pump, the deflection of the diaphragm was measured at different frequencies. **Table 3-5** shows the summary of the FEA and experimental frequency response; the FEA results shows a 3.37% difference in the center deflection

magnitude from the experimental and a 9.3% difference in the peak frequency from the experimental.

Table 3-5: Summary of piezoelectric diaphragm frequency response analysis.

	Frequency (Hz)	Center Deflection (μm)
FEA	4700	55.2
Experimental	4300	53.4
Percentage Error	9.30%	3.37%

The diaphragm achieved 55 μm peak-to-peak deflection at near the resonant frequency as shown in **Figure 3-11**. This is close to the frequency response of the FEA analysis of the diaphragm, where the simulated modal frequency response is 4.72 kHz. The small shift in frequency can be contributed to the boundary condition of the constraint difference of the diaphragm and the exact material properties of the piezo disc.

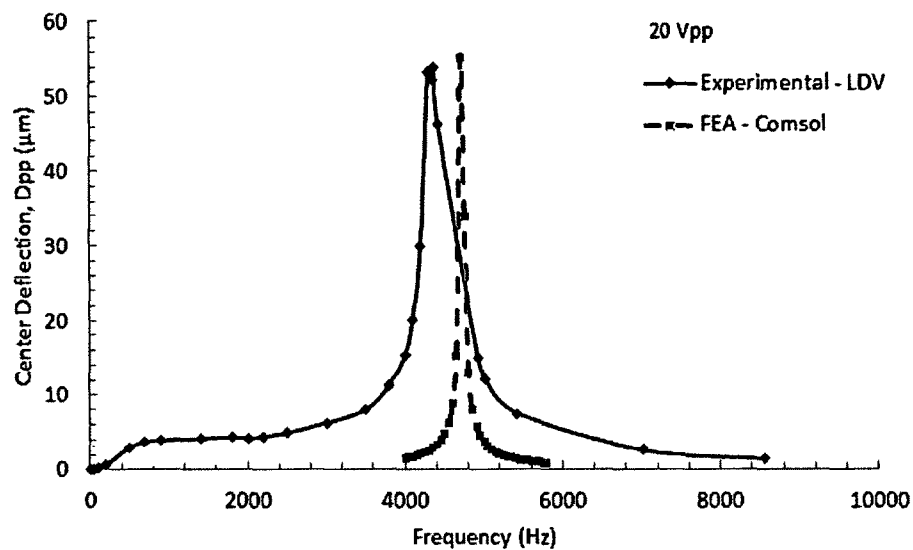


Figure 3-11: Frequency response of the diaphragm deflection at resonant frequency driven at 20 Vpp with no pressure load.

The diaphragm behaves like a membrane, and the resonance frequencies is given as

$$w = \frac{\alpha}{2\pi R^2} \sqrt{\frac{D}{\rho h}} \quad [86] \text{ Eq. 3-3}$$

where w is the angular resonant frequency, α is the constant for the vibration mode, R is the radius, h is the membrane thickness, ρ is membrane density, D are flexural rigidity given as

$$D = \frac{Eh^3}{12(1 - \nu^2)} \quad [86] \text{ Eq. 3-4}$$

where E is the Young's modulus and ν is the Poisson's ratio.

To determine the dynamic stroke volume, the static deflection profile is extrapolated to match the measured dynamic deflection. The stroke volume is determined in **Figure 3-12**.

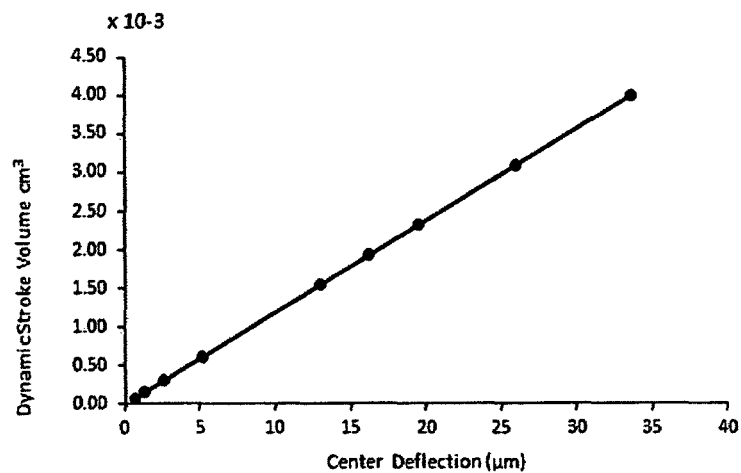


Figure 3-12: Extrapolated dynamic stroke volume

The diaphragm also experienced pressure generated in the chamber and generated back pressure from its outlet port. **Figure 3-13** shows the deflection characteristics of the diaphragm deflection under pressure load using the test set up in **Figure 3-8**. Pressures in the test rig was loaded with a pump syringe up to a maximum of 35 kPa at 40 Vpp. Pressure beyond 30 kPa load resulted in a fast leak rate from the syringe and the O-ring seal, causing inaccurate and unsteady pressure reading from the manometer. Here, 500 Hz was first tested to get a base comparison under non-resonance dynamic mode. The deflection at 500 Hz can operate up to 10 kPa and can no longer deflect at higher pressure. Note that at resonance, the deflection follows a similar horizontal trend line up to 10 kPa and can still generate deflection at higher pressure. Frequency of 4.18 kHz and 4.14 kHz were tuned with the largest deflection under pressure load. At resonance, the diaphragm maintained its stroke volume up to 10 kPa and has a maximum deflection at 15 kPa. At a larger load of more than 15 kPa, the diaphragm shows a more decreasing trend after 15 kPa up to 30 kPa.

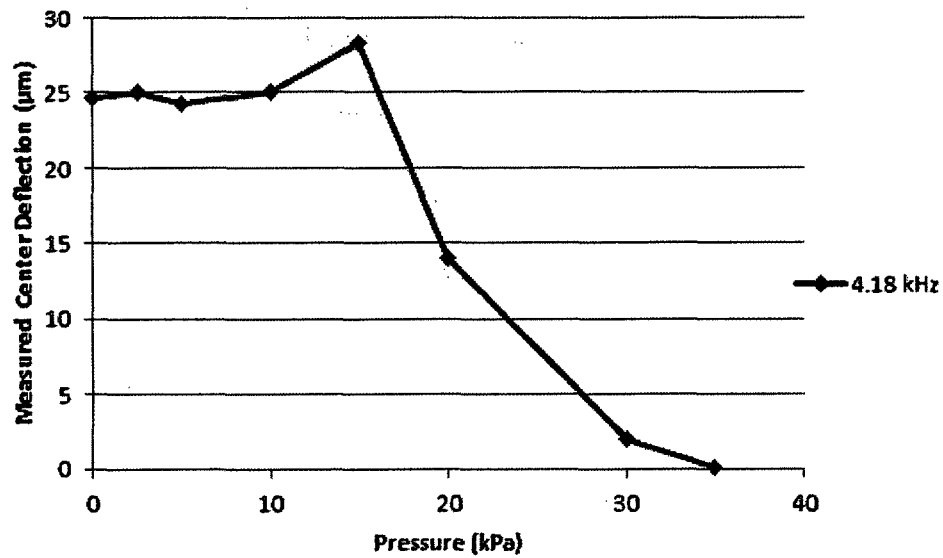


Figure 3-13: Preliminary measured center deflection of piezoelectric diaphragm under pressure load.

3.2 Microvalve Model and Design

The microvalve design is based on a tether check valve designed as shown in **Figure 3-14** fabricated using MEMS microfabrication technique as described in Chapter 5. Here, modeling and characterization of the microvalve and its interaction with the gas flow are discussed. Modeling and FEM analysis allow for the development of lumped model parameters of the microvalve. A 2D illustration of the microvalve model is shown in **Figure 3-15**. The tether valve is designed with SU8 material with its parameters given in **Table 3-6**.

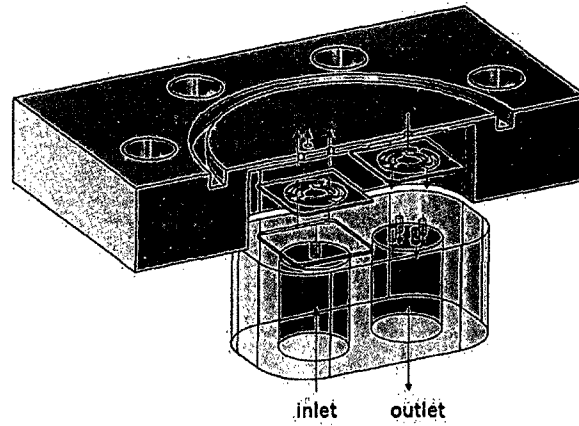


Figure 3-14: Microvalve model.

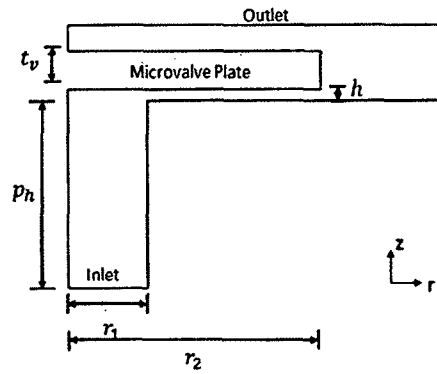


Figure 3-15: 2D schematic of microvalve model.

Table 3-6: Microvalve parameters.

r_1 (mm)	r_2 (mm)	t_v (μm)	p_h (mm)	h (μm)
0.5	0.8	100	0.7	10

3.2.1 Flow Conditions

To develop the model for air flow through a small opening of the microvalve, certain flow conditions is assumed. In the micro scale, the fluid flow is typically laminar

with low Reynolds number. The Reynolds number is given as the ratio of the inertia force over the viscous force or friction of the air flow and is given as:

$$Re = \frac{\rho \bar{U} L}{\vartheta} \quad \text{Eq. 3-5}$$

where ρ , \bar{U} , L , ϑ is the fluid density, mean fluid velocity, characteristic length of the surface, and dynamic viscosity. For a non circular diameter, the characteristic length is the hydraulic dynamic given as

$$D_h = \frac{4 A}{P_w} = \frac{4(2\pi r h)}{2(2\pi r)} = 2h \quad \text{Eq. 3-6}$$

where A and P_w is the cross section area of the channel or fluid flow, and P_w is the wetted perimeter. The mean velocity is defined as

$$\bar{U} = \frac{Q}{A} = \frac{Q}{2\pi r h} \quad \text{Eq. 3-7}$$

where Q is the volumetric flow rate and A is the cross sectional area of the flow.

The Reynolds is rewritten as

$$Re = \frac{\rho \bar{U} D_h}{\vartheta} \quad \text{Eq. 3-8}$$

To determine the Reynolds number, the pressure-flow rate relationship through the valves is needed. Once the pressure-flow rate relationship is described, further discussion of the Reynolds # is presented in the later section.

The compressibility of the air flow is determined by the Mach number given as

$$M = \frac{\bar{U}}{c} \quad \text{Eq. 3-9}$$

where c is the speed of sound.

Using **Eq. 3-7**, the Mach number can be given in terms of the flow rate through the valve and can be rewritten as

$$M = \frac{Q}{c2\pi rh} \quad \text{Eq. 3-10}$$

For $M < 0.3$, the flow is still considered incompressible. The Mach number of the design is revisited in the next section.

3.2.2 Pressure-Flow Rate Model

The flow between the valve plate and the lower surface is considered as a fully developed, radial flow between parallel plates. The applicable steady flow Navier Stokes equations for radial momentum and continuity equations [105], [106] are

$$\frac{\partial p}{\partial r} = \mu \left(\frac{\partial^2 u}{\partial r^2} + \frac{1}{r} \frac{\partial u}{\partial r} - \frac{u}{r^2} \frac{\partial^2 u}{\partial z^2} \right) \quad \text{Eq. 3-11}$$

$$\frac{\partial u}{\partial r} + \frac{u}{r} = 0. \quad \text{Eq. 3-12}$$

The velocity flow is assumed a parabolic profile for the flow between two radial parallel plate starting the entrance to the outer edge of the valve plate at $r_1 < r < r_2$. No slip boundary conditions is applied, where the $u(z = 0)$ and $u(z = h) = 0$.

$$u = \frac{3Q}{\pi rh} \left(\frac{z}{h} \right) \left(1 - \frac{z}{h} \right) \quad \text{Eq. 3-13}$$

The **Eq. 3-11** to **Eq. 3-13** that yield the pressure difference along the radius of the parallel valve plate is

$$p(r_2) - p(r_1) = \xi_1 \frac{6\mu Q}{\pi h^3} \ln \frac{r_2}{r_1} - \xi_2 \frac{\rho Q^2}{4\pi^2 h^2 (r_2 + r_1)^2}. \quad \text{Eq. 3-14}$$

Thus, the pressure drop is contributed from the friction loss and the inertia loss, where the first term, $\xi_1 \frac{6\mu Q}{\pi h^3} \ln \frac{r_2}{r_1}$, is the viscous effect and the second term, $-\xi_2 \frac{\rho Q^2}{4\pi^2 h^2 (r_2 + r_1)^2}$, is the

inertia effects of the flow. If the inertia effect has a smaller order of magnitude than the viscous effect, then the inertia term can be ignored. ξ_1 and ξ_2 are the loss coefficients that have to be determined from experimental data. Here, the loss coefficients are determined from numerical simulation with FEM and are discussed in section 3.2.3.1.1.

It can be seen that **Eq. 3-14** is comparable to the Bernoulli's equation in **Eq. 3-15** and is rewritten to **Eq. 3-16**.

$$p_1 + \alpha \frac{\rho U_1^2}{2} = p_2 + \alpha \frac{\rho U_2^2}{2} + p_L \quad \text{Eq. 3-15}$$

$$\Delta p = p_L + \alpha \frac{\rho(U_2^2 - U_1^2)}{2} \quad \text{Eq. 3-16}$$

where p_L is the viscous loss due to friction and the second term is the inertia loss.

Given by the Hagen-Poiseuille law, the resistance [107] of the microvalve is given as

$$R = \frac{\Delta P}{Q} \quad \text{Eq. 3-17}$$

where ΔP is the pressure drop and Q is the flow rate. The resistance is

$$R = \frac{\xi_2 6\mu \ln\left(\frac{r_2}{r_1}\right)}{\pi h^3}. \quad \text{Eq. 3-18}$$

The total load of the gas acting on the bottom surface of the valve plate can be found by integrating the pressure distribution from the integration of the curve in **Eq. 3-14**. The force load, W , is given as

$$W = p_{in} \pi r_1^2 + 2\pi \int_{r_1}^{r_2} p dr \quad \text{Eq. 3-19}$$

$$W = 3\mu(r_2^2 - r_1^2) \frac{Q}{h^3}. \quad \text{Eq. 3-20}$$

3.2.3 Microvalve Fluid-Structure Characterization

The modeling of the fluid structure interaction of the microvalve is modeled with two approaches using the quasi-steady flow:

3.2.3.1 Quasi-Steady Flow Through a Fixed Valve Plate

The first approach is the analysis of a quasi-steady flow through a fixed plate at height, h_1 as shown in **Figure 3-16**: Schematic of the pressure-flow through the microvalve fixed-plate model with an initial gap height, h_1 . The inlet pressure generates a steady air flow with a load, W , on the fixed valve plate. Here, the initial condition of our assembled valve is modeled where the applied UV adhesive layer leaves an initial gap height, h_1 , between the valve plate and the valve seat.

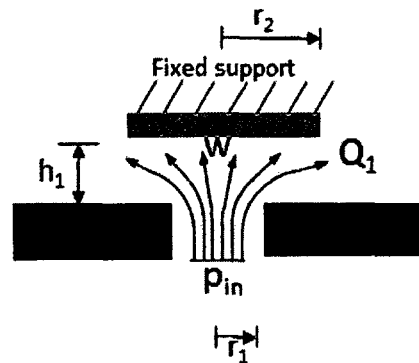


Figure 3-16: Schematic of the pressure-flow through the microvalve fixed-plate model with an initial gap height, h_1 .

The pressure-flow relation [108] is given as

$$Q_1 = \frac{\pi h_1^3 p_{in}}{\xi_1 6 \mu \ln \left(\frac{r_2}{r_1} \right)}. \quad \text{Eq. 3-21}$$

The flow rate, Q_1 , at different gap height, h_1 , is plotted in **Figure 3-17**.

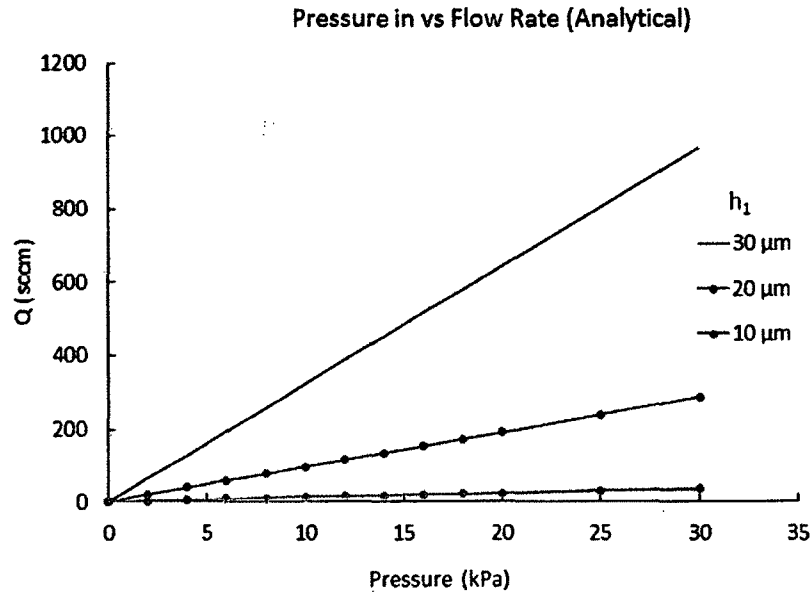


Figure 3-17: Calculated flow rate from Eq. 3-21 with $\xi = 1$.

The Reynolds number through valve structure at various fixed gap heights is observed. The Reynolds number in **Figure 3-18** is estimated with Eq. 3-21 without the loss coefficient calculated at the entrance radius, r_1 . A Re number < 2100 indicates laminar flow, and it can be seen that the flow remains laminar for the gap height parameters in **Figure 3-18**. From **Figure 3-19**, compressible and incompressible flow condition can be considered at different conditions. The incompressible flow exists at gap height, $h < 10 \mu\text{m}$. At a gap height of $20 \mu\text{m}$ with inlet pressure below 15 kPa, the flow remains incompressible. Thus, the analysis conducted in this dissertation considers the flow to be incompressible. At a larger gap height, the modeling results is expected to deviate from this model. Analysis for a compressible flow model is beyond the scope of the study.

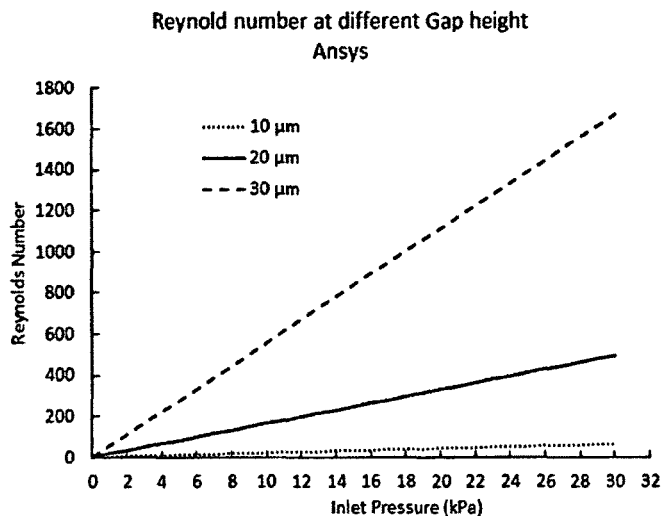


Figure 3-18: Reynolds number for air flow through microvalve.

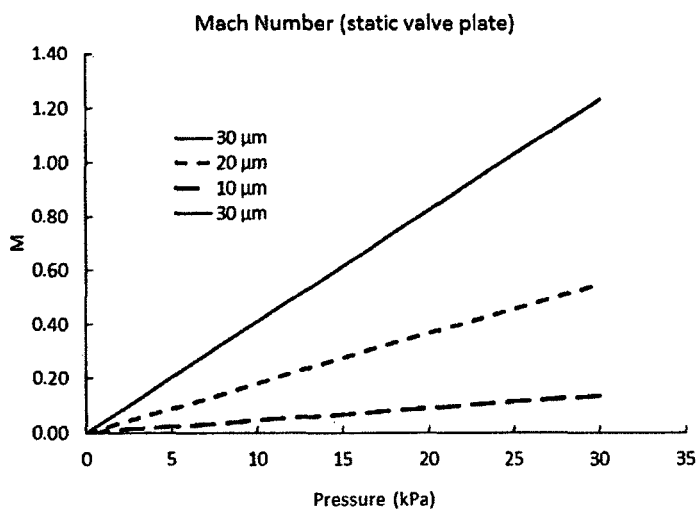


Figure 3-19: Mach number at different gap height with a fixed valve plate height.

3.2.3.1.1 Viscous and Inertia Effect

The quasi-steady pressure-flow relation of the microvalve fixed-plate model in terms of its viscous and inertia effects is given in Eq. 3-14. Since the Reynolds number gives the ratio of the inertia effect over the viscous effect, it can give a good indication of

when the inertia effect would be significant in the microvalve model. To examine these effects contributing to the pressure loss of the microvalve flow without knowing the loss coefficient factor, ξ , the viscous and inertia effects are plotted **Figure 3-20** and **Figure 3-21**. To plot these figures, it is first assumed that the derived model from **Eq. 3-14** is a perfect model representation of the pressure-flow through the microvalve orifice by assuming $\xi_{1,2} = 1$. From the two figures, the viscous effect has one order of magnitude larger than the inertia effect at a low gap height of $h < 30 \mu\text{m}$. Thus, at a low gap height, the viscous effect is more significant. At $h > 30 \mu\text{m}$, the magnitude of the pressure loss from the viscous effect decreases and reaches closer to the order of magnitude of inertia effect at the same gap height. Similarly, the Reynolds number from **Figure 3-18** has a larger magnitude at a larger gap height, indicating that the inertia effect is more significant as the gap height increases.

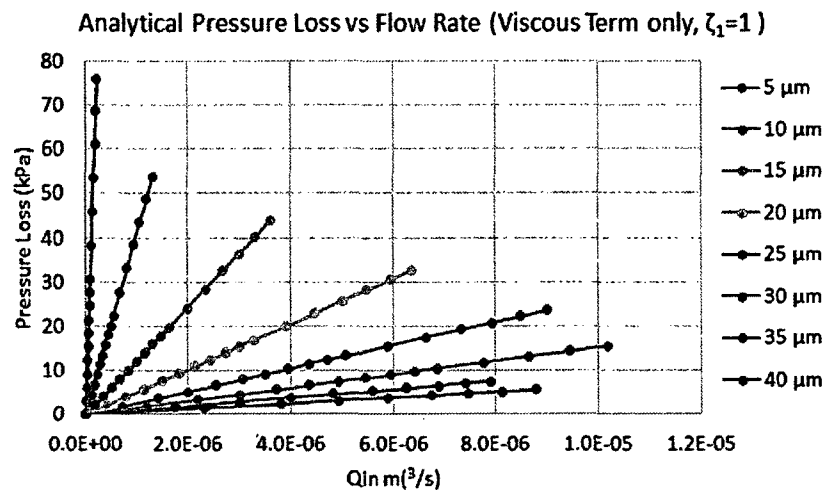


Figure 3-20: Plot of the pressure loss due to viscous effect from the fixed microvalve model.

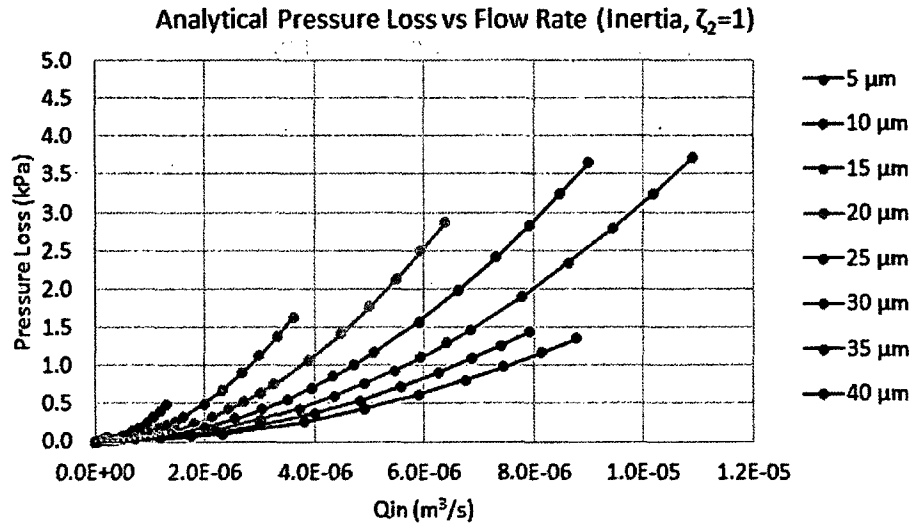


Figure 3-21: Plot of the pressure loss due to inertia effect for the fixed microvalve model.

3.2.3.1.2 Microvalve Fixed-Plate Model Comparison with FEM

Figure 3-22 shows a plot of the quasi-steady flow relations using FEM analysis. The FEM results is then compared to the analytical pressure-flow curves in **Figure 3-23**. At a low gap height, $h < 15 \mu\text{m}$, the simulated flow is linear and fits the analytical model. As the gap height increases, $h > 20 \mu\text{m}$, the FEM results show a nonlinear pressure-flow relation. As mentioned in the previous section, at a large gap height, the viscous effect is smaller contributing to a smaller pressure loss. At a larger height, the fluidic resistance is less, and allowing increase in gas flow velocity. The gas flow velocity contributes to the inertia effect in pressure loss at the large gap height.

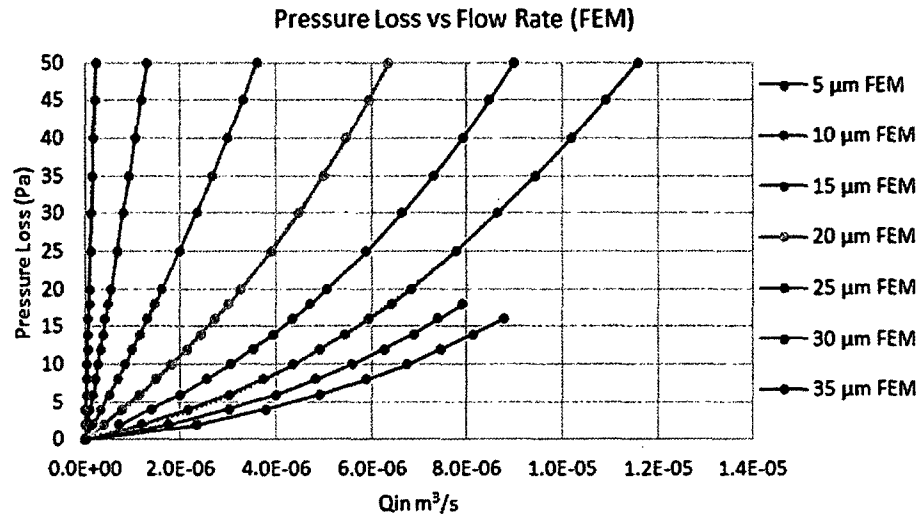


Figure 3-22: Pressure loss from the microvalve at different gap height and flow rate from FEM analysis. These curves are fitted with second order polynomial to determine the viscous and inertia loss coefficient.

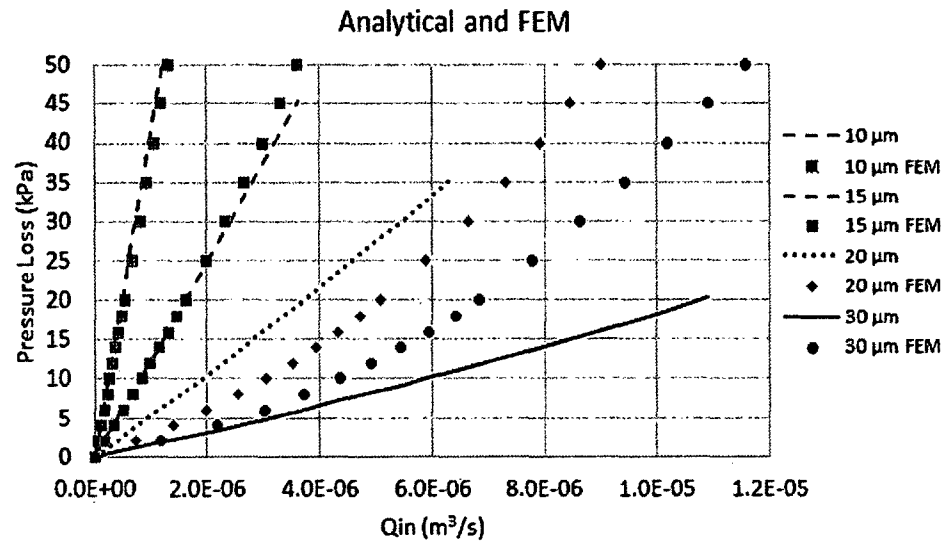


Figure 3-23: Flow rate vs. pressure of steady flow through microvalve. Comparison between analytical and FEM result.

The FEM result of the pressure-flow relations is replotted in **Eq. 3-25** and is fitted as a second order polynomial. The pressures difference along the valve plate from **Eq. 3-14** is rewritten as

$$p_L = a_1 Q + a_2 Q^2 \quad \text{Eq. 3-22}$$

$$\xi_1 = \frac{a_1}{\frac{6\mu}{\pi h^3} \ln \frac{r_2}{r_1}} \quad \text{Eq. 3-23}$$

$$\xi_2 = \frac{a_2}{\frac{\rho}{4\pi^2 h^2 (r_2 + r_1)^2}} \quad \text{Eq. 3-24}$$

By using a second order polynomial fit from **Eq. 3-22** to fit the pressure-flow curves in **Figure 3-22**, the coefficients a_1 and a_2 are obtained for each curve given in **Table 3-7**. The loss factors, ξ_1 and ξ_2 given in **Figure 3-24** and **Figure 3-25**, are determined from a_1 and a_2 using **Eq. 3-23** and **Eq. 3-24**. The loss factors ξ_1 and ξ_2 are determined from **Table 3-7**. With these parameters, the analytical pressure-flow relation for a 30 μm gap height is adjusted to match the FEM result as shown in **Figure 3-26**.

Table 3-7: Pressure-flow polynomial fitted coefficients

h (μm)	a_1	a_2	ξ_1	ξ_2
5	2.00E+11	1.00E+16	0.61	8.88
10	4.00E+10	2.00E+15	0.97	7.11
15	1.00E+10	8.00E+14	0.82	6.40
20	4.00E+09	5.00E+14	0.78	7.11
25	2.00E+09	4.00E+14	0.76	8.88
30	9.00E+08	3.00E+14	0.59	9.59
35	7.00E+08	2.00E+14	0.73	8.70
40	4.00E+08	2.00E+14	0.62	11.37

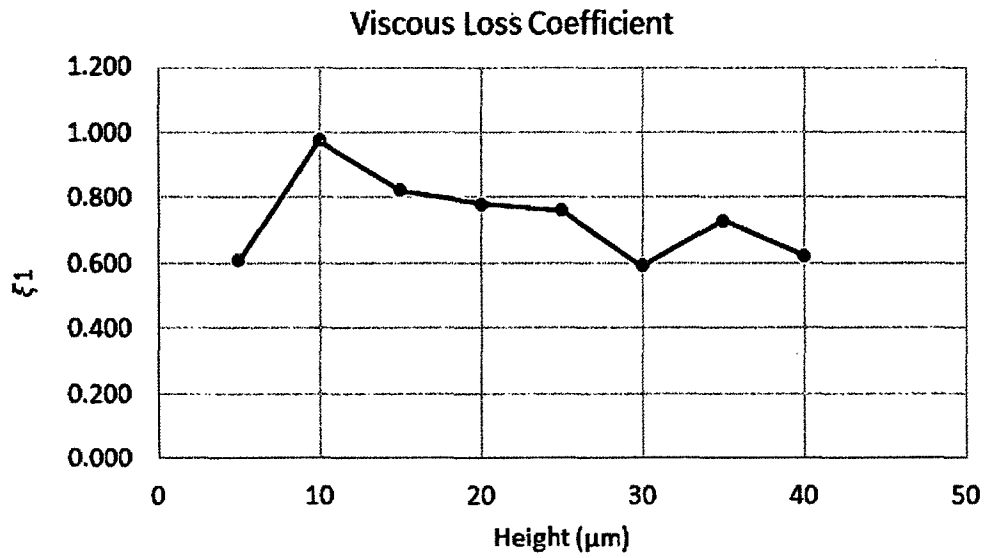


Figure 3-24: Viscous loss factors.

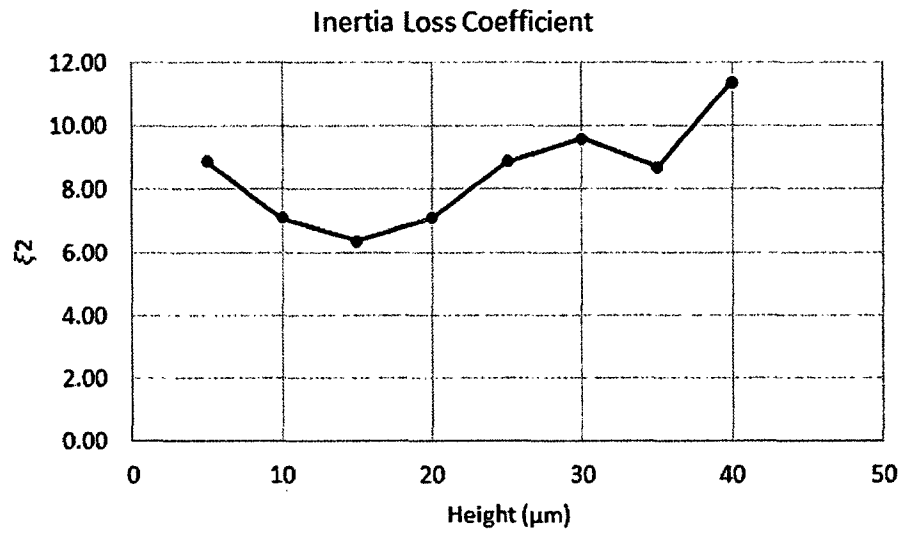


Figure 3-25: Inertia loss factors.

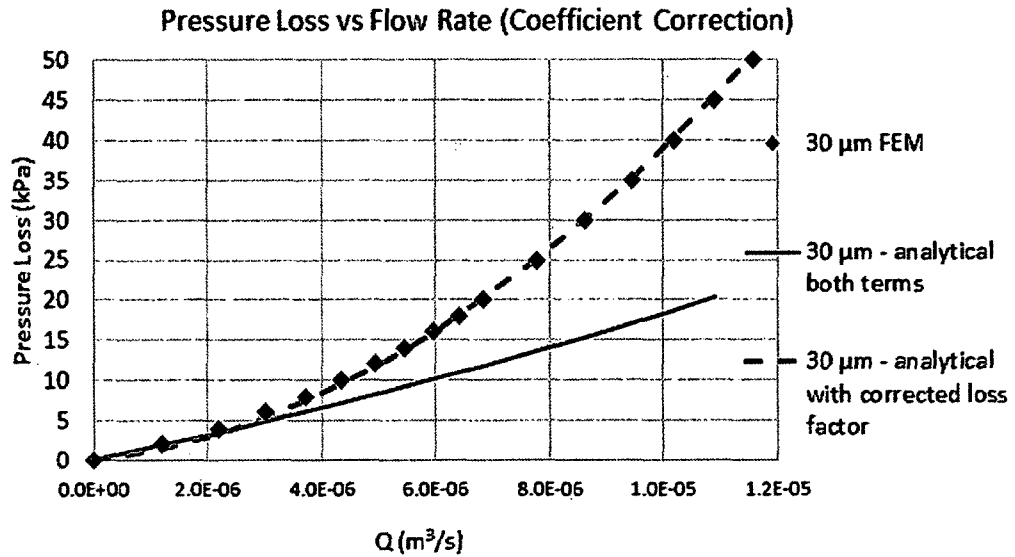


Figure 3-26: Pressure-flow relation with corrected loss factors for a 30 μ m gap height.

3.2.3.2 Flow through a Flexible Valve Plate

The second approach is illustrated in **Figure 3-27(a)**, where the valve rest perfectly on the seat surface with no initial gap as shown **Figure 3-27(a)**. The valve plate is modeled as a spring-mass system. With quasi-steady pressure-flow, the inlet pressure, p_{in} develops steady gas flow and deflects the valve to an equilibrium height, h_2 , as illustrated in **Figure 3-27(b)**.

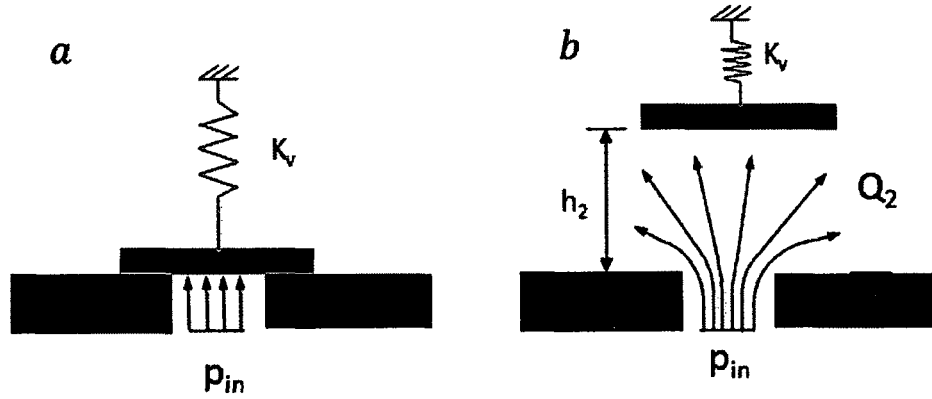


Figure 3-27: (a) Schematic of the microvalve plate in the close position. (b) Schematic of the steady gas flow of the microvalve deflecting the microvalve to an equilibrium gap height.

With the flow rate relating to the load, W in **Eq. 3-20** is set as the spring force of the valve, $k_v h_2$

$$k_v h_2 = 3\mu(r_2^2 - r_1^2) \frac{Q_1}{h_1^3}. \quad \text{Eq. 3-25}$$

Combining **Eq. 3-21** into **Eq. 3-25**, the flexible microvalve gap height at the equilibrium point in relation to the inlet pressure is

$$h_2 = \frac{p_{in} \pi (r_2^2 - r_1^2)}{\xi_1 k_v 2L \ln \left(\frac{r_2}{r_1} \right)}. \quad \text{Eq. 3-26}$$

The flow at the equilibrium position is given as

$$Q_2 = \frac{\pi h_2^3 p_{in}}{6\mu \ln \left(\frac{r_2}{r_1} \right)}. \quad \text{Eq. 3-27}$$

The flexible microvalve gap height from **Eq. 3-26** is plotted in **Figure 3-28**.

Subsequently, the calculated flow rate from **Eq. 3-27** is plotted in **Figure 3-29**.

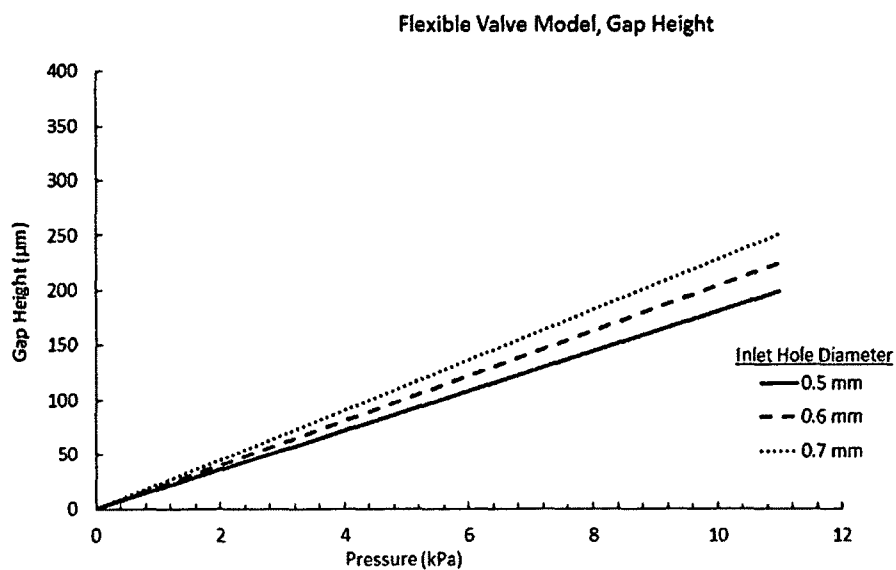


Figure 3-28: Valve plate gap height for flexible valve model, Q₂.

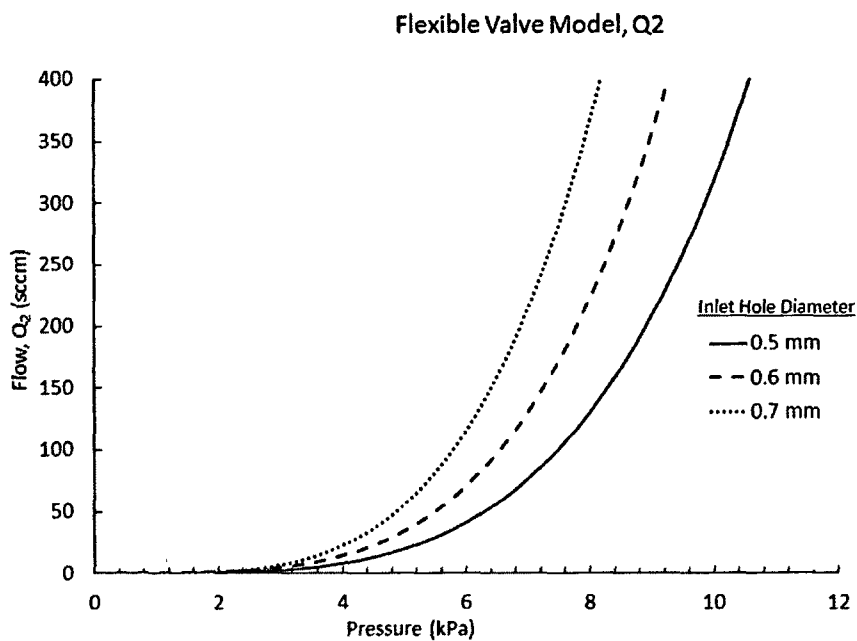


Figure 3-29: Pressure-Flow characteristic curve for flexible valve model, Q₂.

3.2.4 Pressure-Flow Microvalve Test Characterization

An experiment was designed to further characterize the pressure-flow of the microvalve and validate the quasi-steady flow model. Various inlet diameter sizes were used to obtain the pressure flow relation.

3.2.4.1 Experimental Setup

To obtain the pressure-flow relation, a microvalve test jig with an array of different inlet diameter was developed as shown in **Figure 3-30**. To test the flow of the microvalve and pressure relation, the microvalve pressure and flow was generated from a syringe pump as shown in the test set up in **Figure 3-31**. The flow rate through the microvalve was determined from the syringe pump rate set from the equipment. A pressure manometer was tapped to measure the generated back pressure. Forward flow was measured with the setup shown in **Figure 3-31(a)**. Reverse flow was measured by applying flow at the outlet of the microvalve with the setup shown in **Figure 3-31(b)**. A collection tube was used to measure the flow rate, since reverse leakage would be small and would require some back pressure to generate the reverse flow.

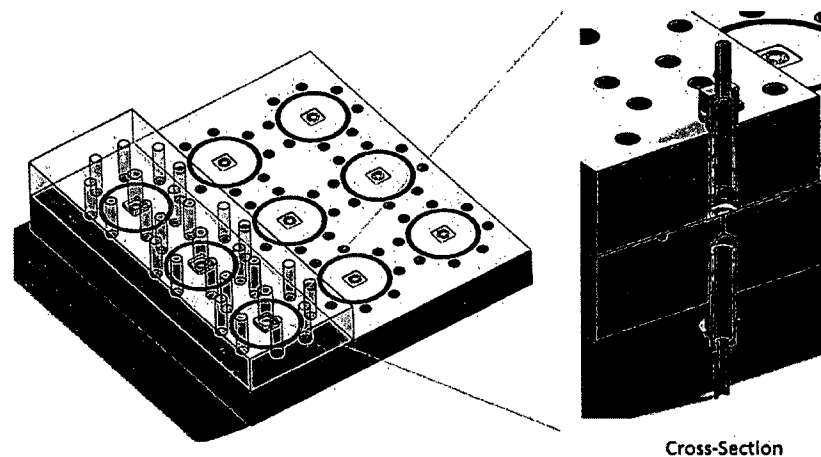


Figure 3-30: Microvalve test jig.

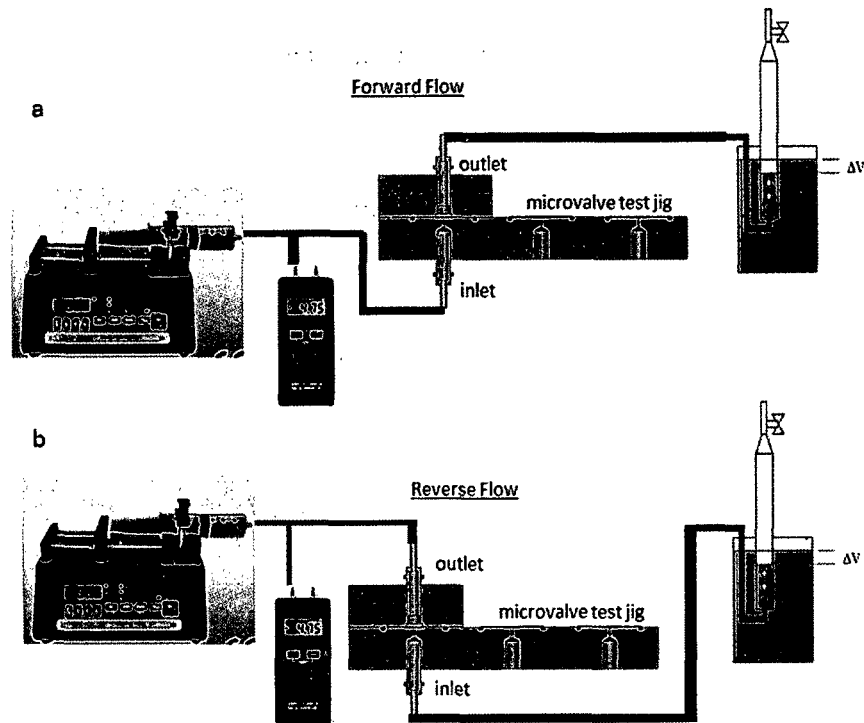


Figure 3-31: (a) Microvalve pressure-flow test set up for forward flow. (b) Microvalve pressure-flow test set up for reverse leakage flow.

The microvalves are attached to the valve seats using the same method as the microcompressor device with UV adhesive. As a result of manually attaching the microvalves, variations in adhesive thickness layer in between the microvalve and its seat resulted in different gap height. Subsequent to the pressure-flow measurement, the microvalves were removed from the valves seat with the UV adhesive still intact with the valve seat. The thickness of the adhesive was measured with a 3D optical profilometer (Zeta instrument) to obtain the average gap height.

3.2.4.2 Pressure-Flow Test Characterization

Figure 3-32 shows the forward pressure-flow curve and the reverse leakage for the microvalves with inlet hole diameters ranging from 0.5 – 0.8 mm and its corresponding gap height from the UV adhesive. It can be seen that for the forward flow

The relation is linear at the lower inlet pressure range. At this lower region, there is an initial gap height in the microvalve. The initial gap height of the valve plate remains constant as the pressure increases and the flow increases through the valve plate. As the pressure reaches a threshold, the valve plate begins to deflect and allows for increase flow rate of gas through the plate. Hence, it is observed that there is an exponential increase trend in the flow rate as a function of pressure once it passed the threshold.

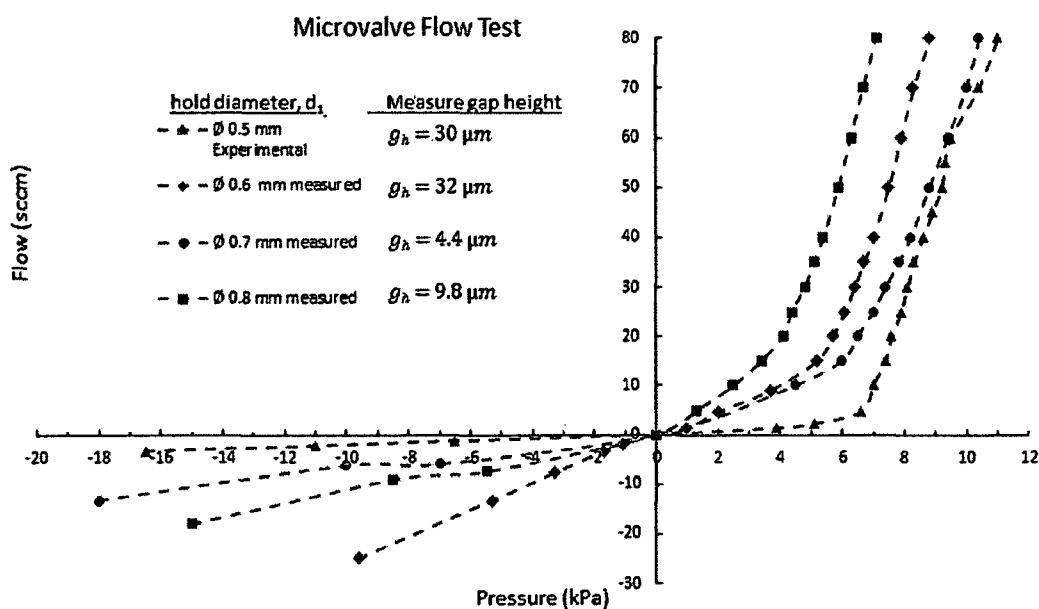


Figure 3-32: Microvalve pressure-flow test for forward and reverse flow.

The magnitude of the sealed-reverse leakage of the microvalve is shown to be linearly dependent on the magnitude of back pressure and is modeled as

$$\dot{M}_l = \beta \Delta P \quad \text{Eq. 3-28}$$

where the reverse flow coefficient, β , is the slope of the pressure-flow curve from **Figure 3-32**, given in the amount of reverse flow per unit of back pressure. From the reverse leak test result summarized in **Table 3-8**, the 0.5 mm hole has $\beta = 0.207$

$(\frac{sccm}{kPa})$, indicating the most reverse flow resistance to back pressure despite its large gap height. There is an increase in sealed surface area for 0.5 mm hole. The 0.6 mm hole provides the least reverse leak resistance to pressure, even less than the 0.7 and 0.8 mm hole. The smaller gap height of 4.4 μm and 9.8 μm in the 0.7 and 0.8 mm hole contributed to a better reverse leak resistance than the 0.6 mm hole where there is a larger gap height.

Table 3-8: Reverse flow coefficients of the experimental test from **Figure 3-32**.

d_1 (mm)	β ($\frac{sccm}{kPa}$)
Hole diameter	Back pressure leak rate coefficient
0.5	0.147
0.6	2.663
0.7	0.722
0.8	1.176

The quasi-steady model developed in the previous section is compared with the measured pressure-flow relation and to provide insight of the valve behavior. In **Figure 3-33** and **Figure 3-34**, the 0.5 and 0.6 mm measured pressure-flow relations are compared to the model from **Eq. 3-21** and **Eq. 3-27**. As shown in **Eq. 3-21**, the flow rate model, Q_1 , is modeled as a fixed plate. The flow rate model, Q_2 , is used to model the pressure-flow curve for a flexible valve plate.

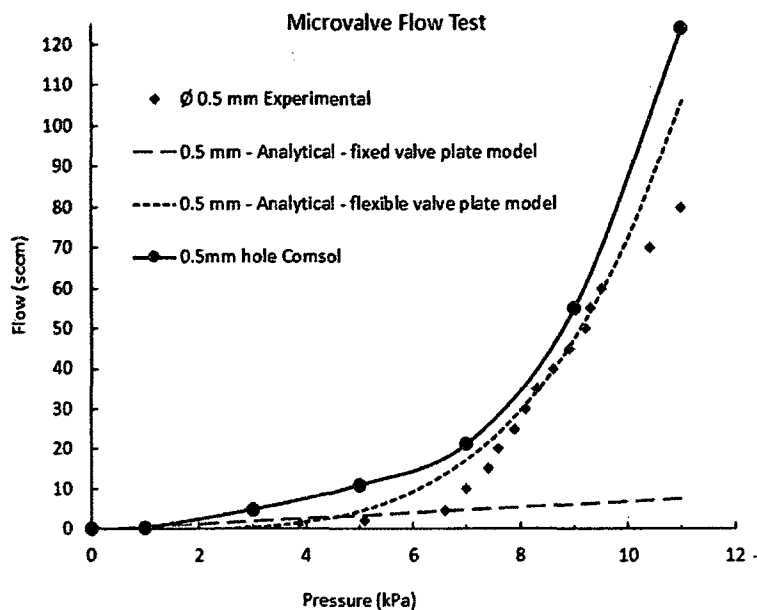


Figure 3-33: Comparison of experimental pressure-flow curve to model for a 0.5 mm inlet hole.

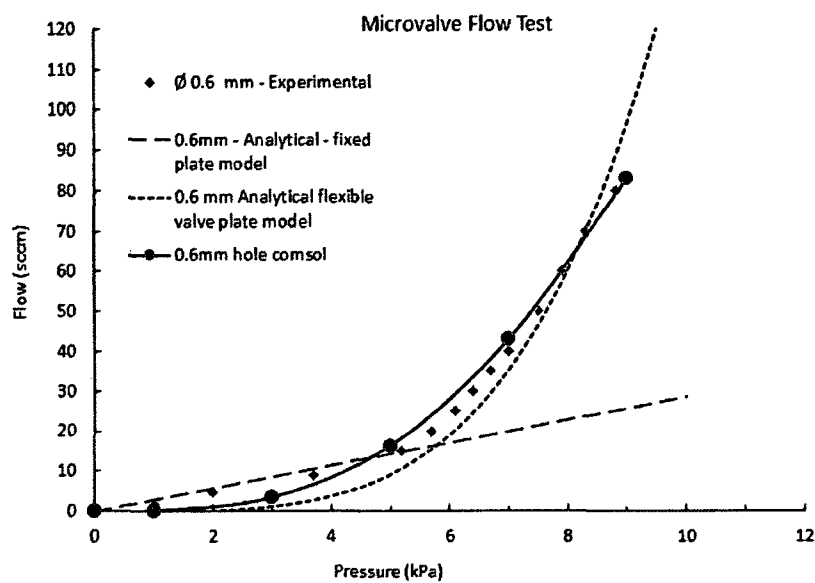


Figure 3-34: Comparison of experimental pressure-flow curve to model for a 0.5 mm inlet hole.

The model of the fixed valve plate and the flexible valve plate model required parameter adjustments as shown in **Table 3-9** to obtain a good fit where it can match the experimental pressure-flow curve. The gap height, h , from the experimental test was measured at 30 μm . However, the fixed plate model required a 7 μm gap height for it to fit the experimental curve. The flexible valve plate model showed a good fit to the experimental curve for the 0.5 mm hole. Furthermore, the tested 0.6 mm hole pressure-flow curve was fitted against the fixed-plate model and the flexible valve plate model. Similarly, a gap height of 15 μm was needed to show a good fit at the port of the pressure-flow curve. The flexible model provided a better fit at higher pressure.

Table 3-9: Summary of microvalve pressure-flow model and experimental parameters.

	Experimental	Fixed-Plate Model	Flexible Valve plate model
Ø0.5 mm inlet hole	-	$Q_1 = \frac{\pi h_1^3 p_{in}}{\xi_1 6\mu \ln\left(\frac{r_2}{r_1}\right)}$	$Q_2 = \frac{\pi h_2^3 p_{in}}{6\mu \ln\left(\frac{r_2}{r_1}\right)}$
	$h = 30 \mu\text{m}$	$h = 7 \mu\text{m}$	$h_2 = \frac{p_{in}\pi(r_2^2 - r_1^2)}{\xi_2 k_v 2L \ln\left(\frac{r_2}{r_1}\right)}$
	-	-	$k_v = 475 \text{ N/m}$
	-	$\xi_1 = 0.3$	$\xi_2 = 0.9$
Ø0.6 mm inlet hole	-	$Q_1 = \frac{\pi h_1^3 p_{in}}{\xi_1 6\mu \ln\left(\frac{r_2}{r_1}\right)}$	$Q_2 = \frac{\pi h_2^3 p_{in}}{\xi_2 6\mu \ln\left(\frac{r_2}{r_1}\right)}$
	$h = 32 \mu\text{m}$	$h = 15 \mu\text{m}$	$h_2 = \frac{p_{in}\pi(r_2^2 - r_1^2)}{\xi_2 k_v 2L \ln\left(\frac{r_2}{r_1}\right)}$
	-	-	$k_v = 475 \text{ N/m}$
	-	$\xi_1 = 0.6$	$\xi_2 = 0.85$

The FEM simulation of the pressure-flow characteristic follows the experimental trend of the flow characteristics. The error is likely due to the error in the material properties of the SU8 materials. Post exposure bake temperature of the SU8 changes the Young's modulus and Poisson ratio [109]. Other errors which were not accounted for includes the flow restriction at the experimental inlet and variations in the gap height from the adhesive.

Summary: A pressure-flow curve for a fixed valve plate is developed and the loss coefficients at different gap heights were determined using the result from the FEM analysis. The fixed plate model includes the viscous and inertia effect contributing to the pressure loss. It was determined that the inertia effect is an order of magnitude less than the viscous effect and has some low gap height of the valve plate.

3.2.5 Tethered Arm Model

The total stiffness constant of the valve is $F = k_t y$, where F is the force acting on the valve plate, k_t is the combined total spring constant of the three tethered arms and is given in **Eq. 3-29**, and y is the displacement of the valve plate. The design of the tethered arms shown in **Figure 3-35** is modeled as a beam with a fixed end and a guide-end. Each of the three arms are considered as a spring in parallel and is given in **Eq. 3-29**, where k_t is the total spring constant of the 3 arms, and k_a is the spring constant of each arm. Each arm has three individual beams connected in series. For beams connected in series, its spring constant is evaluated in parallel as given in **Eq. 3-30**.

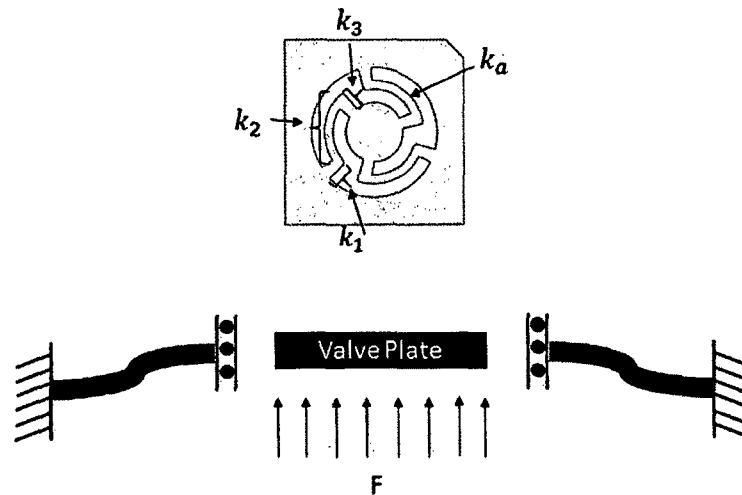


Figure 3-35: Schematic of valve spring model.

$$k_v = 3k_a \quad \text{Eq. 3-29}$$

$$\frac{1}{k_a} = \frac{1}{k_1} + \frac{1}{k_2} + \frac{1}{k_3} \quad \text{Eq. 3-30}$$

The inertial of the beam is given as

$$I = \frac{wh^3}{12} \quad \text{Eq. 3-31}$$

where w and h is the width and height of the beam. The spring constant for a fixed-guide beam is given as

$$k = \frac{12EI}{L^3}. \quad \text{Eq. 3-32}$$

3.2.6 Transient Couple Fluid Structure FEM Analysis of Microvalve

The transient dynamic behavior of the microvalves with the interaction of the gas flow is difficult to determine experimentally because of the small scale of the structure and the high frequency behavior of the microvalves. Ulrich [110] and Koch [111] have studied the static and dynamic flow simulation of a cantilever microvalve using FEM coupled with CFD simulations. Transient simulation can be time consuming and computationally

intensive. However, it can give information on the damping property of the microvalve structure and the effective mass of the microvalve. A microvalve structure can be represented as a 2nd order differential equation:

$$m\ddot{z} + c\dot{z} + kz = F \quad \text{Eq. 3-33}$$

3D transient FSI FEM was set up in Ansys using a 2-way fully coupled transient structural and fluent flow (Fluent) with the boundary conditions shown in **Figure 3-36**. The inlet port was set at 7 kPa and the outlet port was set to 0 kPa. The end of the tether valve is fixed. The microvalve plate has an initial gap height of 10 μm to allow for mesh to exist between the valve plate and the valve seat. Microvalves fabricated from literatures [39], [60], [110], [112] have been shown to have an initial gap height after the release of the microvalve from the substrate.

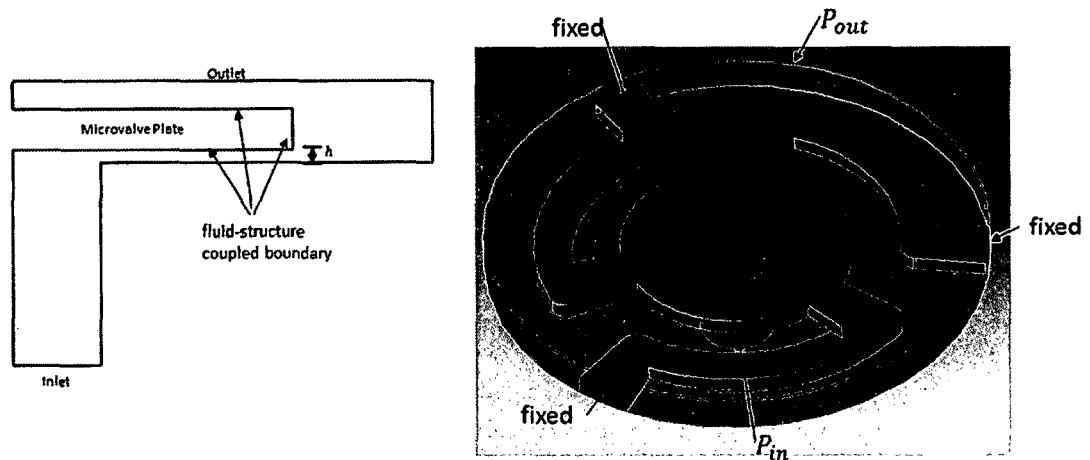


Figure 3-36: FSI FEM boundary conditions setup.

Air was used as the fluid medium in the simulation. **Figure 3-37** shows the fluid domain with tetrahedral mesh, the structural domain with quadrilateral mesh, and the deformation of the microvalve structure. The deflection response of the microvalve from the flow generated by the inlet pressure is given in **Figure 3-38**.

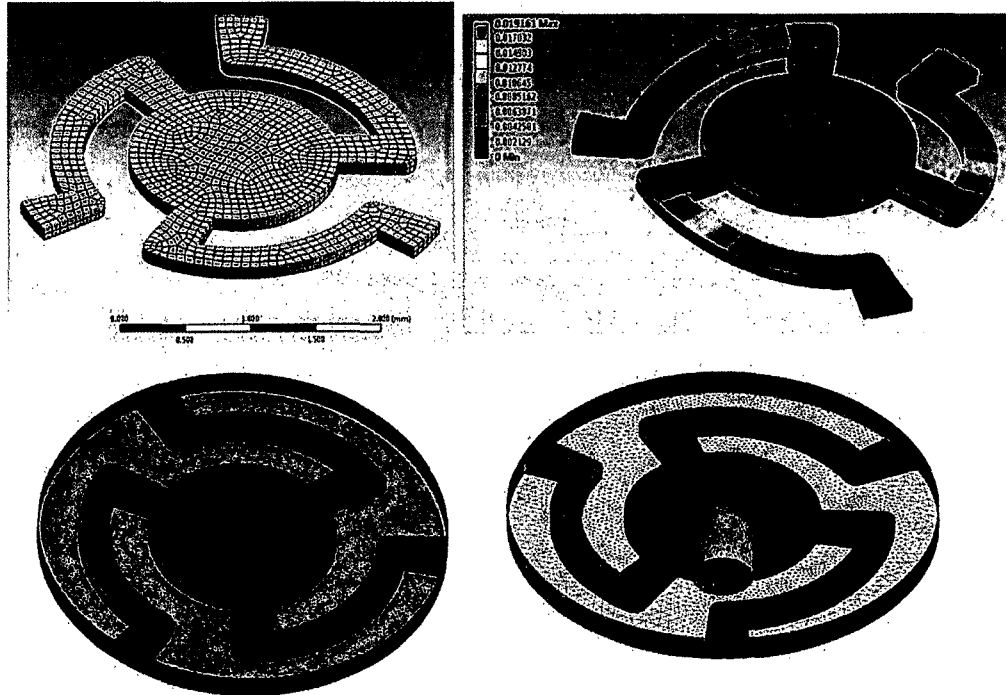


Figure 3-37: (Top left) quadrilateral mesh for the microvalve. (Top right) Deflection of the microvalve with fluid force. (Bottom left) tetrahedral mesh for fluid with the top boundary hidden. (Bottom right) tetrahedral mesh for fluid with the bottom boundary hidden.

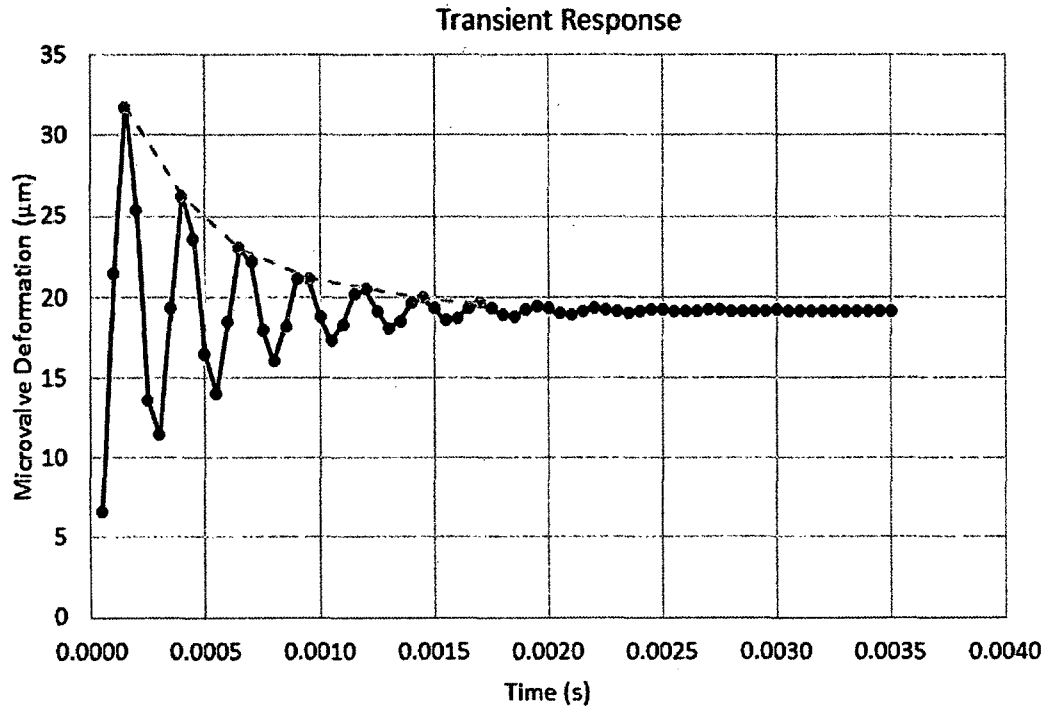


Figure 3-38: Microvalve plate structural displacement response to transient FSI simulation.

The damping ratio, ζ is given as

$$\delta = \frac{1}{n} \ln \left| \frac{x_1}{x_{n+1}} \right| \quad \text{Eq. 3-34}$$

$$\zeta = \frac{\delta}{\sqrt{4\pi^2 + \delta^2}} \quad \text{Eq. 3-35}$$

where x_1 is the first deflection peak, and x_{n+1} is the n^{th} peak. The effective mass, m_{eff} is given as

$$\omega_r = 2\pi f = \sqrt{\frac{k}{m_{eff}}} \quad \text{Eq. 3-36}$$

where ω_r is the resonant frequency (radian/sec) of the structure.

The frequency f is determined from the oscillation peaks of the valve's response and is given as

$$f = \left| \frac{1}{t_{x1} - t_{x2}} \right| \quad \text{Eq. 3-37}$$

where t_{x1} and t_{x2} are the times of the first and second oscillation peaks. The parameters of the microvalve lumped model is summarized in **Table 3-10**. The first mode resonant frequency of the microvalve is at 5.76 kHz and decreases to 4.0 kHz under load, with the effective mass remaining the same.

Table 3-10: Differential equation parameters of microvalve structure determined from static and transient analysis.

	Static	Transient (FEM)
Resonant Frequency	5.76 kHz	4.0 kHz
Mass	749 ng	749 ng
Damping Ratio, ζ	-	0.0950
Spring stiffness, k	473 N/m	-

The pressure distribution on the lower surface of the microvalve is shown in **Figure 3-39**. At this pressure and height, the inlet pressure is mainly concentrated at the center of the valve plate.

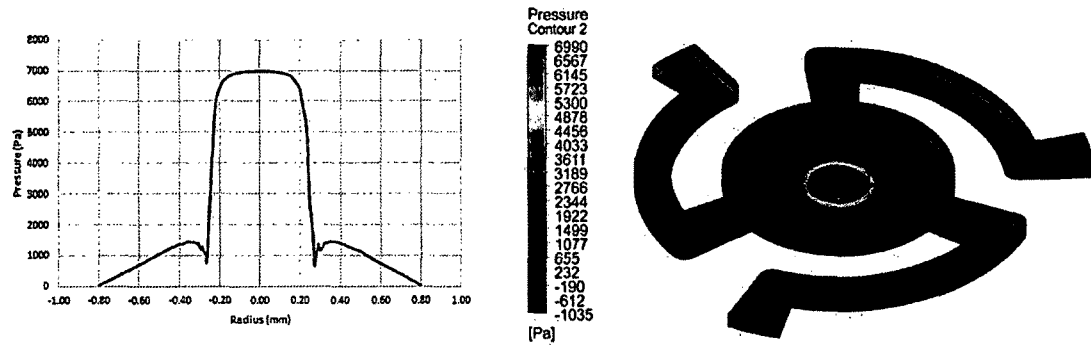


Figure 3-39: Pressure distribution of microvalve at steady state.

3.3 Summary

This chapter discussed the analysis of the two critical components in the microcompressor's design, the piezoelectric unimorph diaphragm, and the microvalve and its pressure-flow interaction. Piezoelectric diaphragms are widely used as a micropump actuator and is easily available to fabricate in the microscale with proven microfabrication processes such as the sol-gel and screen printing method discussed in this chapter. The static deflection with respect to the input voltage of the piezoelectric unimorph diaphragm was predicted with the CLPT method and FEA. Due to the nonlinearity of the diaphragm at high resonant frequency, the prediction of the piezoelectric diaphragm deflection requires a frequency response test and FEA analysis and correlation to the deflection shape to obtain the stroke volume generated from the diaphragm. There are limitations of the piezoelectric unimorph diaphragm from the amount of stroke it can generate under pressure load.

The microvalve pressure-flow model was presented and compared with the fluid-structure interaction FEA analysis to determine its flow coefficients. Both the fixed-plate and flexible plate models were presented to characterize the measured pressure-flow

relations (**Figure 3-32 - Figure 3-34**) and were used to explain the test results in **Figure 3-32**. According to the microvalve analytical models and test results, larger inlet microvalve inlet radiuses reduce the fluidic impedance of the microvalve. However, it also reduces the sealing surface area of the valve plate and its seat. Thus, it reduces the sealed-reverse leakage of the microvalve at large back pressure which can be detrimental to the generation of large pressure rise. In the second part of the analysis, transient fluid-structure interaction FEA were implemented to determine the damping ratio and used for the lumped model simulation studies of the microvalve in Chapter 4.

CHAPTER 4

SINGLE AND MULTISTAGE MICROCOMPRESSOR MODELING AND SIMULATION

This chapter presents the simulation and analysis to predict the performance of a single and multistage microcompressor. The simulation tool developed in this chapter is used to study the behavior between the dynamics in each microcompressor chamber, and the valves dynamics between each chamber. The objectives of this study are to:

- Use a lumped model simulation to study the feasibility and the effectiveness of utilizing passive micro check valves to control the transfer of gas between each stage and how it can affect the overall pressure ratio and performance of a multistage microcompressor.
- Study different configurations of the multistage microcompressor. In configuration one, simulate the multistage microcompressor without dead volume in the chamber, and utilizing one microvalve between cascading chambers. In configuration two, simulate the multistage microcompressor with an interconnection chamber in between each stage, and having two microvalves to control the transfer of gas between stages.
- Validate the lumped model simulation to the experimental device.

Figure 4-1 shows the flow chart for the development of a simulation model for the single-stage and two-stage microcompressor designs. The microcompressor is first

designed with a CAD model to obtain realistic pump chamber volume. The microvalve simulation model is developed with Simulink prior to developing the compressor model. FEA is used to obtain pressure-flow relations for the microvalve model and verified with the lumped model result in Simulink. Parameters and characteristics from the unimorph diaphragm are extracted from experimental data and FEA for the single-stage microcompressor model. Once the lumped parameters for the single-stage are extracted and developed in Simulink, it is expanded into a two-stage model with Simulink. The fabricated single and two-stage devices are tested and compared with lumped model simulation results.

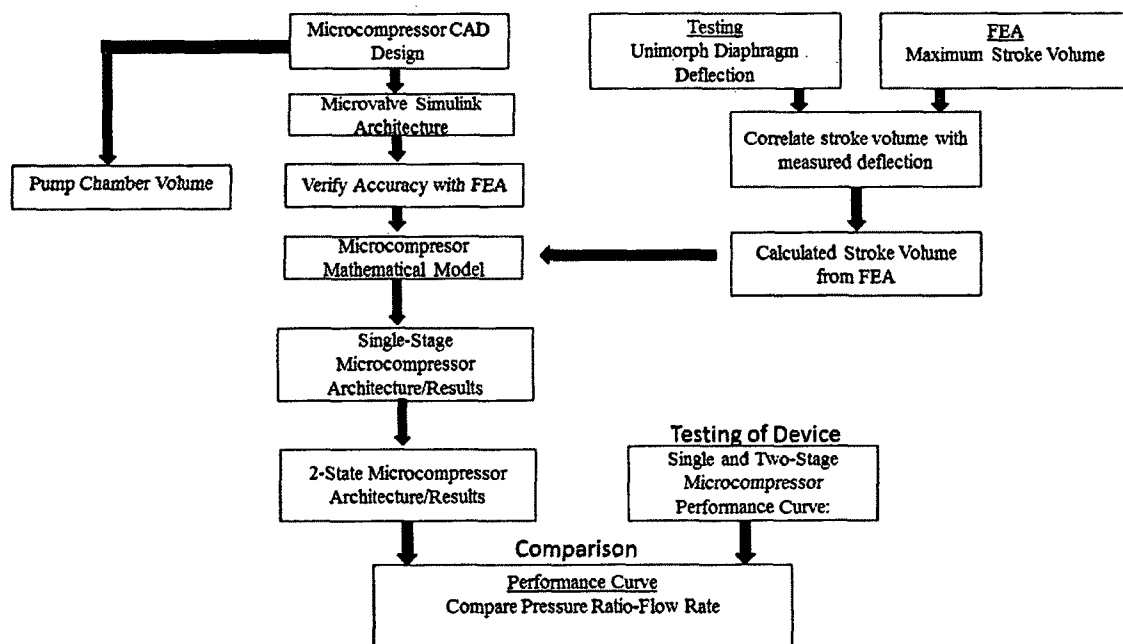


Figure 4-1: Flow chart for the design of microcompressor architecture and simulation results.

Previous methods to simulate a single-stage microcompressor used the Warner and fourth order Runge-Kutta method to obtain the numerical solutions [37], [113].

Lumped model parameters equation derived from compressor thermodynamics was used to build a simulation in Matlab Simulink.

4.1 Principle of Operation

A schematic of the single-stage microcompressor is shown in **Figure 4-2(a)**, which consists of a piezoelectric diaphragm and two passive micro check valves, each for the inlet and outlet ports. The piezoelectric diaphragm is in a unimorph configuration and actuated with bipolar sine voltage up to deform the membrane for mechanical gas suction and compression in the chamber. In the suction phase, the membrane bends upward to expand the volume of the chamber and creates a negative pressure difference, causing the inlet microvalve to open and allow gas to flow into the inlet port, and the outlet microvalve to close to preventing gas backflow. In the compression phase, the membrane bends downward to compress the gas, creating positive pressure difference in the chamber for the inlet valve to close and outlet valve to open. With input voltage sine wave to the piezoelectric, the cycle repeats to generate gas flow and pressure rise from the compressor.

The multistage microcompressor (two-stage) schematic shown in **Figure 4-2(b)** is designed with configuration similar to the single-stage design. For the two-stage design, the chambers are connected in series to increase pressure rise. Two interconnected microvalves exist between the connecting chambers to control the gas transfer between each stage. The microvalve opens and closes as the pressure difference between chamber 1 and chamber 2 varies. Two passive micro check valves are used for each chamber. The first stage is placed at the top and the 2nd stage is placed at the bottom to minimize the overall size of the device.

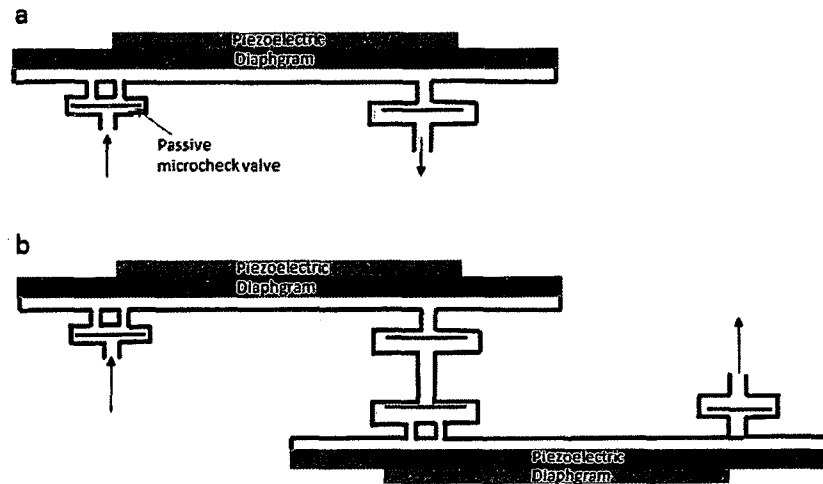


Figure 4-2: (a) single-stage microcompressor schematic. (b) multistage, two-stage, microcompressor schematic.

4.1.1 Theoretical Pump Performance

The microcompressor is designed to achieve high pressure rise and flow rate, low power consumption and small footprint to fit the need of a micro cryogenic cooler (MCC). The pressure ratio is given as

$$\frac{P_o}{P_{in}} = \left(\frac{V_{max}}{V_{min}} \right)^n \quad \text{Eq. 4-1}$$

where the maximum pump chamber volume, V_{max} is when the actuator or diaphragm is at its maximum suction stroke. The chamber volume is at its minimum, V_{min} , when the actuator is at its compression stroke. The compression stroke of the actuator does not fill the whole chamber, and the dead volume, V_{min} , is left. Dead volume from the inlet and outlet ports of the chamber are also considered dead volume. Leakage from the microvalve is also considered as dead volume. Microscale size actuators are limited by the force they can generate against the head pressure of the microcompressor. The dead

volume becomes larger as the actuator reaches its limitation to compress against the head pressure of the gas in the chamber.

The compressor flow rate is given as

$$Q = \Delta V_{stroke} f \varepsilon_f \quad \text{Eq. 4-2}$$

where f is the operation frequency. ε_f is the static rectification efficiency [14] of the compressor and where it is the net flow into the chamber for a suction cycle divided by the total flow out of the chamber for a compression cycle. ε_f is given as

$$\varepsilon_f = \frac{\text{net flow in}}{\text{net flow out}} = \frac{\phi_{1+} - \phi_{2-}}{\phi_{2+} - \phi_{1-}} \quad \text{Eq. 4-3}$$

where ϕ_1 and ϕ_2 denote the flow at the inlet and outlet valve, respectively. The + and – denote flow forward and reverse flow direction, respectively. During the suction cycle, ϕ_{1+} is the flow into the chamber at the inlet microvalve, and ϕ_{2-} is the reverse flow at the outlet microvalve as a result of reverse leakage and sealed-reverse leakage. For the compression cycle, ϕ_{2+} is the forward flow at the outlet microvalve, and ϕ_{1-} is the reverse flow at the inlet microvalve due to the reverse leakage and sealed-reverse.

Vapor compression system requires high pressure ratio as well as a volumetric flow rate. Sathe [43] suggested a flow rate of 1,141 sccm for an 80 W laptop cooler using R134a. For Lewis [72], a flow rate of 270 sccm was needed at maximum efficiency and 50 sccm to stabilize the temperature in their JT MCC. For a multistage compressor, the pressure ratio is given as

$$\frac{(P_o)_j}{(P_{in})_j} = \left(\frac{V_{max_j}}{V_{min_j}} \right)^n \quad \text{Eq. 4-4}$$

where j is the stage number. The overall pressure ratio of the multistage compressor for M number of stages is given as

$$\frac{(P_o)_M}{(P_{in})} = \prod_{j=1}^M \left(\frac{V_{max_j}}{V_{min_j}} \right)^n \quad \text{Eq. 4-5}$$

The j^{th} stage inlet pressure is equal to outlet pressure of the previous stage, $(P_{in})_j = (P_o)_{j-1}$, for $j = 1, 2, 3, \dots, M$, where M is the total number of stages. For a two-stage microcompressor, the pressure ratio of the 1st stage is multiplied with the pressure ratio of the 2nd stage to obtain the total pressure ratio of multistage as given in **Eq. 4-5**.

The volume ratio is given as

$$\varepsilon = \frac{V_s}{V_c} = \frac{V_s}{V_s + V_d} \quad \text{Eq. 4-6}$$

where V_s and V_d are the stroke volume and dead volume of the chamber, respectively.

The theoretical pressure ratios for a single-stage from the designed microcompressors is determined by using **Eq. 4-5**. Thus, values for V_s and V_d are needed to determine the pressure ratio. First, V_s is determined from **Figure 3-12** at 13 μm center deflection, where the center deflection of the piezoelectric diaphragm at 13 μm , the calculated volume is $1.5 \times 10^{-9} \text{ m}^3$. Since the diaphragm deflection is symmetric in the up and down positions, the total stroke volume is twice the calculated volume, where $V_s = 3.0 \times 10^{-9} \text{ m}^3$. Then the dead volume is calculated which comes from two sources in the chamber:

- 1) from the uncompressed volume of the chamber when the diaphragm is at its maximum stroke down position,
- 2) from the volume of the inlet and outlet holes connected to the microvalves.

The calculated dead volume from the design is $V_d = 1.0 \times 10^{-8} \text{ m}^3$. The calculated V_s and V_d gives the volume ratio and the theoretical pressure ratio in **Table 4-1. Figure 4-3**

shows the expected increase of pressure ratio for n number of stages if each stage has the same volume ratio.

Table 4-1. Theoretical pressure ratio of a single and multistage.

# of Stages	Volume Ratio, ϵ	Theoretical Pressure Ratio
1	0.23	1.44
2	0.23	2.09

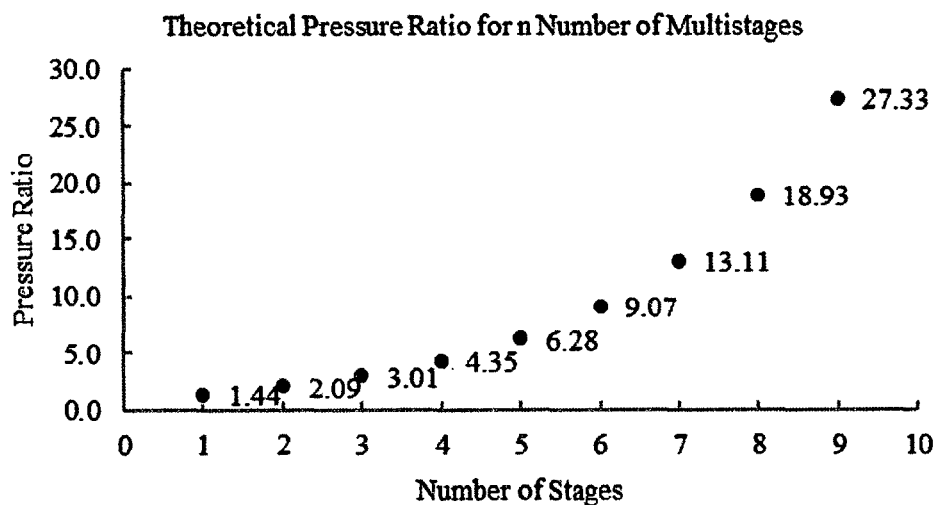


Figure 4-3: Theoretical pressure ratio for a given number of stages given by the volume ratio.

4.1.2 Compressor Model

The model of the multistage microcompressor follows the conservation of mass and the ideal gas law [113] as illustrated in **Figure 4-4**.

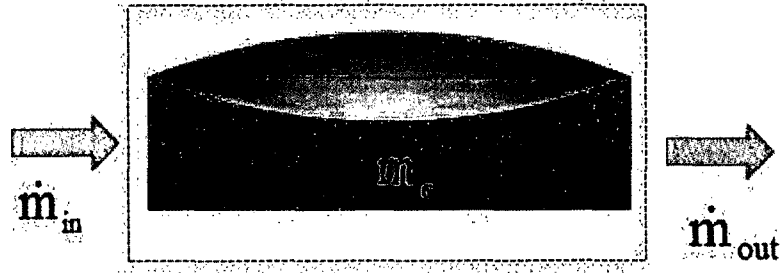


Figure 4-4: Compressor chamber control volume

For a control volume, the change in mass of the chamber is given as

$$\frac{dm_c}{dt} = \dot{m}_{in} - \dot{m}_{out}. \quad \text{Eq. 4-7}$$

The mass in the chamber and the density in the chamber are given as

$$m_c = \rho_c V_c \quad \text{Eq. 4-8}$$

$$\rho_c = \rho_{co} \left(\frac{P_c}{P_{co}} \right)^{1/n} \quad \text{Eq. 4-9}$$

The differential equation for the pressure in the chamber, P_c , varying with time relating to the volume chamber, mass flow rate in and out of the chamber is derived from the conservation of mass and momentum [113] is given as

$$\frac{dP_c}{dt} = \frac{-nP_c}{V_c} \frac{dV_c}{dt} + \frac{nP_c}{\rho_c V_c} (\dot{m}_{in} - \dot{m}_{out}). \quad \text{Eq. 4-10}$$

To reduce complexity of the nonlinearity in the unimorph membrane actuation, the volume displacement is simplified to

$$V_c = V_c + \frac{V_s}{2} (1 - \cos(\omega t)) \quad \text{Eq. 4-11}$$

where the volume stroke is constant. The magnitude of deflection for a unimorph membrane is linearly dependent on the drive voltage at a low frequency range. At the resonant frequency, the unimorph membrane exhibits its largest deflection magnitude.

The nonlinearity near the resonant frequency has not been modeled in literature and may require extrapolation from experimental data for the simulation model. Equation 4-11 is used to ignore these linear and nonlinear effects that the membrane actuator has on the stroke volume to simplify the complexity of the microcompressor model. Equation 4-12 – Equation 4-15 is the mass flow rate through the inlet and outlet microvalves.

Derived from the Bernoulli equations, the mass flow rate through the microvalve orifice is given in Eq. 4-12 to Eq. 4-15.

$$\dot{m}_{in} = C_f A_{in} \sqrt{2\rho_{in}(P_{in} - P_c)} \quad P_{in} < P_c \quad \text{Eq. 4-12}$$

$$-\dot{m}_{in} = C_f A_{in} \sqrt{2\rho_c(P_c - P_{in})} \quad P_c > P_{in} \quad \text{Eq. 4-13}$$

$$\dot{m}_o = C_f A_o \sqrt{2\rho_c(P_c - P_{in})} \quad P_c > P_{in} \quad \text{Eq. 4-14}$$

$$-\dot{m}_o = C_f A_o \sqrt{2\rho_{in}(P_{in} - P_c)} \quad P_{in} < P_c \quad \text{Eq. 4-15}$$

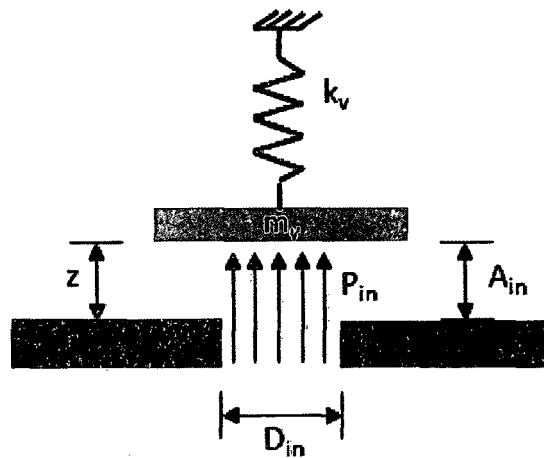


Figure 4-5: Schematic of the microvalve structure.

As the microvalve opens, the mass flow cross-sectional area is a function of the valve plate height, z , and is given in Eq. 4-16 and Eq. 4-17 for the inlet and outlet,

respectively. The orifice cross-sectional area, A_{in} and A_o is modeled as the cylindrical surface that the gas flows through the valve opening as a function of height:

$$A_{in} = \pi D_{in} z \quad \text{Eq. 4-16}$$

$$A_o = \pi D_o z \quad \text{Eq. 4-17}$$

$$m_v \ddot{z} + c \dot{z} + k_v z = C_d A_v (P_c - P_{in}) \quad \text{Eq. 4-18}$$

$$m_v \ddot{z} + c \dot{z} + k_v z = C_d A_v (P_{in} - P_c) \quad \text{Eq. 4-19}$$

$$\frac{dz[t_+]}{dt} = -r \frac{dz[t_-]}{dt} \quad \text{Eq. 4-20}$$

Eq. 4-18 and Eq. 4-19 describe the outlet and inlet microvalve dynamics, respectively. Equation 4-20 describes the restitution of the microvalve dynamics, when the microvalve impacts the valve seat right before collision at t_- and bounces back with a negative velocity right after collision with the valve seat at time t_+ . For $r = 1$, the impact is considered fully elastic, and for $r = 0$, the impact is fully inelastic. The coefficients cannot be predicted from the elastic material properties alone, due to the other fluid-structure interactions [114] such as stiction and air damping between the valve plate and the seat. Habing [114] and Maclaren [115] gave r coefficients ranging from 0.2 to 0.4 based on different valve models and published values that they found. Based on their study, a value of 0.2 was assigned to the valve dynamic model simulation.

4.1.3 Microvalve Model and Analysis

This section discusses the modeling and simulation of the microvalve dynamics combined with the fluid flow interactions of the gas flow through the valve structure. In order to compile the architecture of the multistage microcompressor, the microvalve architecture was designed separately from the microcompressor architecture. The approach in designing the microvalve lumped model simulation is illustrated in **Figure**

4-6. The design of the microvalve CAD model and FEA analysis were utilized to extract the parameters of the design for the lumped model simulation in Simulink. The CAD provided the mass of the microvalve for Eq. 4-19 and Eq. 4-20. Due to the irregular shape of the tethered arm in microvalve design, quasi-static analysis with FEA was implemented to determine its stiffness, k_v . To implement a realistic simulation of the microvalve structural behaviors with the interaction of the gas flow prior to fabrication and testing, fluid-structure interaction (FSI) analysis with finite element analysis was used to verify and correct the lumped model simulation result. This ensured that the microvalve simulation results were accurate prior to the integration of the microcompressor architecture.

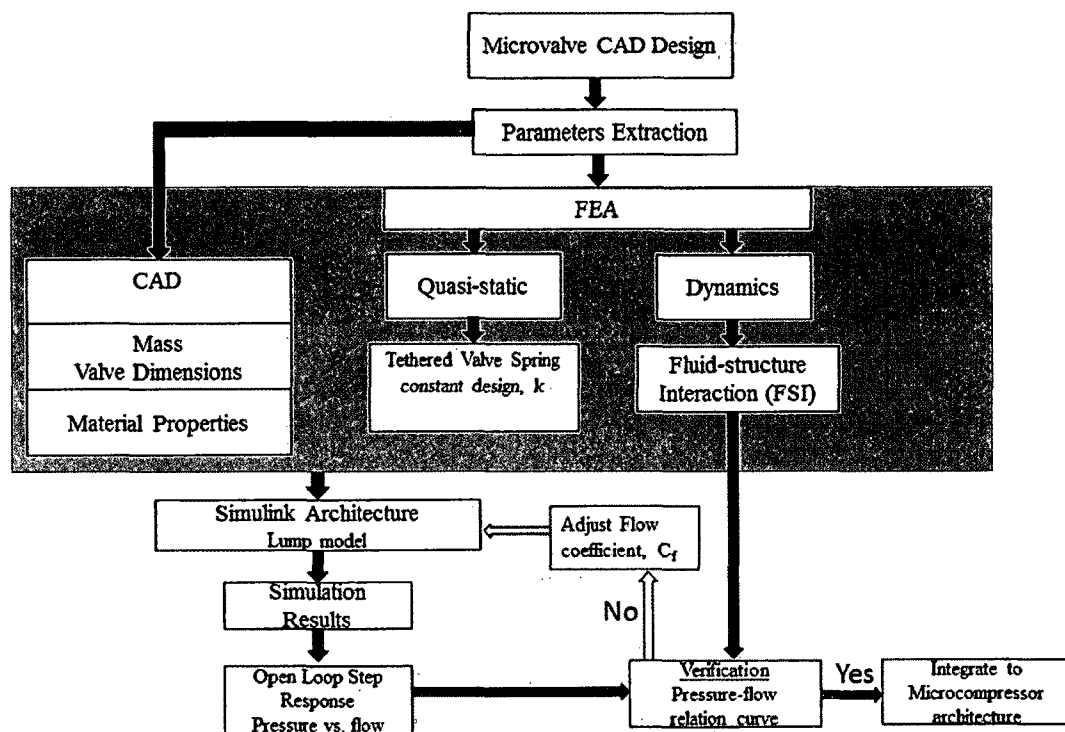


Figure 4-6: Flow chart of the microvalve Simulink simulation design.

The CAD model provided the mass for the lumped model of the microvalve dynamics given in **Eq. 4-19** and **Eq. 4-20**. To extract the spring's stiffness (k) of the microvalve, a quasi-static FEA in COMSOL was conducted. Varying static force loads were applied to the surface of the valve to determine plate displacement. **Figure 4-7** shows the displacement result from the FEA result with respect to the force load on the valve's body surface. From the slope of the linear relations in **Figure 4-8**, k is found to be 473 N/m. This is comparable, and in the same order of magnitude with a silicon dioxide, three arm tether microvalve developed by Hu *et al.* [60] has a stiffness of 851 N/m.

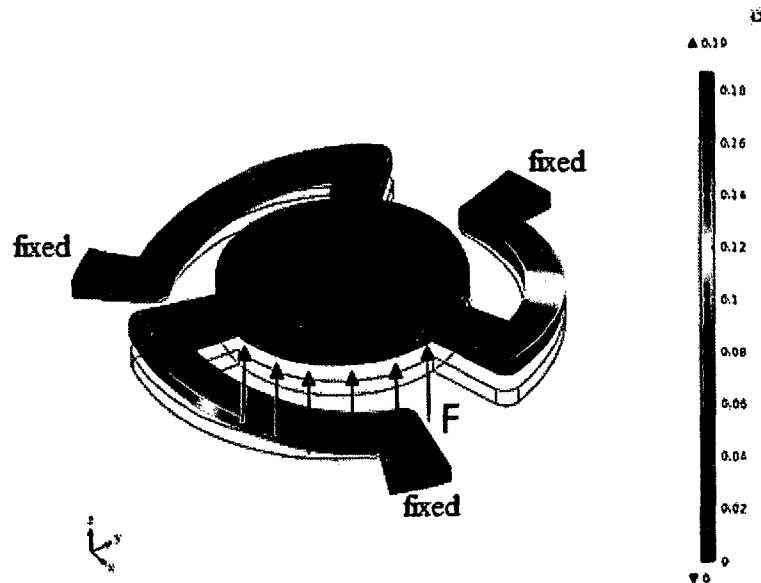


Figure 4-7: FEA result of the microvalve spring force constant.

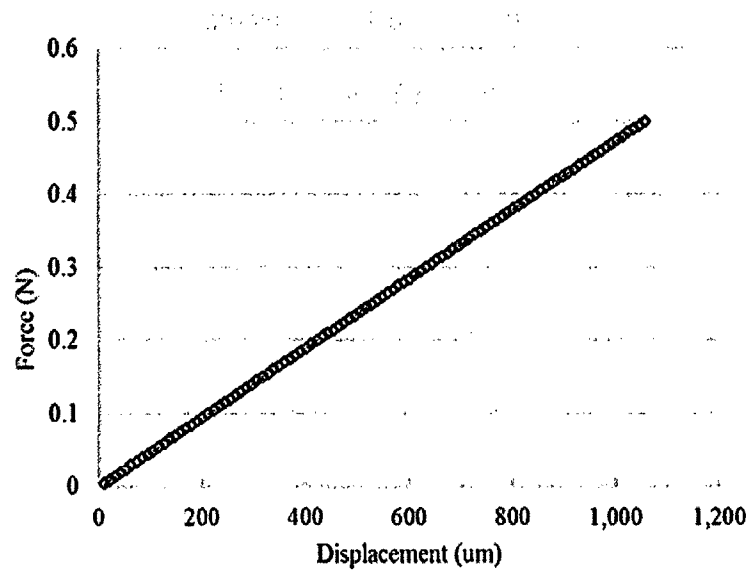


Figure 4-8: Microvalve force versus displacement.

4.1.4 Microvalve Simulink Architecture

The microvalve architecture is developed with equations **Eq. 4-12** to **Eq. 4-20**.

Since the dynamics for the outlet valve is similar to the inlet, the same modeling analysis is used. The assumptions made are: 1) that the stiction force is neglected, 2) the valve seat has an initial gap height, 3) force of the gas flow given by [116] is ignored, 4) the damping coefficient of the valve dynamic system determined from **Table 3-10** the FEA FSI analysis is used for the valve model, and 5) the restitution coefficient is given a low number of 0.2. The Simulink architecture for the inlet valve is designed to couple **Eq. 4-12**, **Eq. 4-13**, **Eq. 4-16**, **Eq. 4-18**, and **Eq. 4-20**. The coupling of these equations in Simulink is shown in **Figure 4-9**.

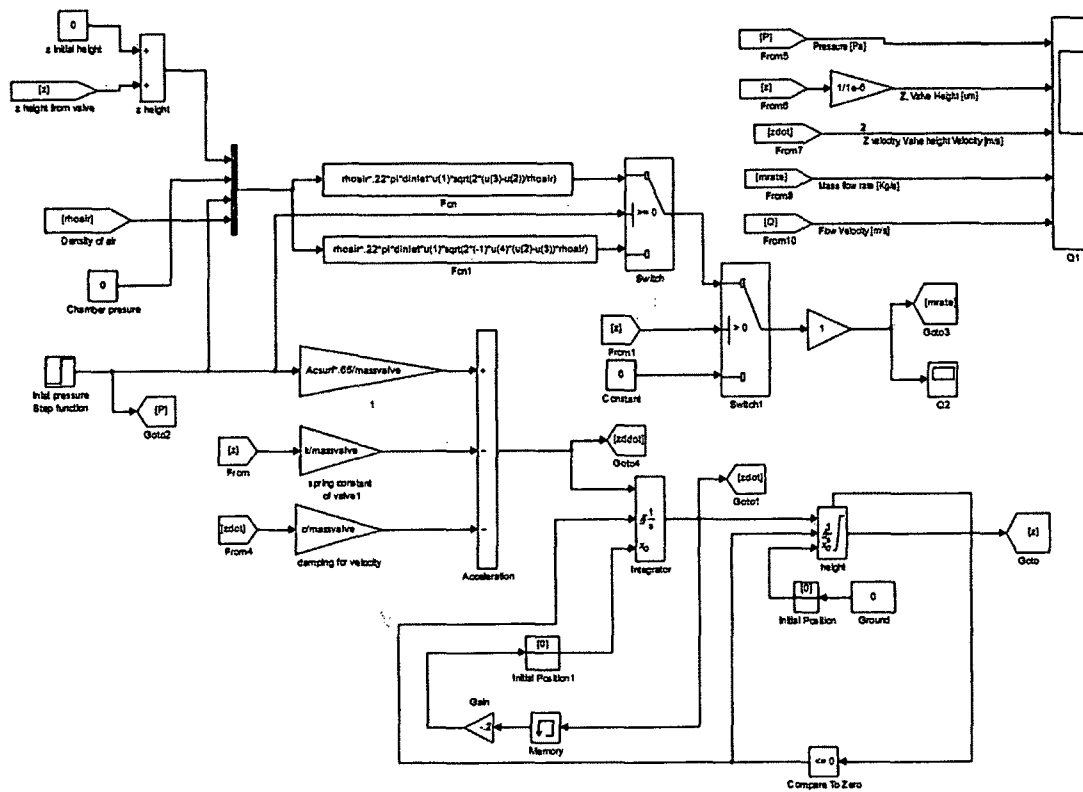


Figure 4-9: Microvalve architecture of fluid-structure dynamics with step pressure input.

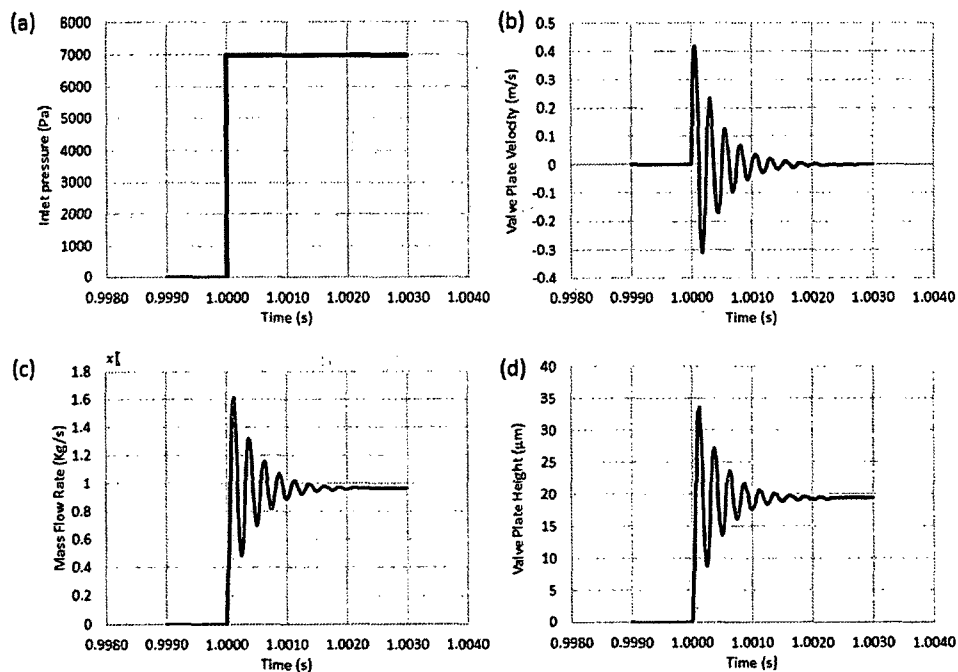


Figure 4-10: Step response of the microvalve Simulink simulation. (a) step input of the pressure at 7 kPa. (b) velocity response of the valve plate. (c) the response of the valve plate mass flow rate. (d) the response of the valve plate height.

A step input function in **Figure 4-10(a)** is used to set the input pressure at a steady set point. The result from the simulation shows the valve plate response velocity (b), valve height (c), and mass flow rate through the valve (d). At 7 kPa at the inlet, the microvalve plate opens to 20 μm height at a mass flow rate of 1 $\mu\text{kg/s}$. The lumped model simulation results are compared to the FEA simulation results in the next section.

4.1.5 Steady-State Fluid Structure Interaction (FSI) Analysis

In the first approach, discussed in Section 3.2.6, the transient analysis of the valve fluid-structure was conducted to obtain the dynamic response and extract the 2nd order dynamic system lumped parameters, such as the resonant frequency and damping ratio which are then utilized for this Simulink valve model. Further analysis of the valve FSI is needed to validate the pressure-flow relations of this design. Such analysis with a transient FEA FSI analysis requires a large amount of computer resources and computation time. Thus, a second analysis using quasi-steady FSI FEA analysis is simulated to extract the pressure-flow relation, avoiding the long computation times and large computer resources required from a transient dynamic steady gas flow.

The steady-state FSI simulation consists of a 3D tether valve structure bounded by the valve orifice and valve seat as illustrated in **Figure 4-11**. The three tether arms connected to the valve have a non-axisymmetric design, so a full 3D model FSI simulation was used. The analysis was conducted with inlet pressure assigned at the inlet and zero pressure is assigned to the outlet surface. In **Figure 4-11**, the input pressure is varied from 1 to 11 kPa at the inlet, and 0 kPa was set at the outlet boundary to generate

steady gas flow. An initial gap height of $5\ \mu\text{m}$ between the microvalve and the valve seat was needed for meshing to exist between the surfaces as the valve deflects away from the seat. Furthermore, the initial gap height presents a simulation of the actual assembly, where the gap height would exist from the fabrication processes.

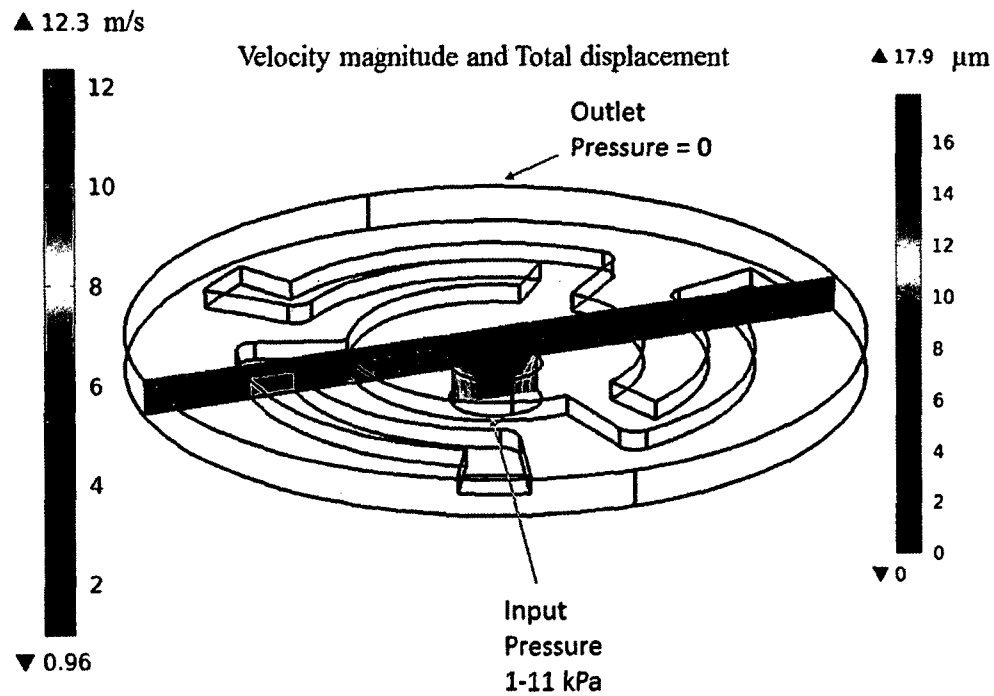


Figure 4-11: Fluid-structure interaction of microvalve with steady pressure-displacement, showing the cross section of the velocity magnitude and displacement of the microvalve with 7 kPa at the inlet.

The first validation of the Simulink model is shown in **Figure 4-12**, which shows the deflection of the microvalve as a function of input pressure matches the from the COMSOL results. Secondly, the transient response of the Simulink valve simulation (**Figure 4-13**) is compared to the transient result from **Figure 3-38**. Lastly, the mass flow rate as a function of the input pressure was compared in the COMSOL and Simulink result as shown in **Figure 4-14**. The lumped model simulation result of

the mass flow rate shows some deviations to the COMSOL results. For flow through an orifice with a valve plate, viscous and convective losses are represented as the loss coefficient, C_f in Eq. 4-12 to Eq. 4-15. Doll *et al.* [117] showed that there are different viscous and convective loss coefficient values at different gap heights that are nonlinear [117]. This would require interpolations from a data table in Simulink for different C_f values in relation to the gap height. To simplify the lumped model architecture, a single adjusted C_f value was used to obtain a close fit to the COMSOL mass flow rate curve in Figure 4-14.

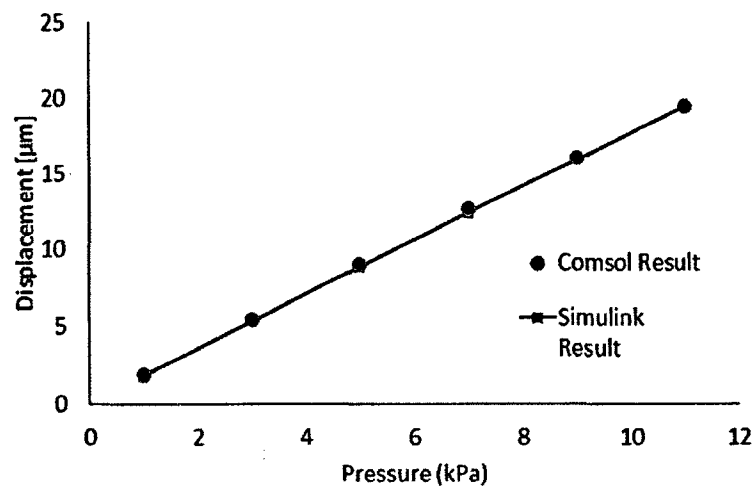


Figure 4-12: FSI result of the valve plate displacement at various constant inlet pressures.

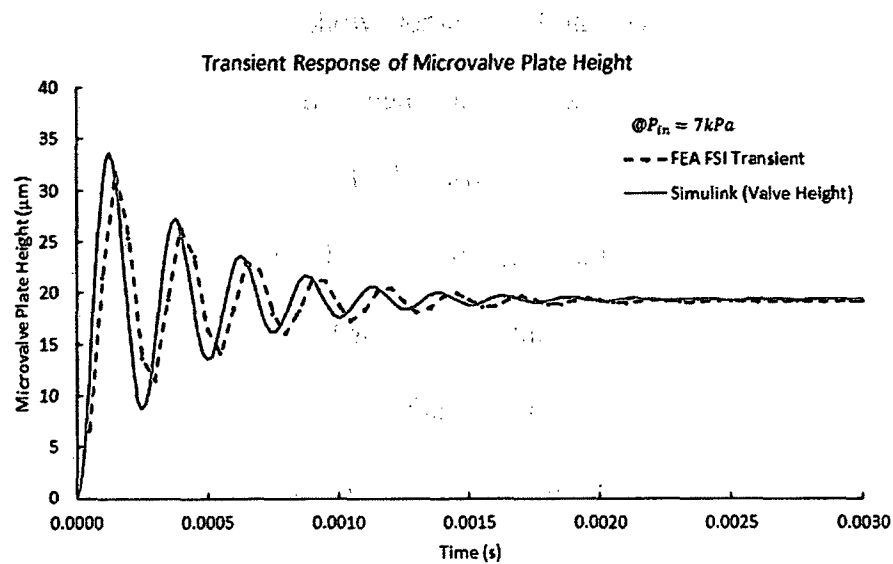


Figure 4-13: Comparison of the adjusted microvalve plate Simulink simulation result to the FEA FSI transient analysis result.

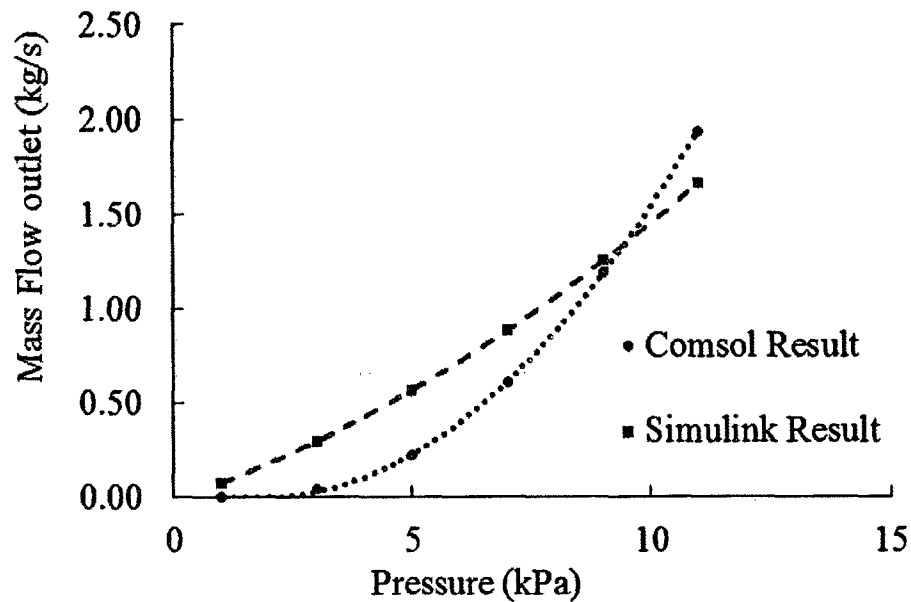


Figure 4-14: FSI result of the mass flow rate through the microvalve at various inlet pressure.

In this section, it was shown that the microvalve lumped model simulation developed in Simulink derived from the microvalve FSI FEA analysis utilizing both the

quasi-steady and transient FSI analysis matched well with one another with respect to the motion dynamics of the valve plate. However, comparisons of the simulated mass flow rate with respect to inlet pressure (**Figure 4-15**) shows some difference in the curves. The lump modeling of the mass flow rate through the microvalve relies on the Bernoulli equations (**Eq. 3-12** to **Eq. 3-15**) and require different loss coefficients at different gap height. An improved Simulink architecture to incorporate different C_f values would improve the results of the Simulink lump model in matching the FEA FSI mass flow rate results. Nonetheless, this provided a good approximation of the mass flow rate through the microvalves.

4.1.5.1 Microvalve Frequency Response

In the previous section, a lumped model simulation of the microvalve was developed and validated with FSI FEA. In this section, observation of the effect of the microvalve in response to cyclic pressure generated from the compressor chamber is shown in **Figure 4-15**. At high operation frequency, the dynamic movement of the closing and opening of the valve plate can lag behind the cyclic pressure change in the chamber. The microvalve plate cannot open fast enough for air to flow through in the suction phase, and it cannot close fast enough to prevent flow from coming back into the chamber during the compression phase.

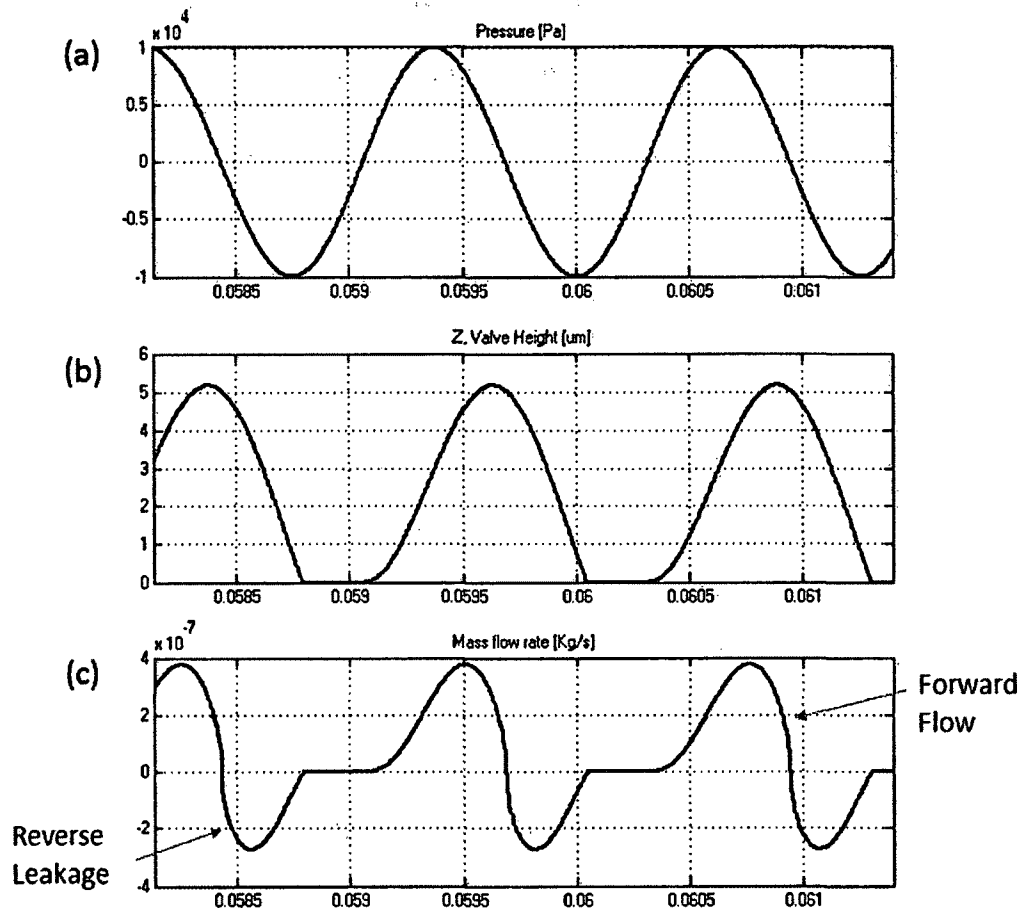


Figure 4-15: Microvalve lumped model dynamic simulation.

A frequency response of the microvalve height as a function of pressure frequency at the inlet microvalve was simulated. Sine function with a pressure of 10 kPa was set at the inlet to simulate the response of the valve plate height and its mass flow rate shown in **Figure 4-16**. It can be seen that reverse flow (reverse leakage) is apparent when there is negative pressure, and the microvalve is still in its open state.

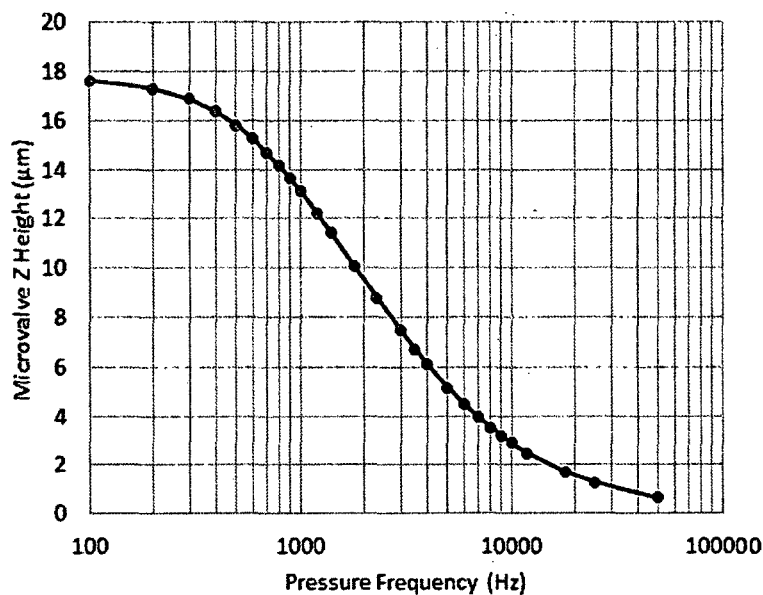


Figure 4-16: Frequency response of the valve plate height.

From **Figure 4-17**, it is observed that the total flow rate is attenuated as the pressure increases to higher frequencies. This is largely due to the attenuation of the valve plate gap height shown in **Figure 4-16**, where the reduction in the valve gap height further restricts the flow rate through the valve orifice. At higher pressure frequencies, the structural dynamics of the valve plate cannot react fast enough to respond to the fast pressure change; therefore, the valve plate will experience a change in pressure before reaching its maximum gap height. The reduction in the total flow rate through the valve orifice is also partly caused by the large reverse flow at higher frequencies. The increase in reverse flow at high frequencies is shown in **Figure 4-17** and can be seen from the valve dynamics plotted in **Figure 3-15**. Notice that the reverse flow decreases at pressure frequencies existing beyond 3.5 kHz. Beyond this frequency, the gap height will decrease below 7 µm, and as result, this

will limit the reverse flow. The relationship of the flow rate through the valve is described as

$$\dot{Q}_t = \dot{Q}_f + \dot{Q}_l \quad \text{Eq. 4-21}$$

where \dot{Q}_t , \dot{Q}_f , \dot{Q}_l is the total flow rate, forward flow rate, and leakage flow rate. The reduction of gas flow rate at high frequency is contributed more from the reduction in gap height rather than the reverse leakage.

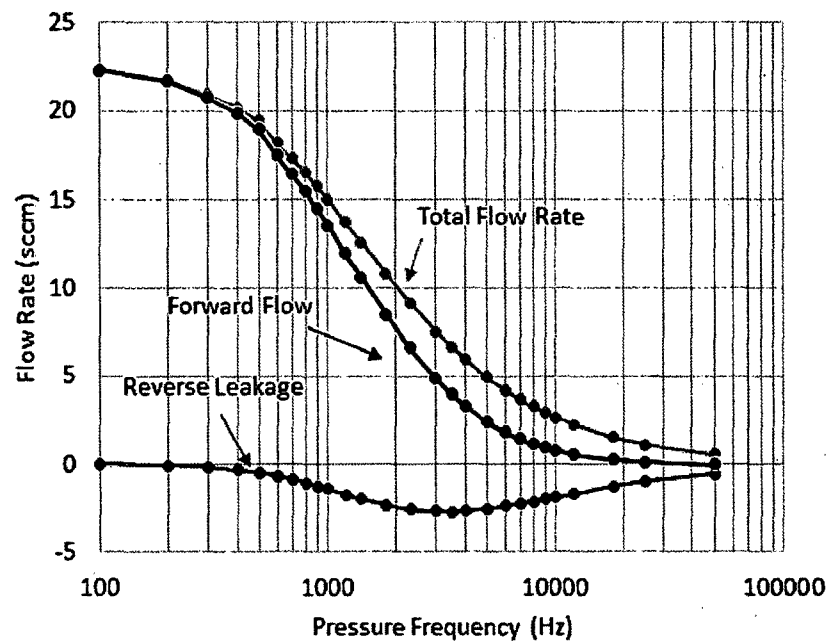


Figure 4-17: Simulation result of mass flow rate through the passive microvalve as a function of chamber pressure frequency.

4.2 Microcompressor Lumped Model Simulations

To realize a Simulink model of a two-stage microcompressor, the modeling and development approach were taken as follow:

1. The microvalve Simulink model was developed, simulated, and verified with the FEA in the previous section. Parameters were adjusted to match the FEA results.

The model is then integrated into the single-stage lumped model.

2. The single-stage Simulink model is developed, simulated, and analyzed.
3. A two-stage Simulink model is developed from the single-stage model.

This section discusses the details of the Simulink model architecture.

4.2.1 Single-Stage Microcompressor Simulink Architecture

The Simulink model of the microcompressor is divided into separate sub models with each representing its own set of equations as shown in the flow chart in **Figure 4-18**.

Parameters of the the single-stage compressor Simulink model is given in Appendix B.

Details of the single-stage compressor Simulink model is given in to **Figure B-1** to **Figure B-4**. The figure shows the coupled parameters and its flow from one set of equations to the next. To simulate the dynamics of the microcompressor model developed in **Figure 4-19**, various inputs were used.

1. The inlet pressure, P_{in} , is set to an atmospheric pressure of 101 kPa.
2. The outlet pressure, P_o , is set to a desired back pressure, the microcompressor compressor.
3. The drive frequency, f , is set to a frequency by the user.
4. V_d and V_s are set to a desired dead and stroke volume. The simulation output of the mass flow rate of the microcompressors, and the parameters such as the valve plate height, pressure variation in the chamber, and gas flow through the valves were monitored to examine the dynamics in the microcompressors.

Several assumptions are made in this simulation architecture.

1. V_d and V_s are set as a constant volume.
2. The sealed reverse leak rate, \dot{M}_l , caused by back pressure when the valve is in the closed position is neglected in this simulation design.

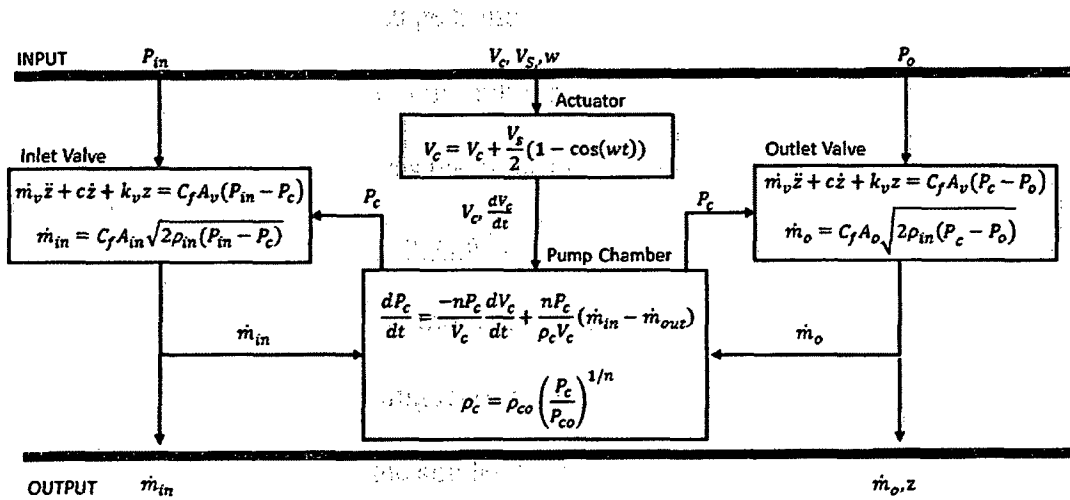


Figure 4-18: Flow chart of the variables and its relationship to each block in Simulink.

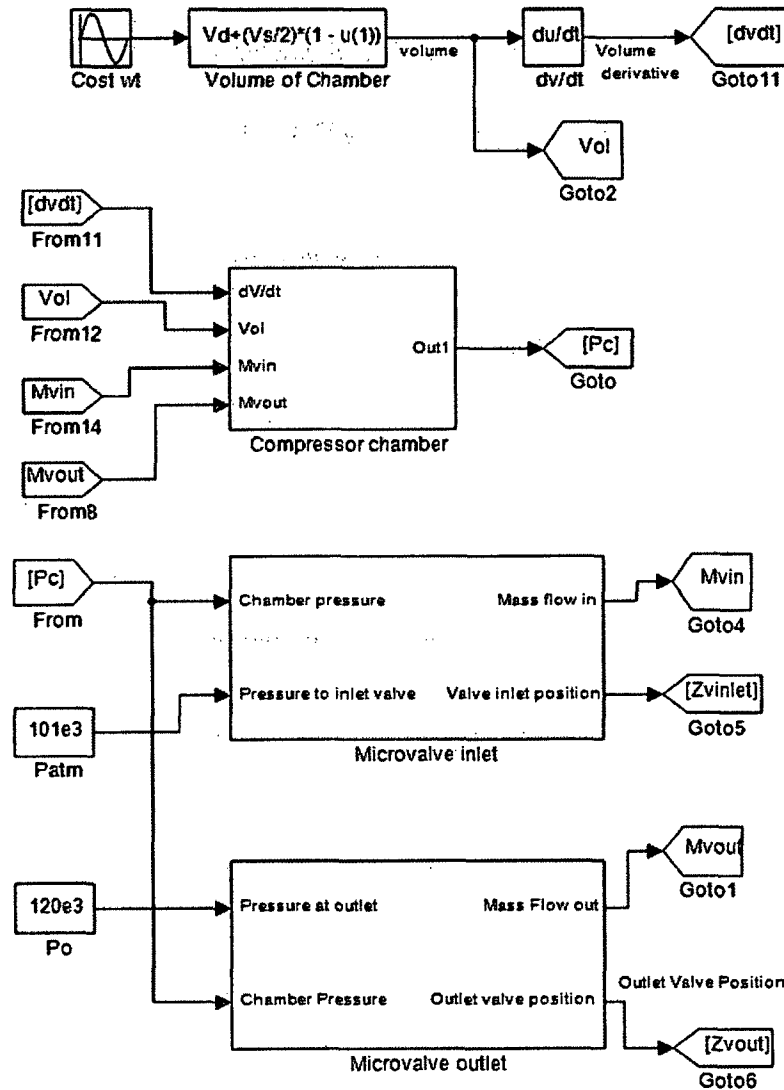


Figure 4-19: Simulink model of a single-stage microcompressor which include the pump chamber, volume chamber control, inlet and outlet microvalves block.

4.2.2 Compressor Chamber Model and Simulink Architecture

The compressor chamber is governed by Eq. 4-9 and Eq. 4-10. These equations are represented in the Simulink architecture in Figure 4-20.

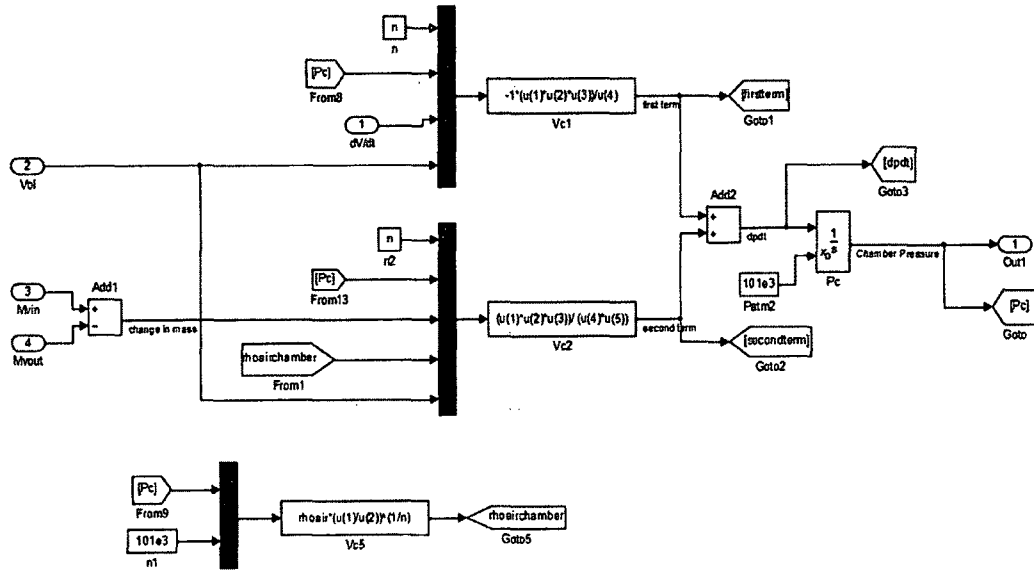


Figure 4-20: The Simulink architecture for a compressor chamber representing Eq. 4-9 and Eq. 4-10.

4.3 Simulink Simulation Results

4.3.1 Single-Stage Dynamic Simulation Results

The pump performance curve in **Figure 4-22** is determined from the Simulink simulation. To simulate this curve, the inlet pressure, P_{in} , is set to atmospheric pressure, and the back pressure (outlet pressure, P_o) is set to a desired constant value to observe the flow rate out of the microcompressor. To verify the Simulink architecture, the single-stage microcompressor dynamics is observed in **Figure 4-21**. It shows the inlet and outlet microvalves' response to the volume of the chamber and pressure generated.

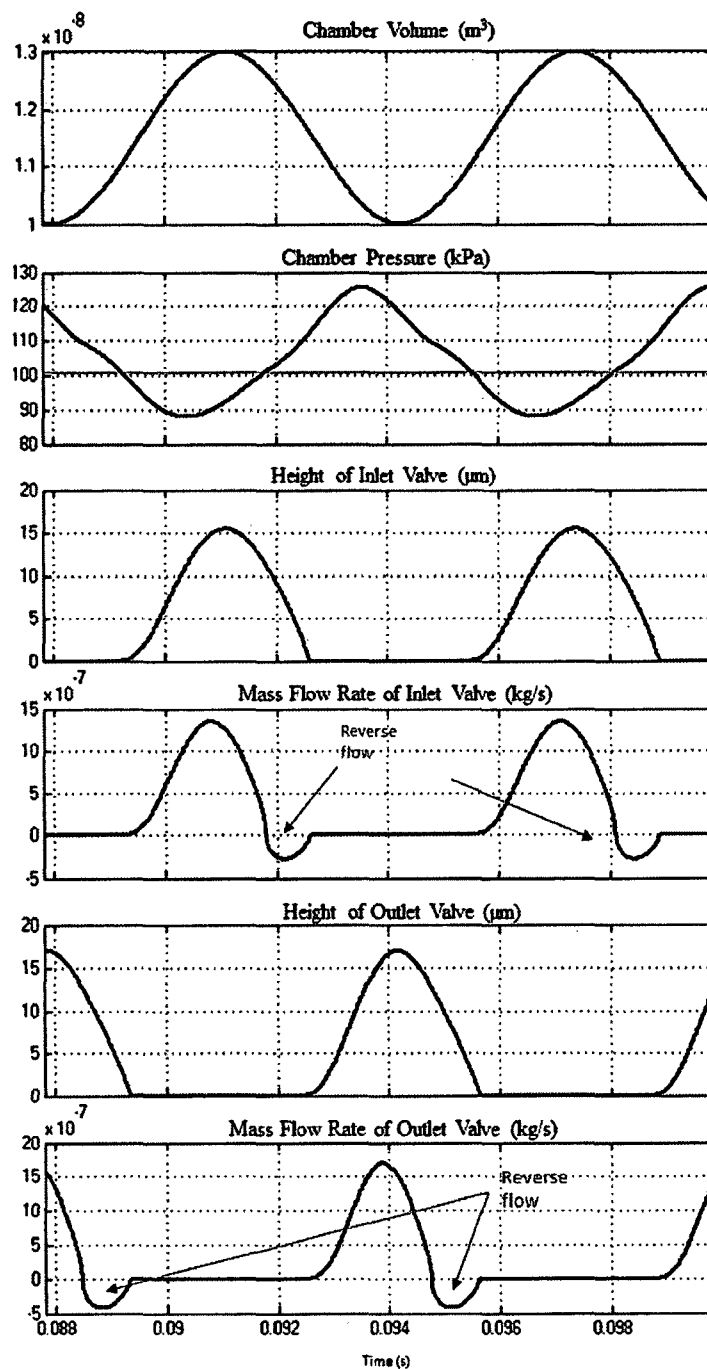


Figure 4-21: Dynamics of single-stage microcompressor. The chamber pressure is monitored along with the valve height and mass flow rate for the inlet and outlet valve, respectively.

The performance curve in **Figure 4-22** shows the flow rate at a different pressure ratio. The curve confirms that the maximum pressure ratio is dependent only on the

volume ratio of the chamber and independent of the actuation frequency. This is based on our assumption that the stroke volume is constant and independent of the actuation frequency. Operation at 1 kHz provided the best performance from the microcompressor. As the frequency increases, the flow rate decreases. A summary of **Figure 4-22** is provided in **Figure 3-20** where the maximum flow rate and maximum pressure ratio is extracted. For this design simulation, at frequencies higher than ~ 1 kHz, the maximum flow rate and the overall flow rate curve decrease. As discussed previously in Section 4.1.5.1, this is caused by the decrease in the gap height of the valve plate which significantly decreases the forward flow rate through the valve, and from reverse leakage at higher frequency.

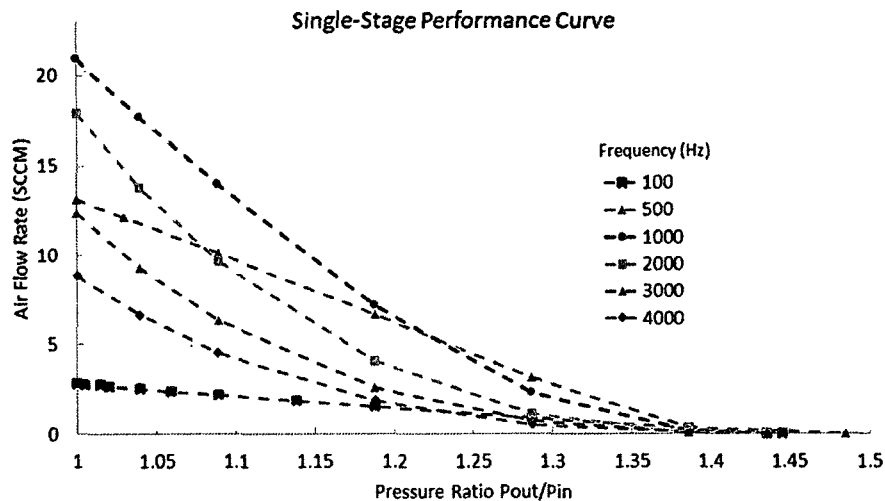


Figure 4-22: Performance curve for single stage microcompressor at different operation frequency.

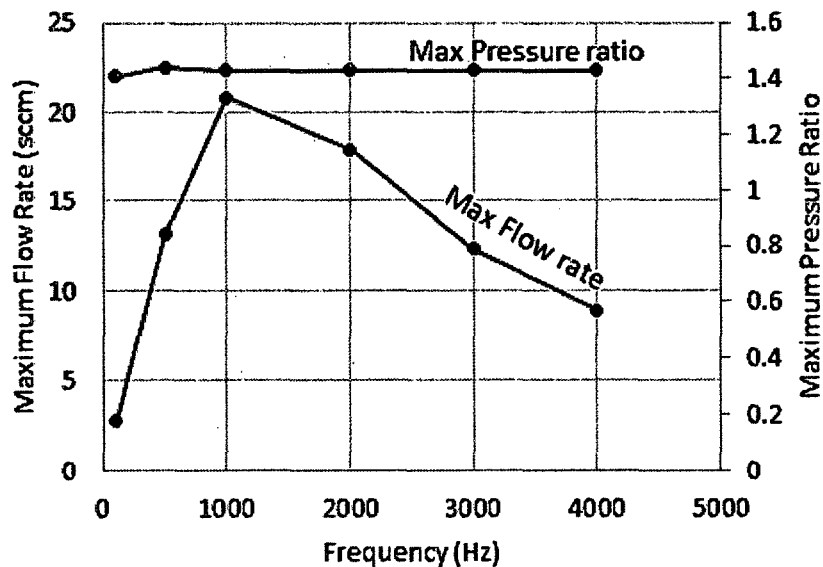


Figure 4-23: Summary of the single-stage microcompressor performance.

4.3.2 Two-Stage Simulink Model Configuration A

The two-stage microcompressor model is developed with two different configurations shown in **Figure 4-24**. The model for configuration A is modeled with the assumption that there is no dead volume at the interconnect chamber between the two stages; and it has one microvalve at the outlet of the first stage to control the transfer of gas to the second stage.

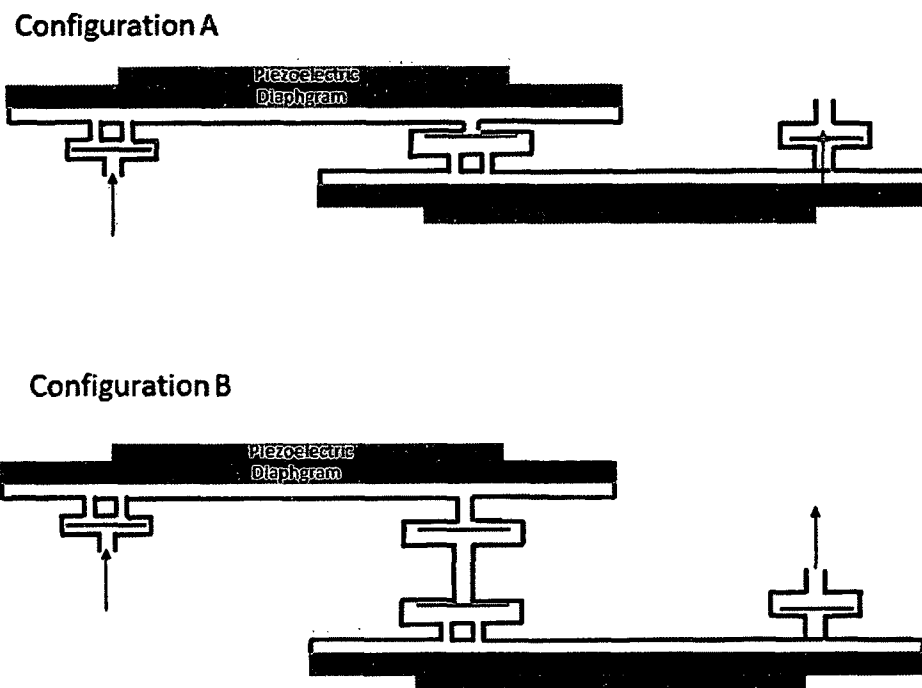


Figure 4-24: Schematic of a two-stage multistage microcompressor for configuration A and configuration B.

The two-stage microcompressor Simulink model utilizes the single-stage Simulink architecture to develop the multistage architecture shown in **Figure 4-25**. Details of the two-stage microcompressor Simulink model is given in **Figure B-5** to **Figure B-7**.

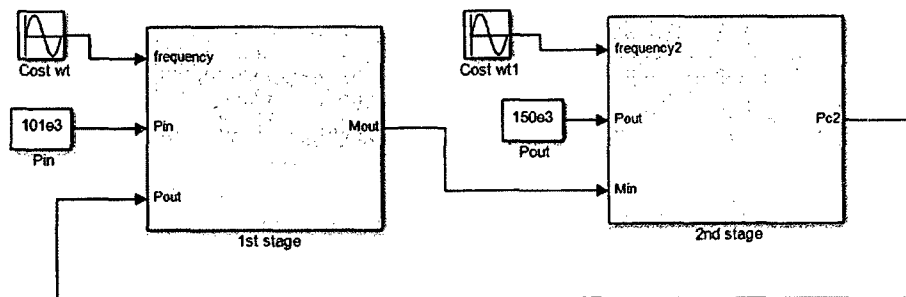


Figure 4-25: Simulink dynamic model of a two-stage multistage microcompressor.

4.3.3 Two-Stage Dynamic Simulation Results

The two-stage simulation is similar to the single-stage where the inlet pressure and outlet pressure are set to a value and the flow rate is observed. Each chamber has its own set of parameters, where the stroke volume and the chamber volume is set for each stage. A dynamic simulation scenario is given in **Figure 4-26**. In this simulation scenario, the two stage operates out of phase with the same stroke and dead volume for each chamber. The outlet backpressure of stage 2 is set to 150 kPa. Stage 1 is operated at 5X faster than stage 2 as seen by the volume of the pump chamber in **Figure 4-26(b)**. In **Figure 4-26(a)**, the pressure in chamber 2 experiences larger internal pressure in the chamber than chamber 1. In **Figure 4-26(c)**, the transfer of gas between stage 1 and stage 2, \dot{m}_{o1} , where gas flow out of the outlet valve from stage 1 occurs when the pressure in stage 2 falls below the pressure in stage 1. It can also be seen that gas transfer between the two stages does not occur when stage 2 is in the compression stroke. Reverse leakage is also observed between the transfer of gas between stage 1 and 2 in as shown **Figure 4-26(c)**. In **Figure 4-26(d)**, the flow rate at the outlet valve port of chamber 1, \dot{Q}_{o1} , and flow rate at the outlet valve port of chamber 2, Q_{o2} , is observed.

The multistage performance curve is shown in **Figure 4-27**, with both stages driven at the same frequency, and in phase with one another. In these conditions, the multistage stage exhibits similar results as the single stage, with an increase in the maximum pressure ratio. Similar to the single-stage microcompressor, flow rate begins to decrease beyond ~ 1 kHz threshold as shown in **Figure 4-27**. To further verify the

multistage simulation results, the simulated maximum pressure ratio is compared to the theoretical pressure ratio in **Table 4-2** which matches well with the theoretical value.

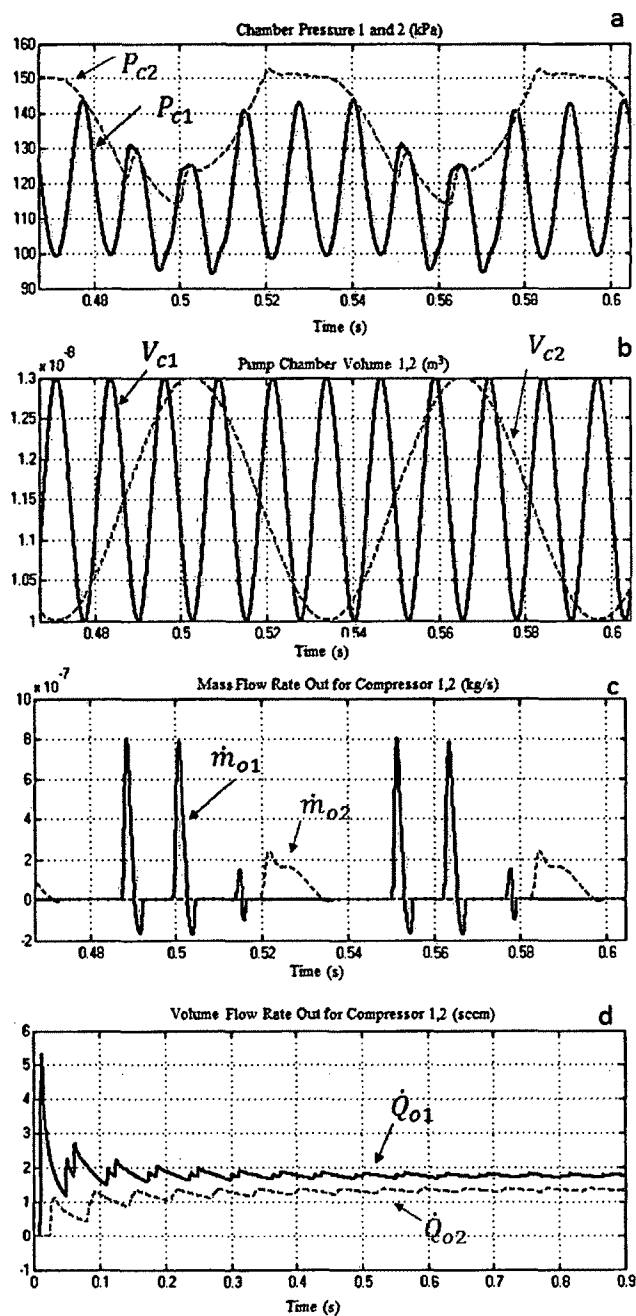


Figure 4-26: Dynamic simulation for a two-stage microcompressor. (a) volume for the 1st stage (in black) and volume for the 2nd stage (violet). (b) shows the current pressure in each chamber. (c) the mass flow rate through the interconnect microvalve and outlet microvalve. (d) shows the total flow rate out from stage 1 and 2.

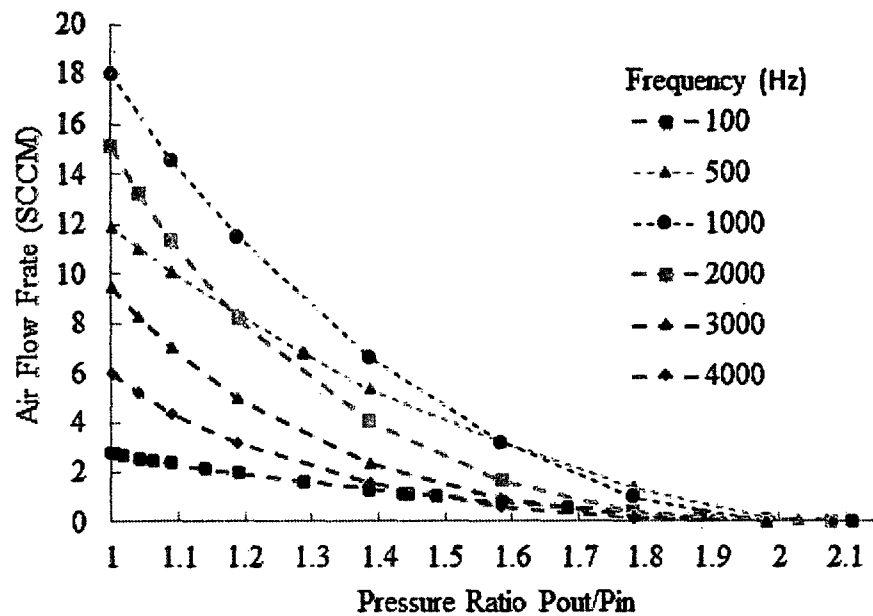


Figure 4-27: Performance curve for a two-stage microcompressor in series operating in phase. Stage 1 and 2 are operating at the same frequency.

Table 4-2: Theoretical pressure ratio comparison to the simulated pressure ratio from Simulink.

# of Stages	Volume Ratio, ϵ	Theoretical Pressure Ratio	Maximum Simulated Pressure Ratio
1	0.23	1.44	1.44
2	0.23	2.09	2.10

4.3.4 Two-Stage Drive Operational Scenarios

A study of the two-stage microcompressor (configuration A) driven at a different combination of frequencies is conducted to observe and determine the optimal drive input to achieve the best pressure ratio performances. The frequency in chamber 1 is simulated to operate at various frequencies relative to chamber 2 and vice versa. Additionally, the

two-stage is also simulated if operating in phase or out of phase will affect the pressure ratio. When operating in phase, it means that stage 1 and stage 2 will start off with the compressor driven in sync with one another in terms of the compression and suction stroke. When operating 180° out of phase, stage 1 would start off in the compression stroke and stage 2 in the suction stroke and would alternate cyclically. In instances where one stage operates faster than the other stage, $f_1 = 100$ Hz and $f_2 = 200$ Hz:

1. for an in phase operation, for every two cycles, stage 2 would be in phase with stage 1,
2. for an out of phase operation, for every two cycles, stage 2 would be out of phase with stage 1.

Simulation results in **Figure 4-28** show that as long as the two chambers are operating out of phase, the frequency ratio will not have an effect in lowering the pressure ratio from its theoretical value. When the two stages operate in phase, there are certain frequency ratios that will decrease the pressure ratio of the microcompressor. The worst case occurs when stage 2 operate in phase at 1X, 2X or 3X faster than stage 1. This can be explained from the dynamics simulations, which shows that there is no transfer of gas between each stage. In **Figure 4-28(a)**, when stage 1 is operating faster than stage 2, the overall pressure ratio is at maximum or close to the maximum pressure ratio of 2.08 regardless if it is in phase or out of phase. However, in **Figure 4-28(b)**, the pressure ratio performance is seen to deteriorate when stage 1's frequency is lower than stage 2 when they are in phase.

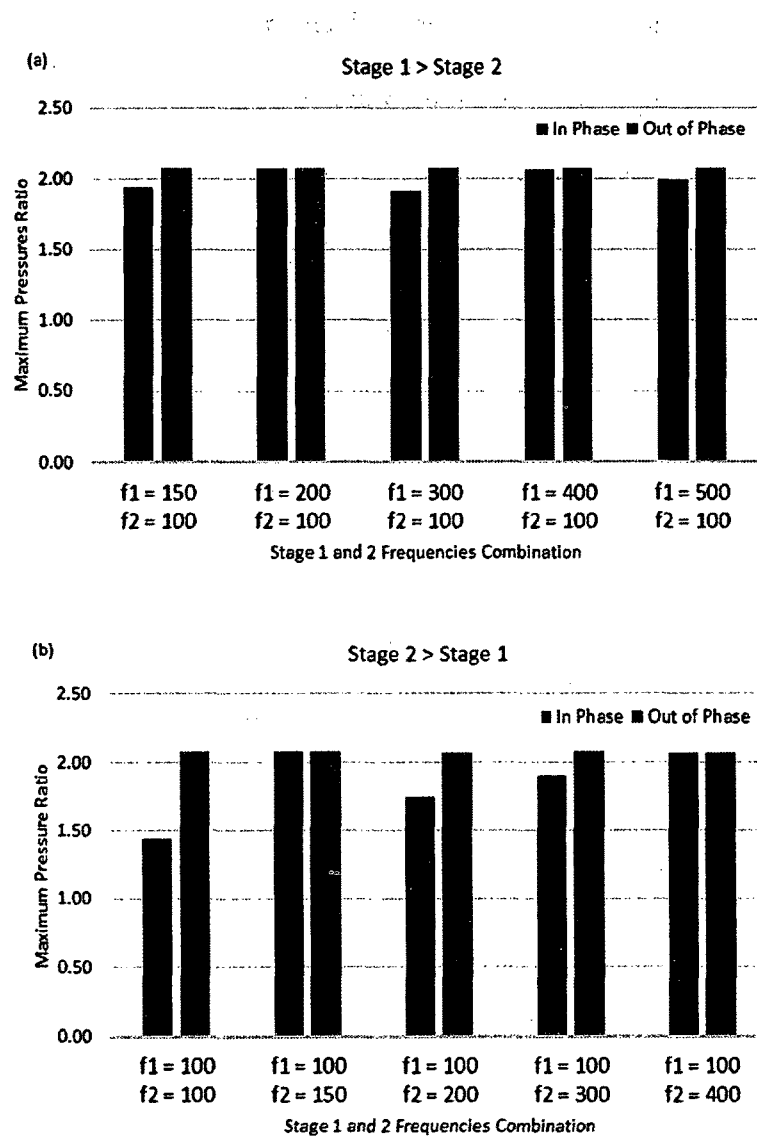


Figure 4-28: Simulated results of maximum pressure ratio generated. (a) Stage 1 operates at a higher frequency than stage 2. (b) Stage 2 operates at a higher frequency than stage 2.

4.3.5 Two-Stage Simulink Model Configuration B

This section investigates the two-stage multistage microcompressor with configuration B in **Figure 4-29**. This design case is more representative of a real case scenario where dead volume exists between the junctions of the micropump chambers. The volume of the interconnected chamber is investigated on how it will affect the

overall pressure rise of the multistage microcompressor. First, the modeling of this configuration and how the Simulink architecture changed from configuration A to configuration B is discussed. Next, effect of this interconnected volume has on the overall pressure ratio of the multistage microcompressor is shown and discussed.

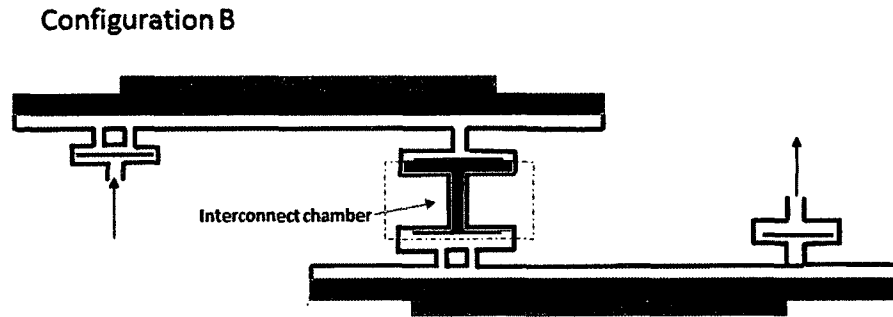


Figure 4-29: Multistage two-stage schematic of configuration B with an interconnecting chamber.

Comparing to configuration A, configuration B has two microvalves that exist between the two chambers. To model configuration B, the interconnect volume between the two chambers is considered as a pump chamber with constant volume and with no volume variation, where $\frac{dV_c}{dt} = 0$. As a result, **Eq. 4-10** is simplified to

$$\frac{dP_c}{dt} = \frac{nP_c}{\rho_c V_c} (\dot{m}_{in} - \dot{m}_{out}). \quad \text{Eq. 4-22}$$

For conventional purpose, **Eq. 4-22** is rewritten and given as

$$\frac{dP_{int}}{dt} = \frac{nP_{int}}{\rho_{int} V_{int}} (\dot{m}_{in_int} - \dot{m}_{out_int}). \quad \text{Eq. 4-23}$$

From **Eq. 4-22**, the variables that cause variations in the pressure of the interconnected chamber is the mass flow rate in and out of the interconnected volume. The multistage microcompressor B Simulink architecture is shown in **Figure 4-30**. An interconnected chamber model using **Eq. 4-23** is added to the multistage microcompressor lumped

model architecture as shown in **Figure 4-31**. **Figure 4-31** shows the first stage Simulink architecture, which includes the inlet and outlet microvalve architecture. **Figure 4-32** shows the interconnected chamber architecture with $dV/dt = 0$ and the volume V is the volume of the interconnected chamber. The interconnected chamber is considered dead volume that extends from chamber 1, which can lessen the pressure rise in stage 1.

Figure 4-33 shows the internal Simulink architecture of the second stage.

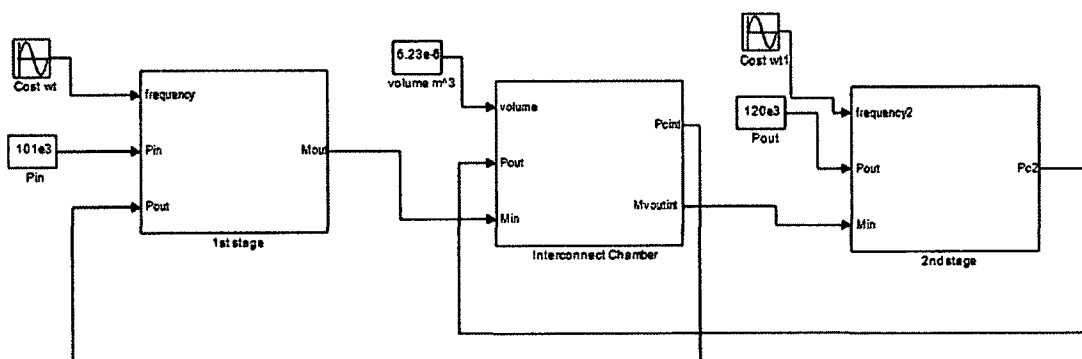


Figure 4-30: Simulink Architecture for a two-stage microcompressor configuration B.

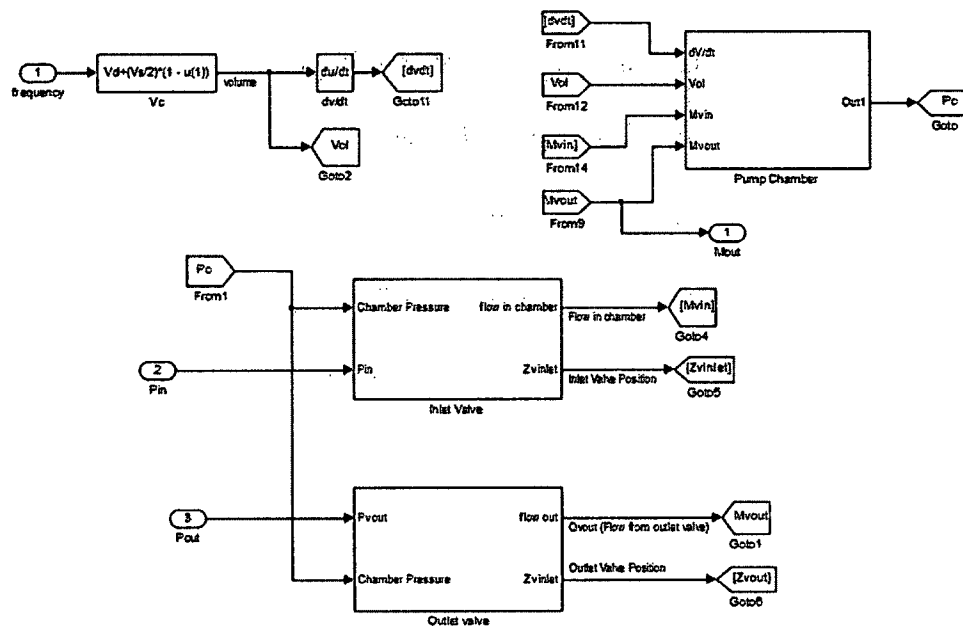


Figure 4-31: Internal architecture of the 1st stage Simulink block of the multistage microcompressor Simulink architecture.

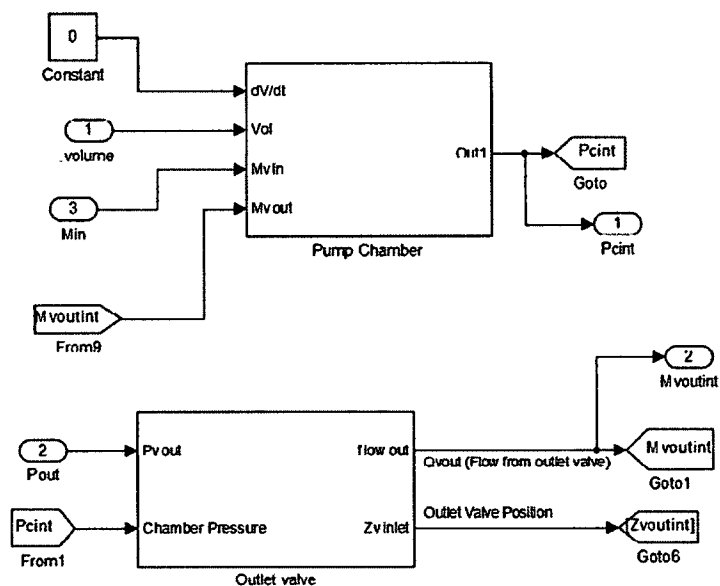


Figure 4-32: Interconnect chamber architecture.

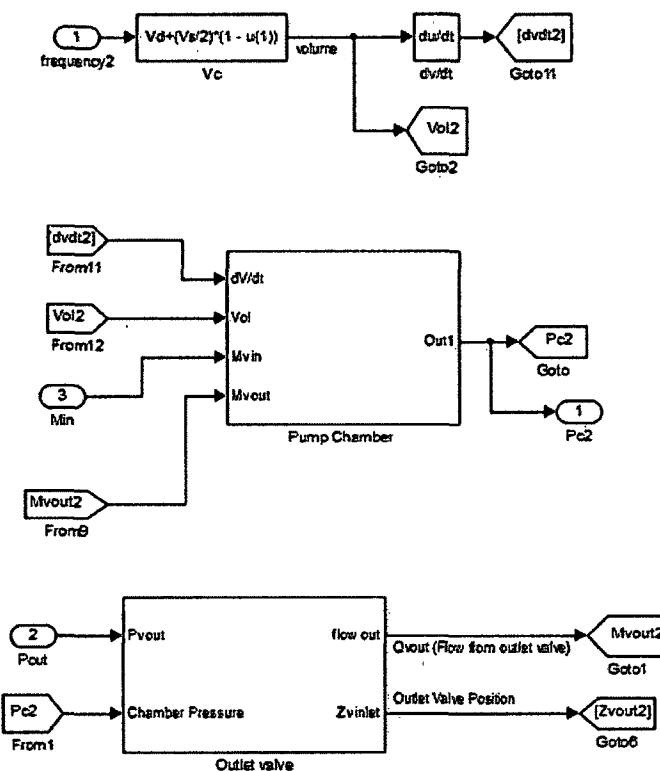


Figure 4-33: The internal architecture of the 2nd stage Simulink block of the multistage microcompressor Simulink architecture.

4.3.5.1 Multistage Microcompressor Configuration B Simulation Results

Here, the configuration B model is simulated with the same parameters as configuration A, with the two stages simulated in phase at 1 kHz. For configuration A, there is no interconnected volume, and it can be considered as configuration B with an interconnected volume of 0. From **Figure 4-34**, it can be seen that the multistage with minimal interconnected volume has the better performance curve. The performance curve in **Figure 4-34** shows the decrease in the maximum pressure ratio of the multistage compressor as the volume of the interconnected stage is increased.

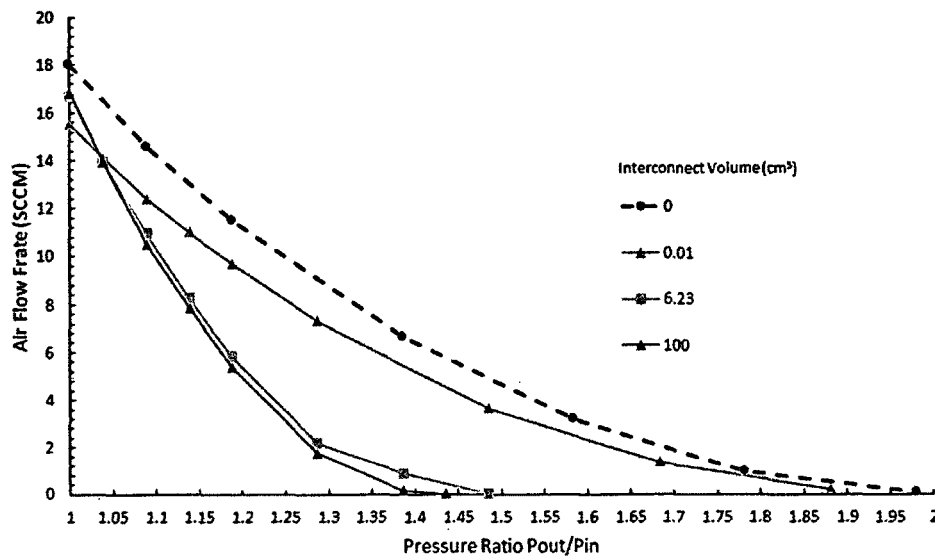


Figure 4-34: Performance curve simulation result for two-stage microcompressor with various interconnected volume (configuration B).

To validate the simulation results, the interconnect volume is considered as an extension of chamber 1 and calculated as dead volume as illustrated in **Figure 4-29**. Thus, for the two-stage microcompressor configuration B, the pressure ratio in **Eq. 4-5** is represented as

$$\frac{(P_o)_2}{(P_{in})} = \left(\frac{V_{s1} + V_{d1} + V_{I1}}{V_{d1} + V_{I1}} \right) \left(\frac{V_{s2} + V_{d2}}{V_{d2}} \right) \quad \text{Eq. 4-24}$$

where V_I is the interconnected volume. The design for the chamber 1 stroke volume, V_{s1} , is equivalent to the stroke volume, V_{s2} , for chamber 2, and the dead volume in chamber 1, V_{d1} , is the same as the dead volume in chamber 2, V_{d2} . The maximum pressure ratio from the performance curve **Figure 4-34** matches well with the analytical calculation (**Eq. 4-15**) in **Table 4-3**.

Table 4-3: Pressures ratio validation for two-stage microcompressor between Simulink and analytical results.

$V_{s1} = V_{s2}$ (cm ³)	$V_{d1} = V_{d2}$ (cm ³)	V_{I1} (cm ³)	$\frac{(P_o)_2}{(P_{in})}$ Simulink	$\frac{(P_o)_2}{(P_{in})}$ Analytical
0.003	0.01	0	1.98	2.09
0.003	0.01	0.01	1.88	1.76
0.003	0.01	6.23	1.48	1.45
0.003	0.01	100	1.43	1.44

4.4 Simulation Conclusion

The dynamics of a single-stage and a cascaded two-stage multistage microcompressor is presented and simulated in Simulink. Characterization of the airflow and valve interaction is implemented in COMSOL to generate and extract parameters for the dynamic equations for the microcompressor model. The Simulink microcompressor subsystem can be arranged in combinations of parallel and series to study its effectiveness in multistaging at the microscale. Ideally, unimorph piezoelectric actuator is used to create the compression and suction action of the gas in the chamber. Here, the volume displacement of the diaphragm actuator is modeled as an oscillating volume. The stroke volume is a linear function of the input voltage at low drive frequency. It becomes nonlinear near the resonance of the diaphragm actuator. Built up pressure load in the latter cascaded stages of the multistage compressor can cause a decrease in the stroke

volume from the membrane actuator as well. These two characteristics are not taken into account in this study to simplify the modeling and simulation of the microcompressor.

Minimal dead volume is most important in increasing the pressure ratio in a microcompressor. This simulation shows that the multistage cascaded series with passive microvalves will improve pressure ratio performance of the microcompressor. Others from [36], [42], [45] have shown multistaging to be effective for the micro gas compressor with electrostatic membrane utilizing electrostatic active valves that can control the gas flow between stages. Here the simulation showed that multistage micro gas compressor with passive valves can be as effective in multistaging as well, which, if successfully developed, may simplify the complexity of a multistage micro gas compressor.

CHAPTER 5

DEVELOPMENT OF THE SINGLE AND MULTISTAGE MICROCOMPRESSOR DEVICE

5.1 Introduction

Many iterations were made to develop the multistage microcompressor. The original goal was to fabricate a gas micro compressor using microfabrication method with silicon and glass wafer substrates. The process proved costly and time consuming, and many process developments were needed. We chose to meet the main goal of the research by investigating the feasibility and characteristics of a multistage microcompressor with passive microvalves by fabricating the device with a different approach. A larger scale micro gas compressor were designed to meet these goals eliminating the tasks of completely using MEMS microfabrication methods to prove the feasibility of a multistage with passive microvalves. Once proven, the miniaturization of the multistage microcomopressor in the microscale can be developed for future work such that a two stage can exist within the range of a 5 x 5 mm x 2 mm size.

A working single-stage microcompressor was needed in the first step to isolate some of the design flaws and to develop the fabrication processes and characterize the pump performances. In the second step, a two-stage microcompressor was developed to demonstrate the effectiveness of a multistage design.

5.2 Microvalve Fabrication

Researchers have developed microvalves with silicon [60] and polymeric materials such as parylene [5], polyimide [39], and SU8 [63]. Passive check valves are typically configured as a cantilever or tethered type. SU8 is fabricated with standard photolithography method and using either SiO₂ or Omnicoat as the release layer. The fabrication process is depicted in **Figure 5-1**.

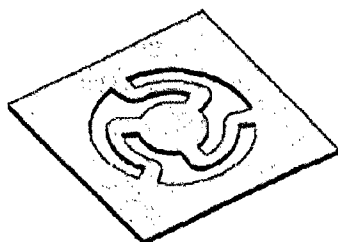
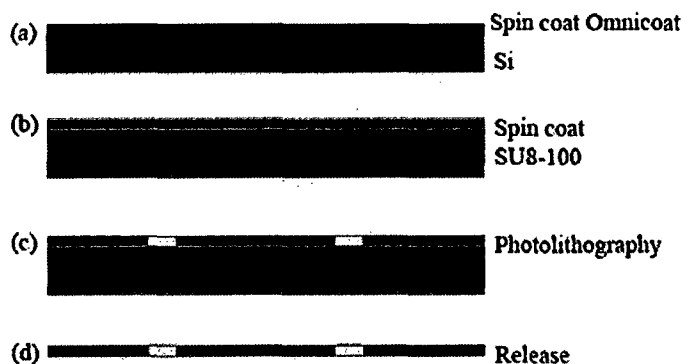


Figure 5-1: Microvalve fabrication steps.

A thin layer of Omnicoat by MicroChem was used as the intermediate layer for the release of the SU8 (from MicroChem) microvalves. It was spin coated on a 100 mm silicon wafer and baked for 200°C for 1 min and cooled. A 100 μm thick SU8-100 photoresist was spin coated onto the wafer and exposed to UV light with a high-resolution transparency mask. The exposed SU8 was developed with SU8 developer solution and rinsed with a mixture of SU8 developer and isopropanol. The preleased

image of the microvalve structure is shown in **Figure 5-2**. The substrate was placed in the MF-316 developer solution to remove the Omnicoat layer, which released the microvalves. It was observed that at low anneal temperature of 100°C prior to the release of the valve, the SU8 valves were brittle and prone to breakage when handled. At annealing temperature of 200°C prior to release, improvement in the valve strength and flexibility allowed it to be handled and function as a valve.

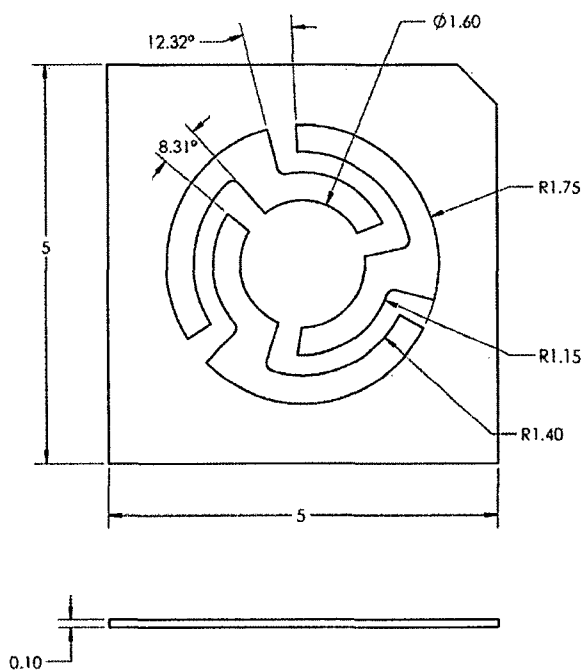


Figure 5-2: Image of microvalve structure on silicon substrate.

5.3 Single-Stage Design

5.3.1 Single-Stage Fabrication Process

The first single-stage design iteration shown in **Figure 5-3** is a design fabricated using mainly stereolithography (SLA) with a Formlab printer. The lower body housing was 3D printed with features incorporated to the body housing. Barbed tube nipples were

integrated to the lower body housing to allow for easy connection to the inlet and outlet port. Square recessed surfaces were integrated for the microvalve seats. A square thin plastic piece was laser cut to provide a reinforcement for the inlet microvalve. Another square thin plastic sheet was laser cut for the outlet microvalve seat. The released SU8 microvalves were assembled directly onto the lower housing with UV adhesive. The cutout plastic sheets were adhered to the microvalves and chamber with UV adhesive. A silicone sheet was laser cut into a flat O-ring shape to seal the chambers between the piezo disc and the chamber. Initial effort in sealing the piezo disc with UV glue and epoxy and mounting the piezo disc flat to the chamber surface was carried out. However, after operating the microcompressor a short period of time, the deformation of the piezo disc created a leak through the adhesives. Clamping with a plate and screws provided a better seal. A top body printed with SLA was used to clamp the outer edge of the piezo disc to the lower body housing with screws and bolts.

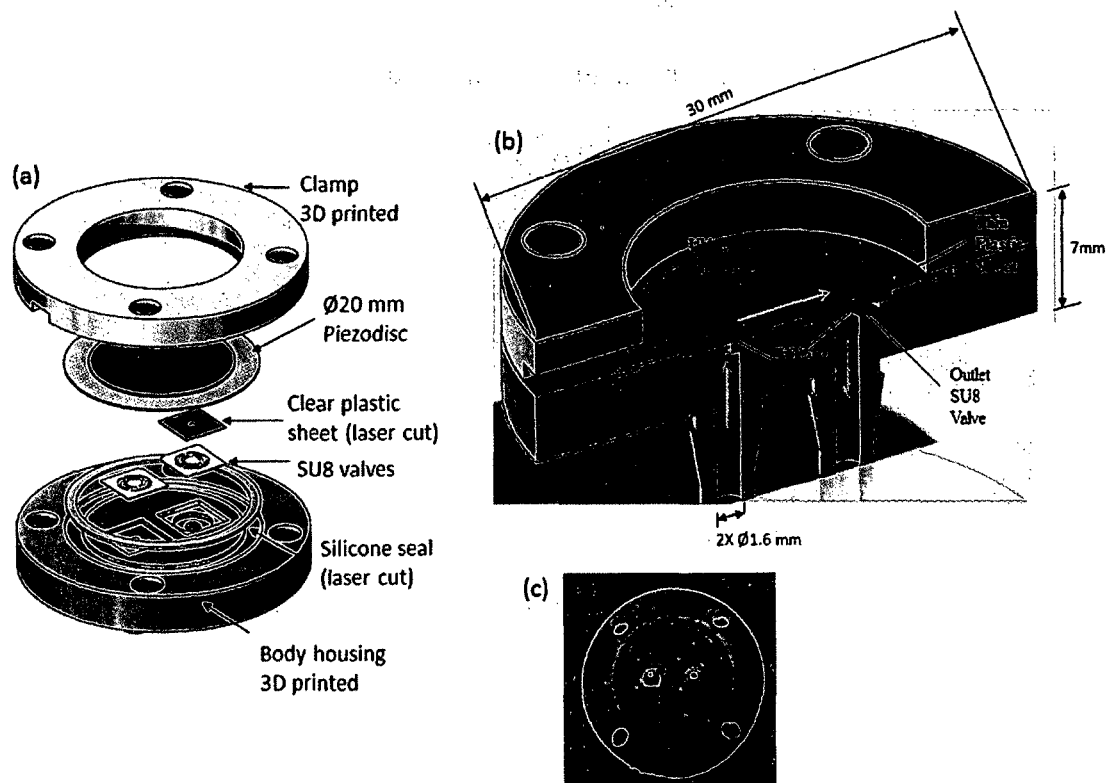


Figure 5-3: 3D printed model of single stage microcompressor.

The 3D printed microcompressor provided poor compressor performances for a few reasons. There were designs, fabrications, and assembly flaws which led to poor performances of the microcompressor.

Design Flaws:

- UV adhesive was used to adhere the thin plastic sheet on top of the microvalves. There was excess UV adhesive after the application process which would produce extra gap height between the piezo disc and chamber surface.

Fabrication and Assembly Flaws:

- The piezo disc chamber surface is designed to completely mate with the lower chamber surface. The SLA 3D print of the lower body housing produced non-

uniform flat surfaces of the lower chamber surface, which created gaps between the piezo disc and the chamber's surface. This increased the dead volume.

- The Formlab printer was unable to produce an accurate height dimension of the recessed area of the microvalve seat. The inconsistent dimension output from the 3D printer required that the recessed height to be larger than the stacked up dimension of the combined microvalve and plastic sheet thickness, so that the plastic sheet would not be higher than the chamber surface when assembled. This left some gap between the chamber surface and the recessed plastic sheet, resulting in more dead volume of the chamber.
- Large surface roughness resulted from the SLA output, resulted in poor valve sealing between the valve's surface and the 3D printed surface's seat, which resulted in large reverse flow leakage.

One of the challenges was the integration of the SU8 microvalves to the recessed seat. Since the microvalves were released from a silicon wafer, handling of the microvalves was a challenge. Several microvalves were broken during the handling process. The microvalves had to mate well with the valve seat's surface to provide a good seal when in the closed position. To attach the microvalves to the recessed area of the body housing, a small amount of UV adhesives was applied to the microvalve's outer edges and placed in the recessed area, and cured with UV light. Small amounts of UV adhesive seep between the microvalve's surface and its valve seat, which formed a thin layer of adhesive ranging from 5 to 40 μm thick. The extra layer of thickness could cause unwanted reverse leakage.

After the adhesive process, the microvalves were tested for reverse leakage using a syringe pump to pressurize air in the forward and reverse direction. To test for reverse leakage, a syringe pump was connected to the outlet port to test for the leakage in the outlet valve and similarly to the inlet port to test for leakage thru the inlet valve. For reverse leakage in the inlet valve, the syringe was pulled to create air suction. After the suction process, the syringe piston was released and check for the distance the piston returned away from its original position. For the outlet valve port, the syringe piston was compressed to create back pressure to the outlet microvalve. The syringe piston is then released to check if it fully returns to its original position.

The 3D microcompressor performance curve in **Figure 5-4** produced a maximum pressure rise of 1.7 kPa and a maximum flow rate of 120 sccm at its resonant frequency. Poor microvalve sealing and extra dead volume described previously resulted in low pressure rise. To mitigate this a different design is described in the next section.

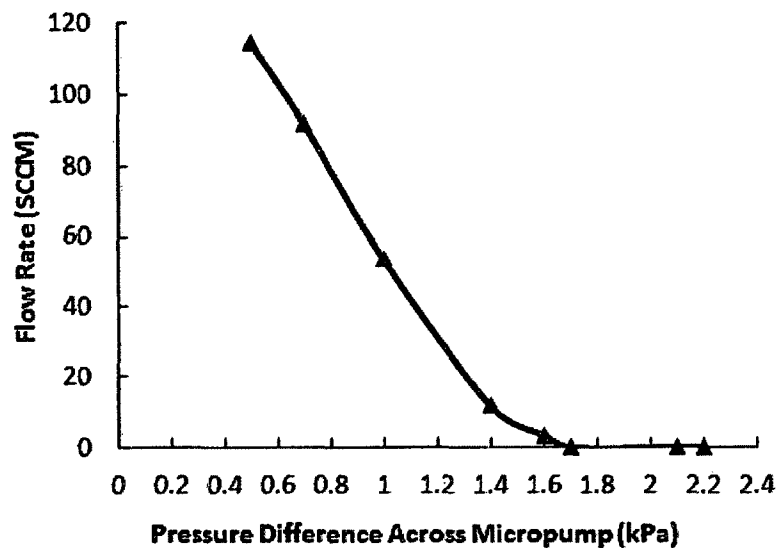


Figure 5-4: 3D printed microcompressor performance curve.

5.3.2 Single-Stage Microcompressor Design - Final Version

The flaws from the 3D printed prototype version required a new method of manufacturing the microcompressor with more precise parts and more predictable dimensions. Additionally, to produce the final version of the single-stage microcompressor shown in **Figure 5-5**; further improvement in the reduction of dead volume and reverse leakage from the microvalve was implemented. A redesign of the microvalve integration to the microcompressor was implemented by placing the microvalve on the bottom side of the thin layer membrane of the chamber surface of part IV. Efforts to reduce the dead volume of the chamber were conducted to maximize the pressure rise of the microcompressor by machining a flat plane for the chamber lower surface using a fly cutting tool.

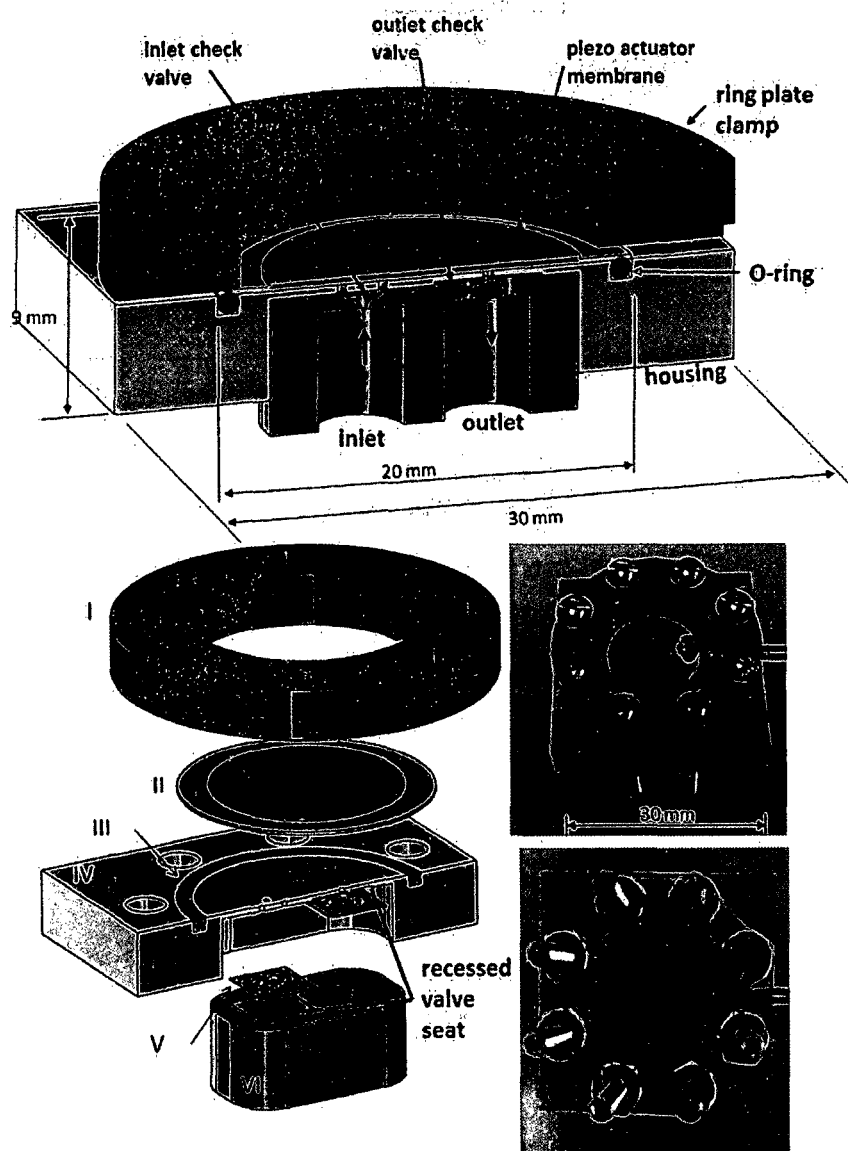


Figure 5-5: CNC single-stage microcompressor.

The single-stage microcompressor consists of the following components. The piezoelectric unimorph diaphragm is a $\text{Ø } 20 \text{ mm} \times 0.21 \text{ mm}$ thick piezo disc buzzer (part II), and is sealed with a $\text{Ø } 1 \text{ mm}$ thick $\times \text{Ø } 18 \text{ mm}$ ID O-ring placed in between the piezo disc and chamber surface (part III). The piezo disc is clamped with a ring plate (part I) held together with screws and nuts, providing easy access and interchangeability to the

chamber and piezo disc during testing. Part I was 3D printed with SLA using a Formlab 3D printer. The components' dimensions are given in **Figure C-1** and **Figure C-2**.

5.3.2.1 *Part IV Machining*

The CNC fabrication process for the microcompressor body presented a challenge of its own. Polycarbonate was the first material used to machine the microcompressor's body housings, and it resulted in many residual burrs from the cutting of the endmill. Acrylic is found to be easier to machine without any issues with residual burrs leftover from the edges.

A CNC Tormach was used to machine the microcompressor body parts IV and VI with acrylic. The chamber surface was machined flat as possible with a fly cutter tool. A 0.5 mm hole was drilled for the inlet port, and four 0.5 mm holes were drilled for the outlet port. The inlet and outlet port diameters were minimized to reduce dead volume without sacrificing too much pressure restriction from a small diameter hole. The radius ratio of the inlet to the valve plate was minimized to increase the sealing surface area. Fabrication from the CNC machine allowed for a smooth valve seat surface and accurate recessed depth for the O-ring. After machining, the housing parts were ultrasonicated for 20 min in DI water to remove residual particles attached to the parts from the micro drilling process.

5.3.2.2 *Assembly of the Single Stage Final Design*

The assembly of this single-stage involved the attachment of the microvalves onto the body housing of part IV and VI in **Figure 5-5**. In this design, the inlet microvalve is attached to the recessed surface of part VI with UV adhesive, and the outlet is attached to the recessed surface of part IV. The microvalves were applied to the recessed seat by

applying a small amount of UV adhesive to the edge of the released microvalve and carefully placing it on the microvalve seat, and curing it with UV light.

Careful attention was paid to the microvalve's assembly. A recessed surface roughness of $R_a = 3.9 \mu\text{m}$ was obtained with a 1-mm endmill to provide the sealing between the acrylic surface and SU8 valves. After adhering the microvalve with UV adhesive Loctite 3751, the inlet and outlet microvalves were checked for reverse leakage by attaching a syringe pump to the inlet and outlet port to apply reverse flow through the microvalves.

After the attachment of the microvalves to the body part IV and VI, these two body parts were joined together with epoxies, sealing the compressor. A syringe was filled with epoxies and injected at the filling port to fill the recessed area of the body's housings. Epoxies were used due to the acrylic not being transparent enough for UV light to transmit through and fully cure the UV adhesive. It was found that injecting epoxy after the acrylic was clamped provided the best adhesion and sealing between the housing. The single-stage microcompressor shown in **Figure 5-5** is assembled and clamped together with screws and nuts.

5.3.3 Single-Stage Performance with Model Fit

In this section, the single-stage microcompressor performance is evaluated experimentally and compared to the simulated model developed in Section 4.3.1. Results from **Figure 5-7** shows the performance of the fabricated single-stage microcompressor is much less than the simulated model. Leak test from **Figure 3-32** showed that when back pressure is applied to the microvalve in the closed position, the microvalve does not completely seal, and there exists some reverse leakage as a function of the back pressure.

Thus, a model of the reverse leakage is needed to be incorporated into the simulation model to obtain a more accurate fit to the test result. Here, this reverse leakage, \dot{M}_l , will be called the sealed-reverse leakage to differentiate between the dynamic reverse leakages of the microvalve. The magnitude of the sealed-reverse leakage of the microvalve is shown to be linearly dependent on the magnitude of back pressure and is modeled as

$$\dot{M}_l = \beta \Delta P \quad \text{Eq. 5-1}$$

where β is the rate of the reverse leakage per unit of pressure, and ΔP is the back pressure difference applied to in the reverse direction of the microvalve. The modified mass flow rate from Eq. 4-12 and Eq. 4-14 through the inlet and outlet microvalve is given as

$$\dot{m}_{in} = C_f A_{in} \sqrt{2\rho_{in}(P_{in} - P_c)} - \dot{M}_l \quad P_{in} < P_c \quad \text{Eq. 5-2}$$

$$\dot{m}_o = C_f A_o \sqrt{2\rho_c(P_c - P_{in})} - \dot{M}_l \quad P_c > P_{in}. \quad \text{Eq. 5-3}$$

Prior to the simulation, the theoretical dead volume and stroke volume of the fabricated microcompressor was determined to simulate an accurate model of the fabricated microcompressor. Since the microcompressor was designed with a CAD model and fabricated from CNC machining, the theoretical dead volume was determined from the dimensions of the microcompressor CAD model. The dead volume is mainly contributed from the holes of the inlet and outlet connecting to the microvalve as shown in **Figure 5-6**. The diaphragm is assumed to mate completely with the chamber surface; therefore, no dead volume is assumed between the piezo disc and the chamber's bottom surface. The calculated parameters for the fabricated model of the microcompressor are given in **Table 5-1**. With the dead volume, V_d , and stroke volume, V_s , given in **Table 5-1**,

the pressure ratio of the tested single-stage and two-stage microcompressor is compared to the theoretical pressure ratio without the leakage rate model in **Table 5-2**.

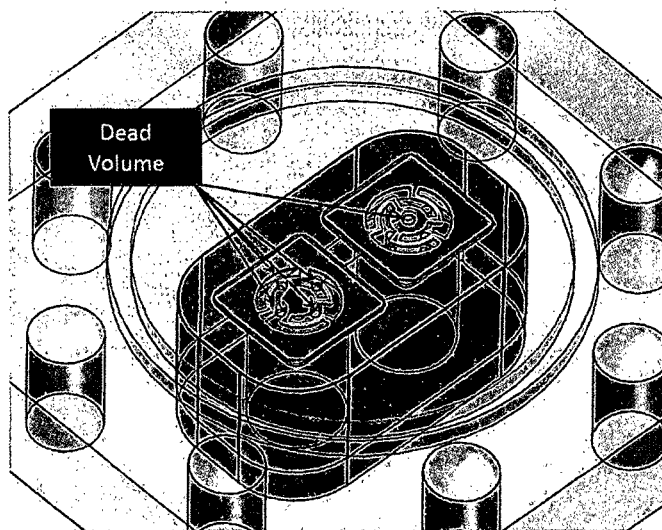


Figure 5-6: Dead volume of single-stage microcompressor.

Table 5-1: Parameter for simulation model.

$V_d(m^3)$	$V_s(m^3)$	$\beta(\frac{sccm}{kPa})$
		Experimental, from Table 3-8
7.86×10^{-9}	4.8×10^{-9}	0.147

Table 5-2: Comparisons of the theoretical pressure ratio to the single-stage and two-stage fabricated device with respect to the calculated volume ratio of the assembled device.

# of Stages	Volume Ratio, ϵ	Theoretical Pressure Ratio	Pressure Ratio of Fabricated Device
1	0.38	1.95	1.09
2	0.38	3.8	1.18

The pressure ratio of the fabricated devices is significantly less than the theoretical pressure ratio, which can be caused by reverse leakage shown in **Figure 5-7**. In **Figure 5-7**, the effect of the sealed-reverse leakage has on the microcompressor performance can be seen. The increase in sealed-reverse leakage significantly affects the pressure-flow performance curve. With the dead volume and stroke volume from **Table 5-1**, and β adjusted from 0.147 sccm/kPa to 2.45 sccm/kPa, the simulated model closely matches the single-stage performance curve. Details of the test results is described in the next chapter.

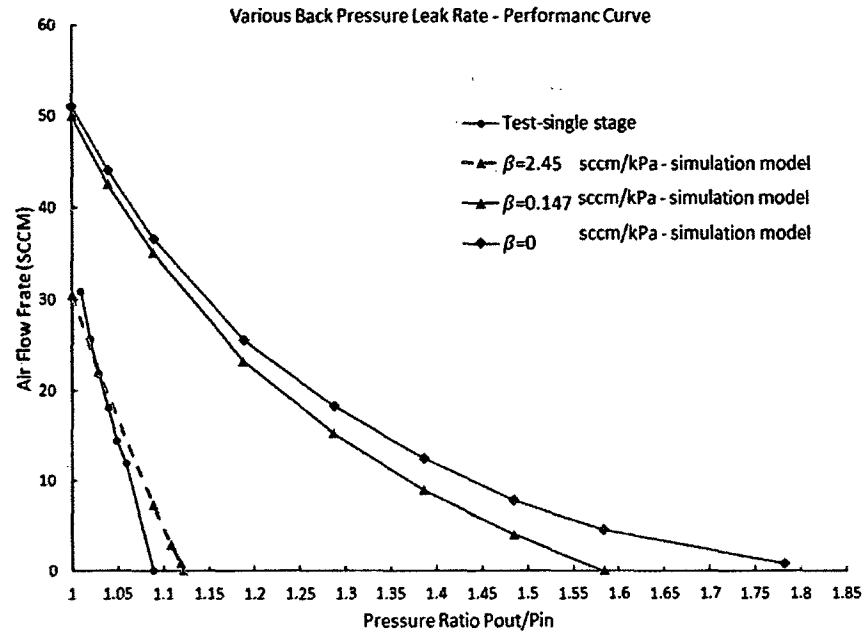


Figure 5-7: Modeled performance curve compared to the experimental curve of single-stage with various back pressure leak rate.

5.4 Multistage Two-Stage Design

The multistage microcompressor (two-stage) shown in **Figure 5-8** and **Figure 5-10** is designed with a similar configuration to the single-stage design. A cross-section of the two-stage designed is shown in **Figure 5-9**. The components' dimensions are given in **Figure C-3** to **Figure C-5**. Two passive micro check valves are used for each chamber. The first stage is placed at the top and the second stage is placed at the bottom overlapping the first to minimize the overall size of the device. An O-ring is used to seal the piezo disc actuator and the chamber for each stage. The housing consists of a bottom, middle, and top body, which were machined from acrylic material.

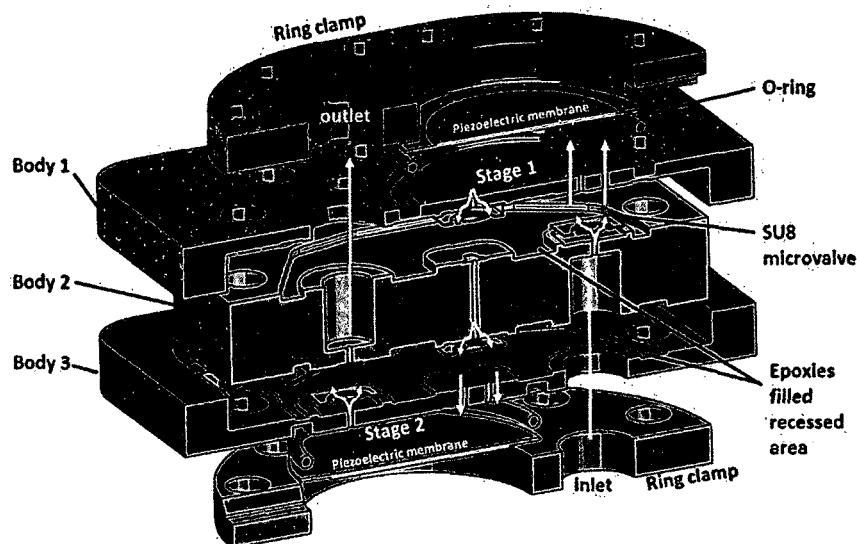


Figure 5-8: Cross-section and exploded view of the two-stage microcompressor design.

In **Figure 5-8**, four passive micro check valves were placed on and adhered to the recessed areas of the housing bodies 1, 2, and 3 with UV adhesive before bonding the three bodies together with epoxies. The first microvalve is adhered to the inlet recessed area of body 2 with UV adhesive. This serves as the inlet microvalve for stage 1. The second microvalve adheres to the recessed area of body 1, serving as the outlet microvalve for stage 1. The third microvalve adheres to the backside of the recessed area of body 2, serving as the inlet microvalve for stage 2. The fourth microvalve adheres to the backside recessed area of body 3, serving as the outlet microvalve.

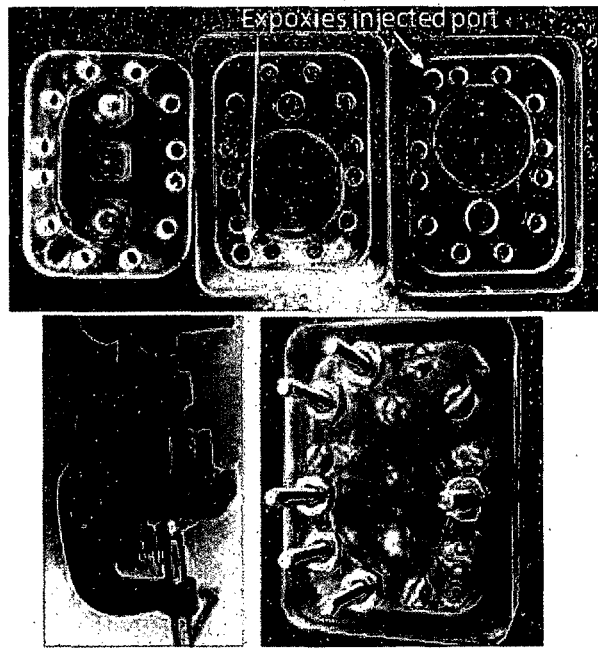


Figure 5-9: Injection of epoxy into the cavity for bonding and sealing. Assembly is screwed together and clamped at the center to ensure no epoxy flow into the valve surface.

The next step involved the bonding of the three body housings. The assembly of the multistage compressor required the three body housings, 1, 2, and 3 in **Figure 5-9**, to have a good seal with the epoxy bond to prevent any gas leakage in between which can compromise the compressor performance. Shown in **Figure 5-9**, a filling port was drilled in bodies 1 and 2 to provide a port for the filling of epoxies. Epoxies were used in replacement of UV adhesive due to acrylic not being transparent enough for UV light to transmit through and fully cure the UV adhesive. It was found that injecting epoxy after the acrylic was clamped provided the best adhesion and sealing between the housing.

To complete the bonding process of the three bodies, the parts were mated together via self-alignment, by their rectangular shape, and provided a slip fit from the close tolerance machining processes. When assembled together, bowing of the thin wall of the chamber plane was noticeable from the stress of the machining process. As a result

of this, when the cavity was filled with epoxies, it seeped into the valve seat. Clamps were used to push down on the bowing while holding the three housings together along with the screws and nuts as shown in **Figure 5-9**. A syringe pump was used to inject the epoxies into the cavities in between bodies 1 and 2, and between bodies 2 and 3. When the cavity was filled with epoxies, an air pocket was noticeable. To prevent the air pocket in the filling process, an air relief hole was drilled in bodies 1 and 3, allowing for better epoxies flow. Once the epoxies were filled in both cavities, the assembly was cured for 24 h with the clamps and screws on. After the curing process, the screws and clamps were removed.

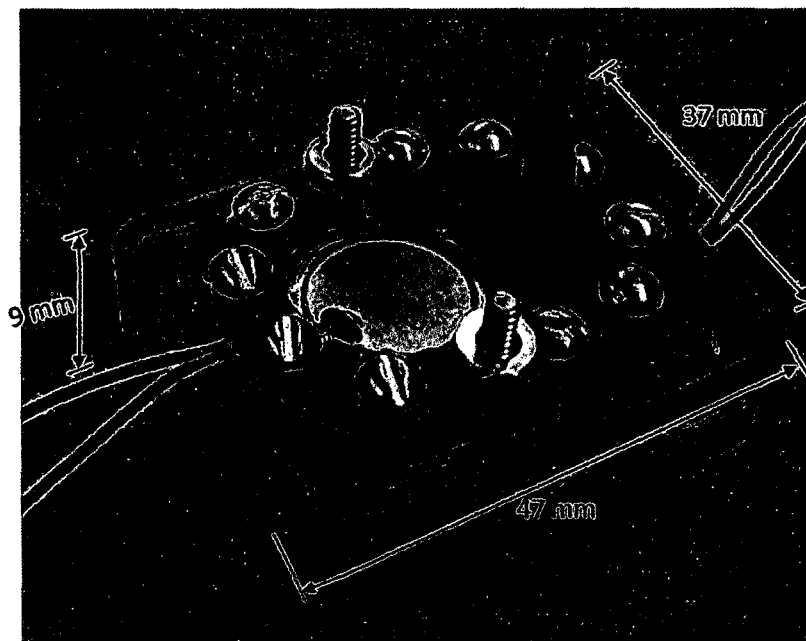


Figure 5-10: Photograph of the two-stage micro gas compressor.

The final assembly required the two O-rings and the two piezo discs to be placed on the bonded body assembly using the two clamp plates and secured in place with screws and bolts as shown in **Figure 5-10**.

CHAPTER 6

MICROCOMPRESSOR TESTING, RESULTS, AND DISCUSSION

This chapter presents the testing and characterization of the finalized single-stage and two-stage microcompressors by evaluating their performances; this is implemented by measuring the pressure-flow rate curves. Testing of the single-stage performance curves allows for a baseline comparison with the two-stage, which can prove the success and capabilities of utilizing multiple stages. The dynamics performance of the microcompressor is characterized by driving the microcompressor across its operating frequency range.

6.1 Test Setup

A schematic of the pressure-flow test setup is illustrated in **Figure 6-1**. A Dwyer Series 475 Mark III digital manometer was used to measure the pressure rise. Flow rate is measured by placing the output air tube into a volumetric glass tube partially submerged in water. Change of volume in the water inside the glass tube is measured over time to determine the output flow rate of the microcompressor. A needle valve was used to restrict the flow rate and generate various levels of back pressure from the micro gas compressor during operation. In addition, a Laser Doppler Vibrometer (LDV) system was used to measure the center deflection magnitude of the microcompressors piezo disc. The LDV system provided a fast fourier transform (FFT) analysis to determine the deflection response of the diaphragm at varying drive frequency. To drive the

compressors, sine wave signal from the function generators were input to custom signal voltage amplifiers [118] to the drive compressor at 60 Vpp with piezoelectric bipolar actuation.

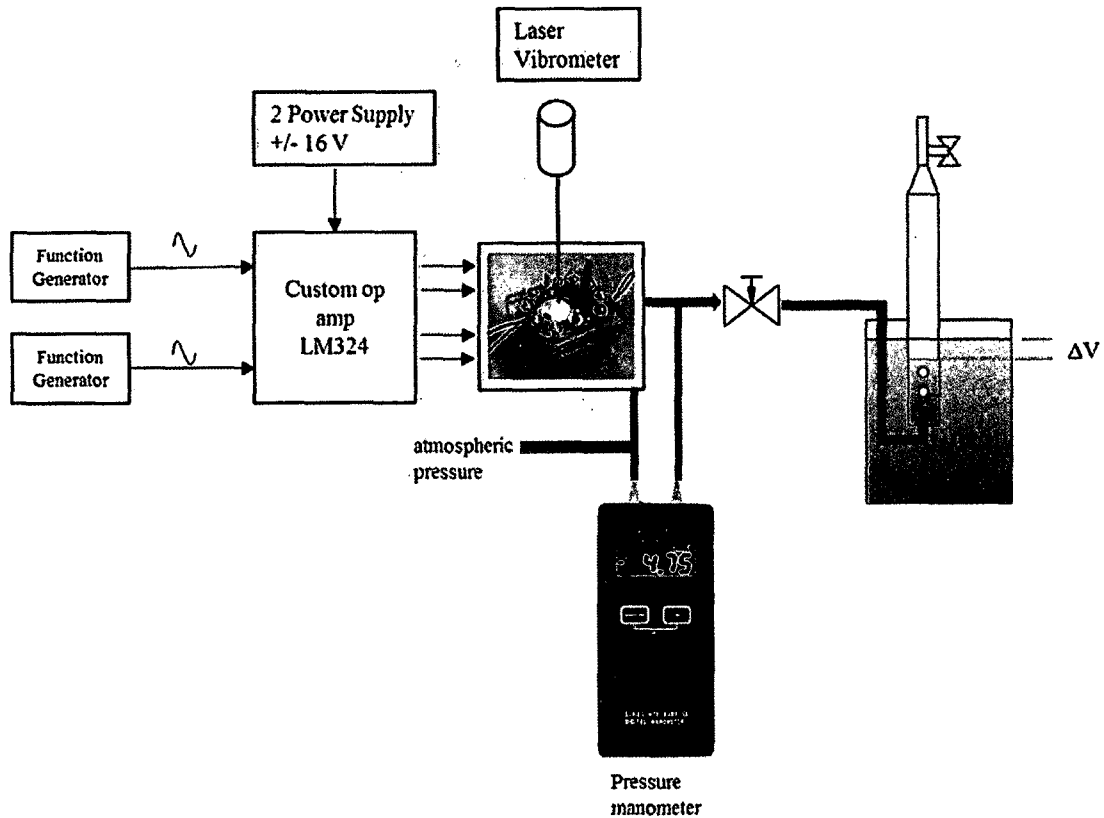


Figure 6-1: Performance curve and deflection test set-up.

For the two-stage compressor, each stage is driven independently with its own function generator. To tune the multistage microcompressor to its maximum pressure rise, each stage was tuned to its own resonant frequency while the other stage was turned off. After the 1st stage was tuned, the second stage was ramped up to its own resonant frequency to generate the maximum pressure rise from the multistage.

6.2 Single-Stage Microcompressor Test Results

From the measured pressure-flow performance curve in **Figure 6-2**, the single-stage microcompressor produced a maximum pressure rise of 9.5 kPa at zero flow rate and a maximum flow rate of 32 sccm at zero back pressure; this was driven at 60 Vpp tuned to the piezoelectric diaphragm resonance. The microcompressor produced its max pressure rise at 5.8 kHz closely matching the resonant frequency of the finite element model (FEM) result of 5.4 kHz. The variation in resonance can be attributed to the differences in the exact material properties, diaphragm construction and constraint of the piezoelectric diaphragm as assumed in the Simulink model. The diaphragm construction showed a non-concentric position of the piezo layer to that of the brass layer, which also may alter the resonant frequency. Secondly, the finite element model was modeled as a fixed constraint at the outer radial edges, while the actual model is constrained with the clamping of the ring plate and O-ring as described in Section 3.1.6. At the resonant frequency, sine wave voltage signal from the function generator supplied to the op amp generated 0-60 Vpp.

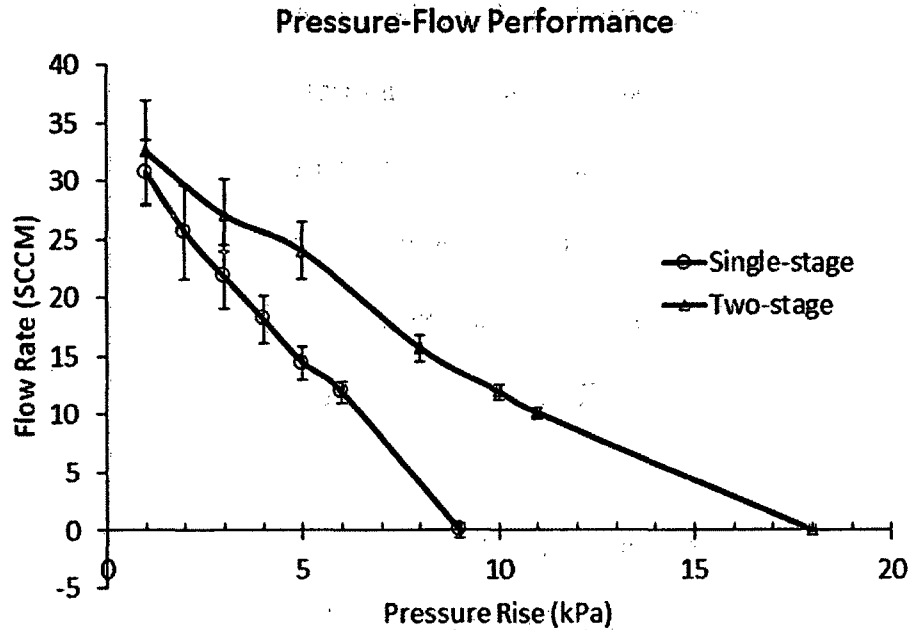


Figure 6-2: The pressure-flow performance curve of the single and two-stage microcompressors.

To characterize the voltage dependency of the microcompressor, input voltage of 0-60 V_{pp} was applied to the single-stage microcompressor. The maximum pressure rise was measured by plugging the outlet tube of the microcompressor, allowing zero flow rate output. The measurement was taken by first tuning the resonant frequency of the microcompressor, then a varying voltage was applied to the piezoelectric diaphragm. Maximum pressure rise was obtained once the pressure reading from the pressure manometer stabilized to its maximum. It can be seen from **Figure 6-3** that the increase in voltage generated larger pressure rise from the microcompressor. From the study in Section 3.1.6, it shows that the voltage increase resulted in an increased deflection of the diaphragm, thus increasing the stroke volume of the microcompressor chamber. It was found that voltage greater than 60 V_{pp} degraded

the diaphragm, which may have delaminated the PZT from the electrodes, resulting in a damaged piezoelectric diaphragm actuator.

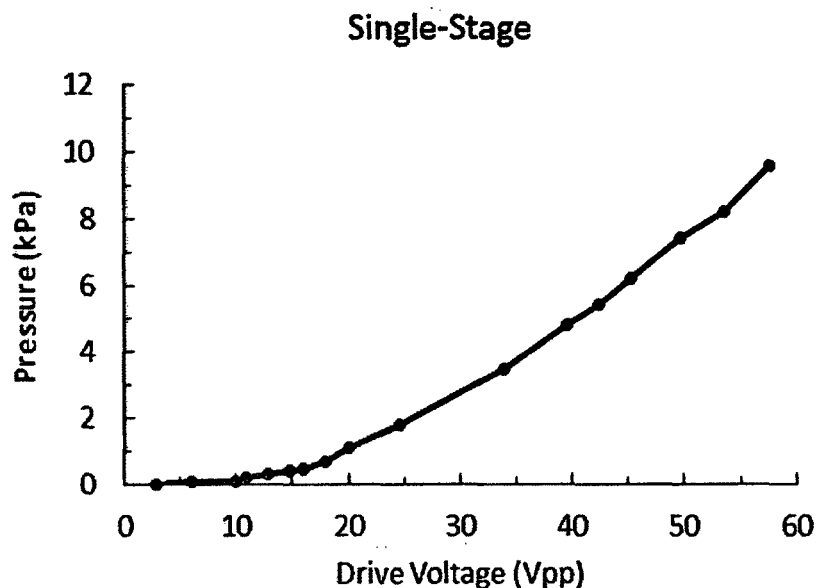


Figure 6-3: The pressure rise of the compressor at its maximum resonant frequency with different voltage applied to the maximum operating voltage of the piezoelectric diaphragm of 60 Vpp.

A frequency sweep of the single-stage and two-stage devices were conducted to observe their frequency response. **Figure 6-4** shows an overlap of the single-stage microcompressor pressure rise and the piezoelectric diaphragm deflection driven with a sinusoidal max input voltage of 60 Vpp. This test was carried out with the experimental setup similarly shown in **Figure 6-1** but with the outlet plugged, allowing zero flow rate. As observed from **Figure 6-4**, the single-stage microcompressor, generated most of its pressure rise at the diaphragm resonant frequency. At the peak of the pressure rise of the microcompressor, the diaphragm deflection shows a decrease in its deflection. Under large back pressure, the diaphragm can only generate a maximum deflection of 10 μm . Additionally, it was

observed that the microcompressors were sensitive to the tuning of the diaphragm frequency and needed to operate near the resonant frequency of the piezo disc to generate a significant pressure rise.

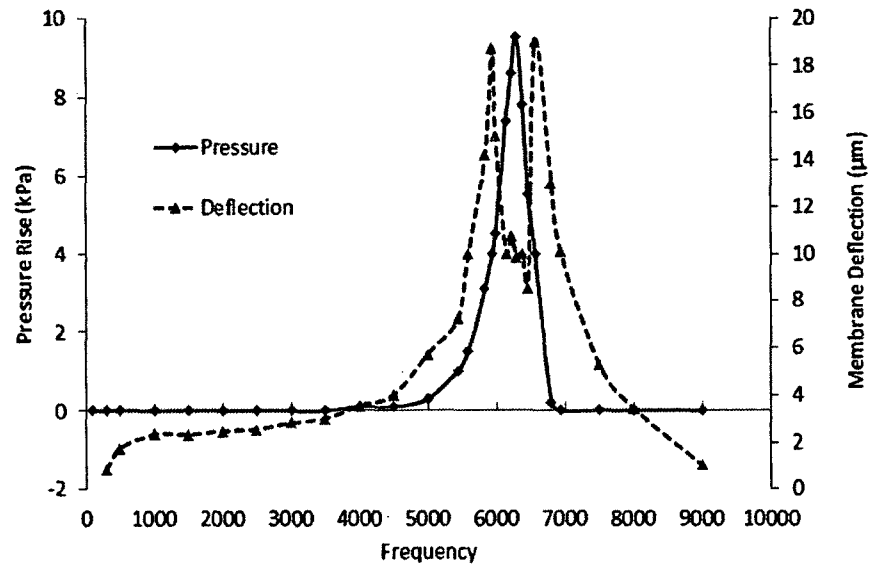


Figure 6-4: Maximum pressure rise occurs at resonant frequency of the piezo diaphragm actuator.

6.3 Two-Stage Microcompressor Test Results

Characterization of the two-stage microcompressor follows the same test method as the single stage. The first characterization test for the two-stage device was carried out measuring the pressure-flow performance curve shown in **Figure 6-2** using the test setup in **Figure 6-1**. The test was carried out with the two-stage device driven at the maximum input voltage of the diaphragm, at $V_{pp} = 60$ V, and at its resonant frequency. Stage one was first tuned to its maximum pressure rise with the tuning of the voltage frequency. With the first stage, the second stage voltage frequency was tuned to obtain the overall maximum pressure rise of the device. Stage

one was altered again to ensure that the maximum pressure rise is obtained. From the pressure-flow curve in **Figure 6-2**, the two-stage microcompressor developed a maximum pressure rise of 18 kPa, achieving twice the pressure rise of the single stage. At maximum flow, with no back pressure, the two-stage device produced a same maximum flow rate of 32 sccm to that of the single-stage device.

The second characterization test conducted was a frequency sweep of the two-stage device by measuring the response of the generated pressure rise and the diaphragm deflection. In the first part of the frequency sweep test, each stage was driven separately, with the other stage turned off to measure the pressure generated and diaphragm deflection. **Figure 6-5** and **Figure 6-6** show the measured result of the pressure rise and deflection in each stage in response to the drive frequency.

Comparing the two figures, stage 2 in **Figure 6-6** exhibited a maximum pressure rise of 9.8 kPa, larger than stage 1 shown in **Figure 6-5**, with only 6.6 kPa. The deflection of the diaphragm in stage 2 followed the same pattern as that of the single-stage microcompressor; where the diaphragm deflection decreases at the maximum pressure rise. Stage 1 does not follow this similar trend, where diaphragm deflection has no local minimum when generating large pressure rise. This is likely due to the extra dead volume at the interconnection chamber that exist between the stage 1 outlet and stage 2 inlet port. The interconnection chamber becomes an extension of stage 1; therefore, extra dead volume reduces the pressure rise in stage 1. Due to the pressure rise in stage 1 being at minimal (6 kPa), the diaphragm can still maintain its large deflection.

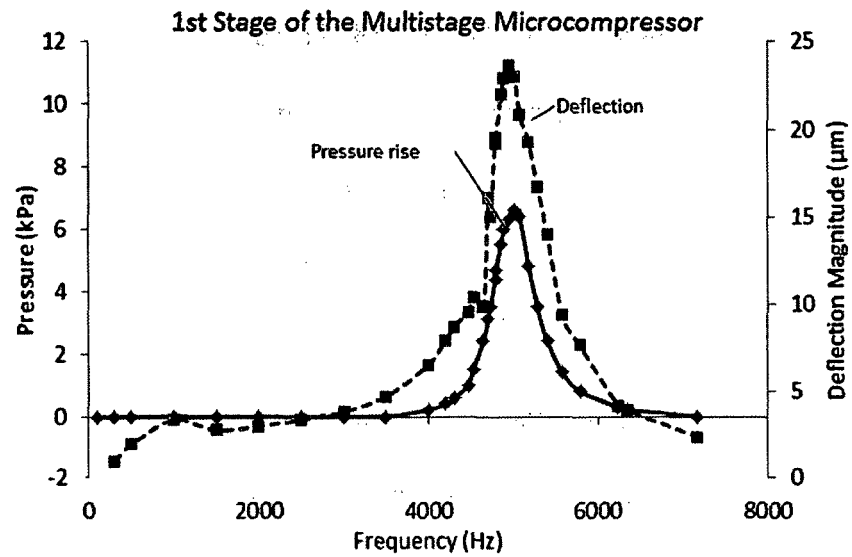


Figure 6-5: Stage 1 of the two-stage microcompressor device frequency.

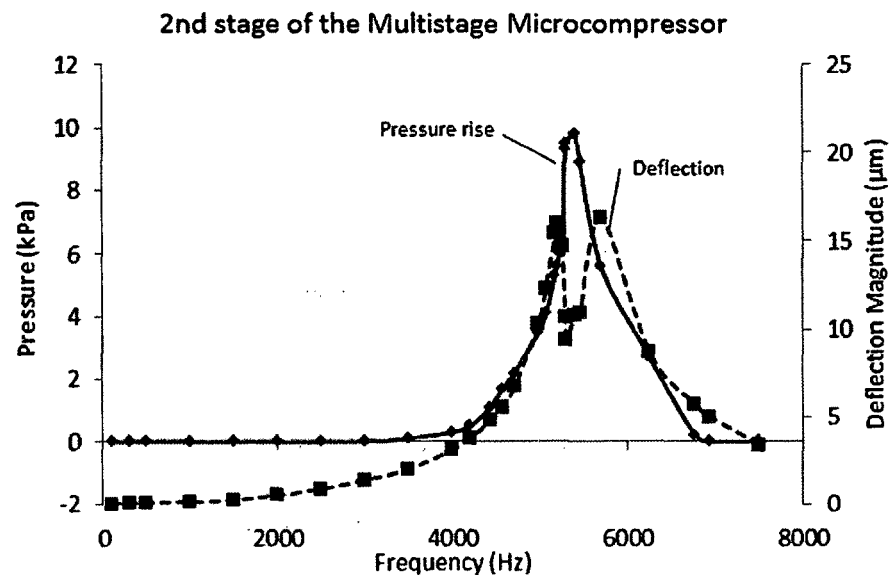


Figure 6-6: Stage 2 of the two-stage microcompressor device frequency response.

The second part of the characterization test is shown in **Figure 6-7**; it shows the frequencies sweep of the two-stage operating in combination to generate pressure rises. This was conducted by first determining that the best combination frequencies

were 4.8 kHz and 5.26 kHz for stages 1 and 2, respectively. To obtain the two frequency sweep curves in **Figure 6-7**, each stage was fixed to its peak frequency while the other stage drive frequencies were swept from 0-8 kHz. It can be noted that stage 1 shifted from 5.0 kHz to 4.8 kHz, and stage 2 shifted from 5.4 kHz to 5.26 kHz from the test in **Figure 6-5** to **Figure 6-6**, respectively. Thus, when operating together, the multistage has a combination of frequencies which may produce its own system resonance as a multistage.

Interestingly, there is another local point (A) in **Figure 6-7** that shows a local point of system resonance in the multistage device. This occurs at point A when the frequency in stage 1 was fixed at 4.8 kHz while the frequency in stage 2 was tuned to 2 kHz. System resonance can occur in this tuning sequence since stage 1 is operating at high frequency, and since it is producing the pressure in the system, it becomes the dominant stage and controls the opening of all the valves, under the condition that stage 2 is operating at low frequency. As the frequency in stage 2 increases beyond 0 Hz, it aides stage 1 in the pressure output, and once it reaches 2 kHz, there is a system resonance that occurs generating a local pressure rise.

Moreover, this local peak does not exist when conducted vice versa as seen with the top curve in **Figure 6-7**. It is concluded that when stage 2 is operating at a fixed frequency of 5.26 kHz, it becomes the dominant stage from the large pressure it generates. Thus, stage 2 is in control of its inlet check valves preventing any reverse flow or reverse pressure back into stage 1. Stage 2 behaved as it is operating independently of stage 1, as long as stage 1 frequency is below its resonant frequency

Therefore, this can be viewed as stage 2 being decoupled from stage 1, preventing any system resonance from happening.

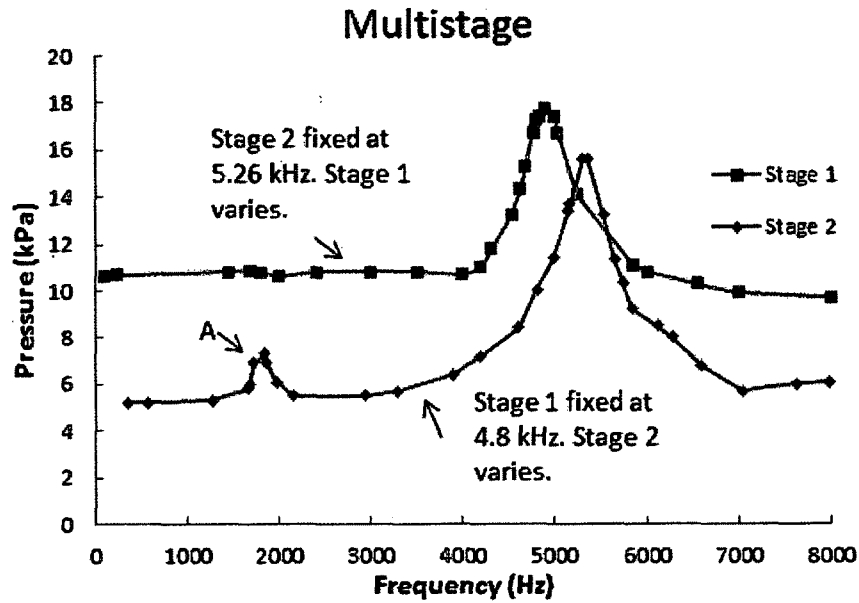


Figure 6-7: Frequency sweep of the two-stage microcompressor.

6.4 Microcompressor Efficiency

The efficiency of the microcompressor can be calculated by first determining the power consumption of the piezoelectric diaphragm. AC voltage and current are supplied to the piezoelectric diaphragm. The power consumption of the piezoelectric actuator is [119] determined as

$$P = \frac{1}{T} \int_0^T V(t)I(t)dt. \quad \text{Eq. 6-1}$$

The average power consumption is

$$P_{piezo} = I_{rms}V_{rms}\cos(\theta) \quad \text{Eq. 6-2}$$

where I_{rms} , V_{rms} is the the root mean square of the current and voltage peak, and θ is the phase shift between the current and the voltage. The peak current and voltage is measured using a voltage probe and current probe connected to a Tektronic oscilloscope and converted to its root mean square (rms) value.

The power output from the microcompressor is given as [21]

$$P_{comp} = \Delta P \frac{\dot{m}}{\rho} \quad \text{Eq. 6-3}$$

The efficiency of the compressor is given as

$$\eta = \frac{P_{comp}}{P_{piezo}} \quad \text{Eq. 6-4}$$

The compressor's efficiencies at various back pressure in **Figure 6-8** shows a maximum efficiency of 0.55% and 0.25% for the single-stage and two-stage, respectively. The efficiency of the single-stage showed a comparable value to the compressor developed by Yoon *et al.* [21] with 0.12%. Although the two-stage has two actuators requiring more electric power to the piezoelectric diaphragm, the two-stage is driven at lower resonance frequencies than the single-stage. Thus, with the lower power consumption and larger pressure rise, the efficiency of the two-stage is better than the single-stage.

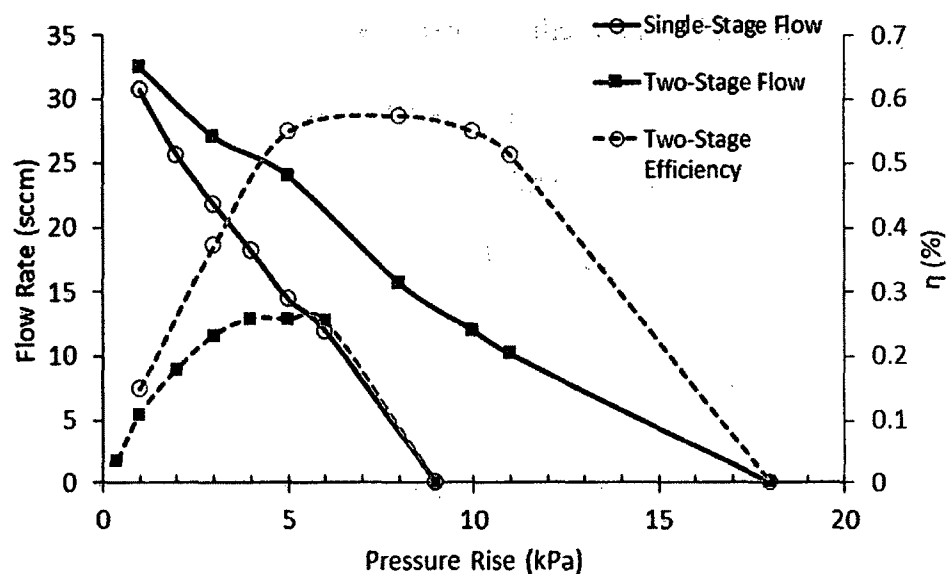


Figure 6-8: Measured pressure-flow performances and compressor efficiencies of the single-stage and two-stage microcompressors.

6.5 Conclusion

This chapter covered the experimental test result of the fabricated single-stage and two-stage microcompressor. Using the single-stage as a baseline comparison, the two-stage microcompressor device was proven successful as it generated twice the pressure rise of the single-stage. The characterization tests were carried out at its maximum driving parameters, with 60 V_{pp} to the piezoelectric diaphragm and at its resonant frequency to determine the pressure-flow performance. The test shows that the single-stage and the two-stage device can generate a maximum pressure rise of 9.5 kPa and 18 kPa, and a maximum flow rate of 32 sccm using air as the gas medium. Frequency sweep characterization of both devices showed that the developed piezoelectric microcompressors need to operate at a high resonant frequency close to or at the diaphragm resonance to achieve maximum performance output.

The interconnect volume that exists between stage 1 and stage 2 of the two-stage device is considered as extra dead volume in stage 1, which resulted in lowering the pressure rise of stage 1. Overall, piezoelectric unimorph diaphragm with passive microvalves configured in a series was proven successful in increasing the pressure rise of the overall multistage device at a high resonant frequency.

CHAPTER 7

SUMMARY, CONCLUSIONS, AND FUTURE WORK

This chapter summarizes the findings and major points of this dissertation. Additionally, dissertation motivation and objectives are summarized. The conclusions are based on the major points from the literature review in Chapter 2, the piezoelectric diaphragm and microvalves study in Chapter 3, the single and multistage microcompressor modeling and simulation in Chapter 4, the fabrication of the single and two-stage microcompressor in Chapter 5, and characterization results of the fabricated devices in Chapter 6.

7.1 Summary

The motivation of this dissertation was to investigate a multistage microcompressor utilizing passive microvalves to drive a micro vapor compression system and use with other micro gas applications. The primary objective was to develop an initial conceptual experimental device which can demonstrate the effectiveness of using a multistage micro gas compressor with micro components. The second objective was to develop support studies to further the understanding, characterization, development, and optimization of the device.

Chapter 2 provided a review of the mechanical compression micropump to understand its limitations and challenges in incorporating it to a micro cooler such as a Joule-Thomson system. The current requirement from a Joule-Thomson requires a 4:1

pressure ratio with a maximum output of 0.4 MPa from the microcompressor. For a microscale device, this needs not only a high performance microactuator, but also microvalves which can provide a good seal from reverse leakage at high pressure, and enclosed chamber materials that can withstand large back pressure at the microscale level. Out of the different microactuators reviewed in Chapter 2, stack piezoelectric actuator with a flexure structure has successfully satisfied this requirement. Piezo-hydraulic is another promising microactuator that can help overcome the limited displacement from a stack piezoelectric actuator. At the microscale level, microactuator provides very limited stroke, and reduction of the dead volume has shown to be effective and more important at the microscale level in increasing the pressure ratio. However, this is not the only challenge, large output force from the microactuator is also needed to overcome the high backpressure of the gas and provide the stroke in the chamber.

Chapter 3 presents a detailed study of the piezoelectric diaphragm and the passive microvalve. A literature review of the different piezoelectric diaphragm configurations, its fabrication methods, synthesis of the piezoelectric material, and geometric design optimization were discussed to provide a means for developing a high performance piezoelectric unimorph diaphragm microactuator. Characterization of the piezoelectric diaphragm was conducted with analytical analysis and FEM, and compared to the experimental results. Input driver voltage, the frequency response of the diaphragm deflection, and pressure load on the diaphragm were characterized and tested.

In the second part of Chapter 3, characterizations of the passive microvalves were carried out. In the first part of the microvalve study, an analytical model of the gas pressure-flow relationship was developed using a fixed microvalve plate structure in a

quasi-steady flow study. This model was also carried out with FEM analysis to determine the loss coefficient in the analytical model. The second model was a flexible valve plate model, which was developed to predict the valve plate response with respect to the flow rate through the valve in a quasi-steady flow. The two analytical models, the fixed valve plate and flexible valve plate were used to explain the experimental result of the pressure-flow relationship. A quasi-steady fluid-structure interaction FEA was also used to compare the results. Lastly, a transient fluid-structure interaction FEA analysis was carried out to observe the response of the microvalve plate height, damping ratio and resonant frequency.

Chapter 4 presents the lumped model simulation of the single and two-stage microcompressor which can provide the dynamic performance of the microcompressor chamber, microvalve dynamics, and the mass dynamics. The model was developed based on the assumption that the stroke volume from the piezo disc is a constant volume independent of the operating frequency. To develop the multistage lumped model simulation, several steps were taken. First, the microvalve fluid-structure lumped model was developed, simulated and validated with the result from the FEA fluid-structure quasi-steady flow analysis. Second, the single-stage lumped model was then developed and simulated based on a lumped model of the compressor and the validated microvalve lumped model. Dynamic results and the pressure-flow rate performance curve were plotted. Lastly, the two-stage simulation model was then developed by arranging two single-stage models in a series. Two different configurations of the two-stage microcompressor simulation were presented. One with no interconnected chamber, and

the second with an interconnected chamber. Drive frequency ratio between stage one and two of the multistage was simulated to observe the pressure rise as well.

Chapter 4 results highlight:

- There exist two types of reverse leakage. Dynamic reverse leakage which exists from the frequency lag of the microvalve structure, and sealed-reverse leakage which exists when gas leaks in the reverse direction when the valve plate is in a closed position.
- Reduction in the microvalve flow rate in the forward direction at high pressure frequency is a result of the attenuation of the microvalve plate height at high frequency. Dynamic reverse leakage contributes to a smaller amount than the plate height attenuation.
- Operating the two-stage microcompressor out of phase provides the best case scenario to achieve high pressure ratio from a simulation standpoint.
- The interconnected volume is considered dead volume to its previous stage, which can result in pressure ratio loss. Therefore, it is critical to minimize dead volume in the design of a multistage device.

Chapter 5 covers the fabrication and assembly of the single-stage and two-stage microcompressor devices. The finalized microcompressors were developed using a mixture of microfabrication process and machining. A pressure-flow performance curve of the single-stage microcompressor was plotted. This curve was compared to the simulation model developed in Chapter 4. A sealed-reverse leakage model of the microvalves was added to the lumped model simulation to compare to the single-stage device.

Chapter 6 presented the characterization of the single- and two-stage devices. Using the single-stage as a baseline performance comparison to the multistage, the pressure-flow curve tests, drive voltage test, and frequency response tests were carried out to evaluate the device's pressure, flow, and diaphragm deflection output. The single-stage and two-stage devices produced a maximum pressure rise of 9.5 kPa and 18 kPa, respectively, with both outputting a max flow rate of 32 sccm driven at its maximum operating condition of 60 V_{pp} and at the resonant frequency (~ 4.8 – 6.3 kHz). Tests from the two-stage device showed that stage one generated less pressure rise than stage two because of the interconnect volume that exists between stage one and stage two, which acts as dead volume for stage one.

7.2 Conclusion

The tested single-stage and two-stage microcompressors were successfully developed with passive microvalves and piezoelectric unimorph disc and were shown to increase gas pressure when arranged in series. The two-stage microcompressor operates with each stage at its own resonant frequency at ~4.5-6.3 kHz and operates independently of one another to achieve a pressure rise of 18 kPa.

7.2.1 Dissertation Contributions

- 1: This multistage device developed in this dissertation has laid the groundwork for developing a true microscale multistage piezoelectric diaphragm micro gas compressor.
2. Passive microvalves and piezoelectric unimorph diaphragm have been modeled and analyzed and are viable components for integration in a multistage device.

3. Lumped modeling of the multistage microcompressor enables the study of microcompressor dynamics and prediction of the overall device performances.
4. A comparison of a fabricated single-stage and a two-stage microcompressor device arranged in a series is shown to improve the overall pressure rise of a microcompressor by utilizing piezoelectric diaphragm and passive microvalves.
 - a. High resonant frequency operation is needed to achieve larger stroke volume to produce larger pressure rise.
 - b. The piezoelectric diaphragm stroke volume generation is limited to higher back pressure. Thus, improvement in a microactuator large force generation is needed to operate at a higher pressure ratio.
 - c. Operation at high frequency generates undesirable acoustic sound from the piezo disc.

7.3 Future Work and Recommendations

The work in this study was intended for the investigation of a multistage microcompressor utilizing micro components that are possible for scaling down to a true microscale size. The requirement for a micro cryogenic cooler using the Joule-Thomson system with a pressure ratio of 4:1 at 0.4 MPa were not achieved with the two-stage microcompressor. However, the result of this dissertation proved that the utilization of multistage chamber in a series with microactuators and passive micro check valves can be promising for future work. Here is a list of identified issues which can further the development of a multistage microcompressor and improve its performance.

7.3.1 Microactuator Improvement

The implementation of the piezoelectric unimorph diaphragm (piezo disc) showed to be promising. However, as shown from the deflection analysis in **Figure 3-10** and the test result in **Figure 6-4**, the membrane can only deflect up to a pressure limit of 30 kPa operating at the resonant frequency with 60 Vpp (**Figure 3-13**). To increase the upper load limit, improvement in the piezoelectric material properties and unimorph layers construction to prevent delamination and breakage at high voltage it needed to yield larger pressure load limits to allow the microcompressor to generate a larger pressure rise.

A promising microactuator to implement is the piezo-hydraulic type described in Section 2.2.4.1. This can be used to amplify the stroke at least 40X from 0.65 μm to 26 μm while still maintaining large enough force generation to overcome the back pressure in the chamber. Improvement in the development of these microactuators in terms of fabrication complexity will yield an improved multistage microcompressor.

7.3.2 Microvalve Improvement

The microvalves in this thesis were developed with SU8 using the microfabrication process, released from the silicon substrate and attached to a recessed valve seat made from machining acrylic. The attachment of the microvalve to the machine housing of the microcompressor leads to a reverse-sealed leak problem. The manual bonding process of the UV adhesive leads to an inconsistent thickness adhesive layer between the valve plate and its seat, leading to some unpredictability in the pressure-flow characterization. The large gap from the adhesive can exist if the operator applies a large amount of UV adhesive during the bonding process.

A more consistent or improved approach in the bonding process may help with these issues. A recommended approach for future work is to leave the microvalve on the silicon substrate and only release the valve plate diameter as shown in **Figure 7-1** using a release layer. The release layer can be materials such as SiO_2 and others that are compatible with the micro fabrication process. The microvalves will have a very thin consistent gap layer for the pressure-flow characterization, and the layer will be thin enough for good reverse seal. The microvalve assembly can be diced from the silicon substrate and integrated directly into the microcompressor housing. Other microvalve material such as silicon, parylene, and polyimide, have been developed with success even at a high back pressure of up to 350 psi [59].

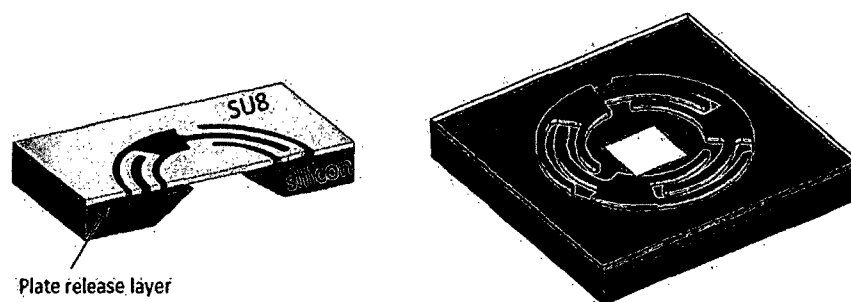


Figure 7-1: Microvalve future recommendation.

7.3.3 Improvement in the Characterization of Microvalve Fluid-Structure Interaction

A quasi-steady equilibrium microvalve model shown in **Eq. 3-26** was developed to predict the valve plate height with respect to the steady air flow through the valve plate orifice. The valve plate height in response to the steady air flow was not measured for model validation due to limitations of the measurement equipment. The LDV was

capable of measuring the dynamic displacement but unable to obtain measurements of the static displacement of the valve plate at steady-state flow equilibrium. Additionally, the SU8 material is a clear material which does not reflect the LDV well enough to obtain measurable signal strength. Metal deposition on the SU8 can improve reflection. However, it changes the microvalve structural stiffness which needs to be accounted. Moreover, the LDV needs to be set up to capture the timing and triggering of the valve plate response. Other measurement methods such as stroboscope interferometry [120] can measure out-of-plane motion using a CCD camera system may address this issue.

7.3.4 Lumped Model Simulation Improvements

The mass flow rate (given in **Eq. 4-12 - Eq. 4-15**) through the microvalve orifice in the lumped model simulation used was based on Bernoulli's equation. In Chapter 2, the pressure-flow through the microvalve orifice given in **Eq. 3-21** was based on the aerostatic thrust bearing flow model [121], [122], also called the radial flow between parallel disks [123], [124]. The simulation lumped model can be designed to use the aerostatic thrust bearing model to replace Bernoulli's equation.

The lumped model simulation used in **Eq. 4-11** for the stroke modeling of the compressor chamber ignored the modeling of the piezoelectric diaphragm and its nonlinearity at the resonance peak and assumed an oscillating volume. The classical laminate plate theory (CLPT) provides a model of the diaphragm deformation for a quasi-static deformation based on the input voltage and pressure load. The magnitude of the center deflection of the diaphragm from the CLPT match closed to the deflection of the experimental test deflection between 500 – 2,500 Hz. The dynamic deflection becomes non-linear at higher frequency range near its resonance. A dynamic model of the

diaphragm may be of interest for the future study of using a diaphragm for the microcompressor, unless the diaphragm compressor is designed to operate at a low frequency

7.3.5 Device Characterization Test Recommendation

Characterization test of the two-stage device was carried out by driving each stage independently at its own resonant frequency to ensure that each diaphragm generates its maximum stroke. In the simulation model, it was predicted that driving each stage out of phase provided the maximum overall pressure rise of the multistage device. Due to the dependency of the diaphragm resonant frequency, validation of this simulation results was not carried out. In future work, a microcontroller is needed to control the timing of each stage to validate further the in-phase and out of phase timing of each stage.

7.3.6 Redesign for a True Microscale Multistage

The microcompressor was designed with components which can be scaled down to microscale sizes using microfabrication methods and MEMS method. Numerous work on micropumps have been developed from silicon and glass substrates. Similar methods can be used to develop a multistage microcompressor device. To achieve a large pressure ratio from a microcompressor for current Joule-Thomson requirement, an alternative to piezoelectric diaphragm is needed because it cannot withstand large pressure loads. Piezo-hydraulic microactuator is a better choice for integration with MEMS technology to develop the next generation of multistage microcompressors.

APPENDIX A
CLASSICAL LAMINATE THEORY WITH MATLAB

The analytical model for the static deflection of the circular piezoelectric unimorph diaphragm is given by Desphande [104] and Lin [125]. The matlab code generates output of the diaphragm profile as shown in **Figure A-1** or it can be modified to output the volume that is displaced by the unimorph diaphragm as a function of input voltage and pressure.

```

clear all; clc;

%% Radius m, thickness of layer
Ri=7.5E-3;    % for Silver, PZT, Silver, Bonding Epoxy,
Ro=10E-3;    % Brass outer, passive layer
tag=0;       % top silver thickness
tpz=.21E-3;  % PZt thickness
tag=0;       % bottom silver thickness (same as top)
tbo=0;       % bonding epoxy
tbr=.21E-3;  % Brass
%%

%% Material properties of layers
Ebr=110E9;   E(1)=Ebr;    %Brass Elastic modulus
vbr=0.27;    v(1)=vbr;    %Poisson' ratio of brass
Ebo=5.17E9;  E(2)=Ebo;    %Bonding epoxy Elastic modulus
vbo=0.3;     v(2)=vbo;    %Poisson' ratio of bonding epoxy
Eag=40E9;    E(3)=Eag;    %Pa unit, silver paste. Elastic modulus
vag=0.35;    v(3)=vag;    %Poisson' ratio of silver
Epz=63E9;    E(4)=Epz;    %PZT Elastic modulus
vpz=0.3;     v(4)=vpz;    %Poisson' ratio of pzt
              E(5)=Eag;    %Silver Elastic modulus
              v(5)=vag;    %silver poisson ratio
d31=175E-12; %C/N

%%

%% thickness of the different layers
zo=-tbr/2;   z(1)=zo;
z1=z0+tbr;   z(2)=z1;
z2=z1+tbo;   z(3)=z2;
z3=z2+tag;   z(4)=z3;
z4=z3+tpz;   z(5)=z4;
z5=z4+tag;   z(6)=z5;
%%

Aint11=0; Bint11=0; Dint11=0; n=5;
Aint12=0; Bint12=0; Dint12=0;
for k=1:5

```

```

Aint11 = Aint11 + E(k)*(z(k+1)-z(k))/(1-v(k)^2)
Aint12 = Aint12 + v(k)*E(k)*(z(k+1)-z(k))/(1-v(k)^2)
Bint11 = Bint11 + 0.5*E(k)*(z(k+1)^2-z(k)^2)/(1-v(k)^2)
Bint12 = Bint12 + 0.5*v(k)*E(k)*(z(k+1)^2-z(k)^2)/(1-v(k)^2)
Dint11 = Dint11 + (1/3)*E(k)*(z(k+1)^3-z(k)^3)/(1-v(k)^2)
Dint12 = Dint12 + (1/3)*v(k)*E(k)*(z(k+1)^3-z(k)^3)/(1-v(k)^2)
end

Aext11=0; Bext11=0; Dext11=0; n=1;
Aext12=0; Bext12=0; Dext12=0;
for k=1:n
    Aext11 = Aext11 + E(k)*(z(k+1)-z(k))/(1-v(k)^2)
    Aext12 = Aext12 + v(k)*E(k)*(z(k+1)-z(k))/(1-v(k)^2)
    Bext11 = Bext11 + 0.5*E(k)*(z(k+1)^2-z(k)^2)/(1-v(k)^2)
    Bext12 = Bext12 + 0.5*v(k)*E(k)*(z(k+1)^2-z(k)^2)/(1-v(k)^2)
    Dext11 = Dext11 + (1/3)*E(k)*(z(k+1)^3-z(k)^3)/(1-v(k)^2)
    Dext12 = Dext12 + (1/3)*v(k)*E(k)*(z(k+1)^3-z(k)^3)/(1-v(k)^2)
end

%% comment out V=200 and P=1 and uncomment both V= sym('V') and
%% P= sym('P') if user want to obtain the expression for the volume
displaced
%% as a function of Voltage V, and Pressure, P
% V=200          % temporarily assign V, voltage input  Create a function
variable for this
%P=1            % temporary assignment of pressure
V= sym('V')    % create a variable for V
P= sym('P')    % create a variable for P

Npr=(1+vpz)*Epz*V*d31*(z(5)-z(4)) / ((1-vpz^2)*tpz)
Mpr=0.5*(1+vpz)*Epz*V*d31*(z(5)^2-z(4)^2) / ((1-vpz^2)*tpz)

A = [Ro^2 log(Ro) 1 0 0 0 0 0
     2*Ro 1/Ro    0 0 0 0 0 0
     0 0          0 Ro 1/Ro 0 0 0
     Ri^2 log(Ri) 1 0 0 -Ri^2 -1 0
     2*Ri 1/Ri 0 0 0 -2*Ri 0 0
     0 0 0 Ri 1/Ri 0 0 -Ri
     -2*(Dext11+Dext12) (Dext11-Dext12)/Ri^2 0 (Bext11+Bext12) -
(Bext11-Bext12)/Ri^2 2*(Dint11+Dint12) 0 -(Bint11+Bint12)
     2*(Bext11+Bext12) -(Bext11-Bext12)/Ri^2 0 -(Aext11+Aext12)
(Aext11-Aext12)/Ri^2 -2*(Bint11+Bint12) 0 (Aint11+Aint12)]

D= [-(1/64)*(Aext11*Ro^4*P)/(Aext11*Dext11-Bext11^2)
    -(1/16)*(Aext11*Ro^3*P)/(Aext11*Dext11-Bext11^2)
    -(1/16)*(Bext11*Ro^3*P)/(Aext11*Dext11-Bext11^2)
    -(1/64)*(Aext11/(Aext11*Dext11-Bext11^2) - Aint11/(Aint11*Dint11-
Bint11^2))*(Ri^4)*P
    -(1/16)*(Aext11/(Aext11*Dext11-Bext11^2) - Aint11/(Aint11*Dint11-
Bint11^2))*Ri^3*P

```

```

- (1/16) * (Bext11 / (Aext11 * Dext11 - Bext11^2) - Bint11 / (Aint11 * Dint11 -
Bint11^2)) * Ri^3 * P
- Mpr + (1/16) * ((Aext11 * Dext12 - Bext11 * Bext12) / (Aext11 * Dext11 - Bext11^2)
- (Aint11 * Dint12 - Bint11 * Bint12) / (Aint11 * Dint11 - Bint11^2)) * Ri^2 * P
Npr - (1/16) * ((Aext11 * Bext12 - Aext12 * Bext11) / (Aext11 * Dext11 - Bext11^2)
- (Aint11 * Bint12 - Aint12 * Bint11) / (Aint11 * Dint11 - Bint11^2)) * Ri^2 * P]

C=A\D
vpa(C, 10)

k=200
ri=[0:Ri/k:Ri]
ro=[Ri:(Ro-Ri)/k:Ro]

wintr= (1/64) * Aint11 * ri.^4 * P / (Aint11 * Dint11 - Bint11^2) + C(6) * ri.^2 +
C(7)
wextr= (1/64) * Aext11 * ro.^4 * P / (Aext11 * Dext11 - Bext11^2) + C(1) * ro.^2 +
C(2) * log(ro) + C(3)
wintr=vpa(wintr, 5)

w=[wintr, wextr]
r=[ri, ro]
w=[fliplr(w), w]
r=[-fliplr(r), r]

plot(ri, wintr, ro, wextr)
figure(2)
plot(r, w)

%this display the volume displacement equation. Uncomment the variable
%V and P sym(V) above as variable to display it as variables.
vdisp=(1/192) * pi * P * ( (Aint11 * Ri^6 / (Aint11 * Dint11 - Bint11^2)) +
(Aext11 * (Ro^6 - Ri^6) / (Aext11 * Dext11 - Bext11^2)))
+ .5 * pi * C(1) * (Ro^4 - Ri^4) + pi * C(2) * ( (log(Ro) - 5) * Ro^2 - (log(Ri)
- .5) * Ri^2)
+ pi * C(3) * (Ro^2 - Ri^2) + .5 * pi * C(6) * Ri^4 + pi * C(7) * Ri^2

vpa(vdisp, 10)

```

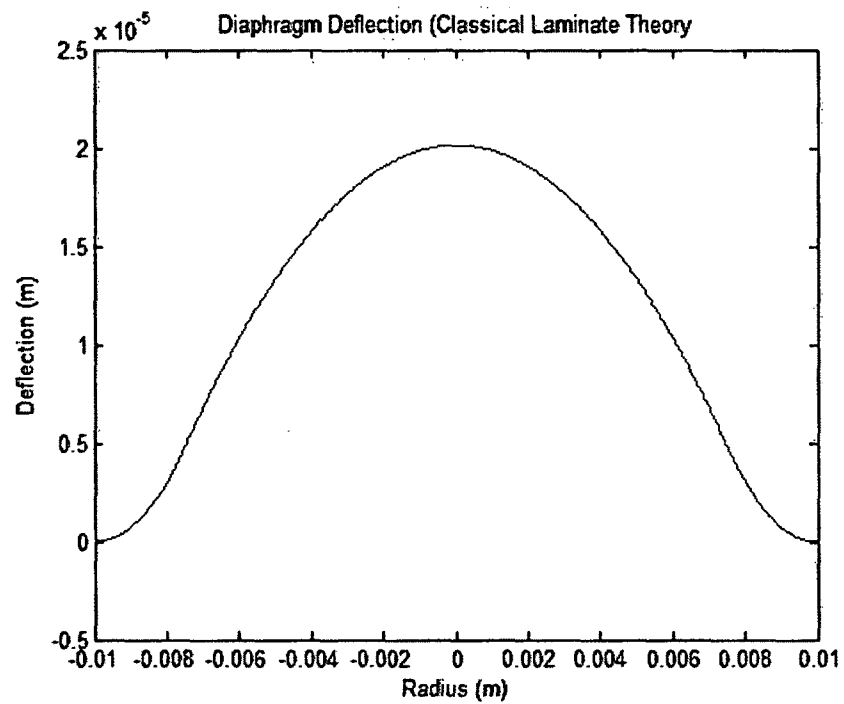
Matlab Output

Figure A-1: Deflection profile of the piezoelectric diaphragm actuator from the Matlab source code using the CLPT method.

APPENDIX B
MICROCOMPRESSOR SIMULINK MODEL

B.1 Single-Stage Microcompressor Simulink Model

The following is lumped model Simulink model to simulate the single-stage microcompressor. The Matlab m-file is the variables values for the lumped model needed for the single-stage and two-stage simulation.

```

clc; clear all;
% This section calculate the Reynolds number

dinlet = 0.5e-3;      %diameter of the inlet port. meter
mu      = 1.983e-5;   % dynamica viscosity of air

% this plot the flow pressure curve for the orficie only

rhoair = 1.225; % kg/m^3
patm   = 101325; % Pa
Cd = 0.7; % flow coefficient
Ao1 = pi*(dinlet)^2/4 % cross sectional area of the entrance orifice
rvalve = 0.4e-3 % radius for surface valve
zv = 100e-6 % height for opening of the vavlve
Ao2 = 2*pi*rvalve*zv; % area for the opening of the valve
Aosurf = 2.01e-6; % m^2, surface area of the valve face
k = 473; % N/m
volvalve = 6249e-9 % m^3 volume of the valve
rhosu8 = 1145 % kg/m^3 density of su8
massvalve = rhosu8*volvalve; % mass of the valve
Vd = 1.0e-8; % m^3 dead volume
Vs = 3.0e-9; % m^3 stroke volume
Vdinit=Vd;
Vsinit=Vs;
n=1.401 % polytropic constant for air
constant = 101e3/(rhoair^n)

```

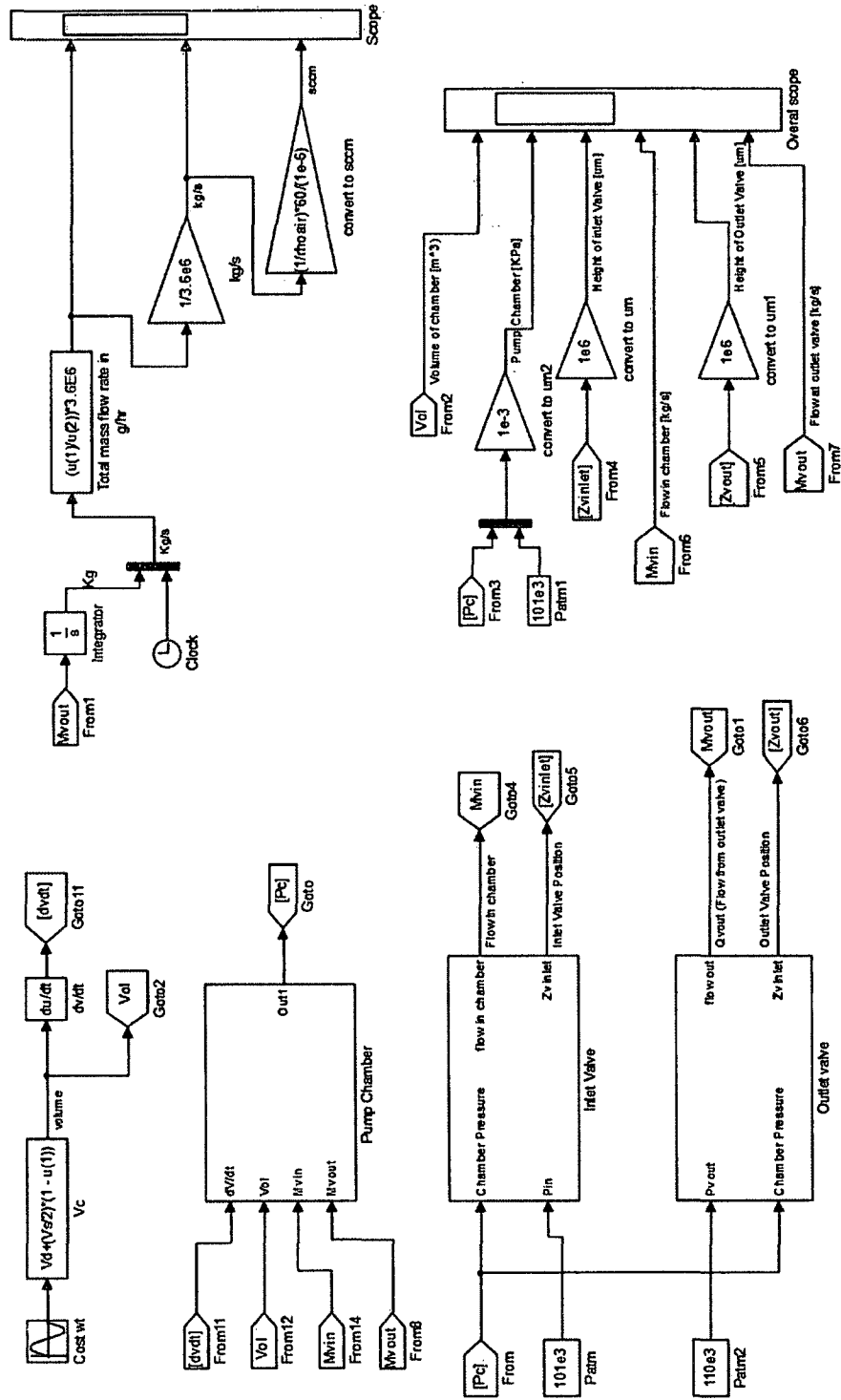


Figure B-1: Single-stage top level Simulink model.

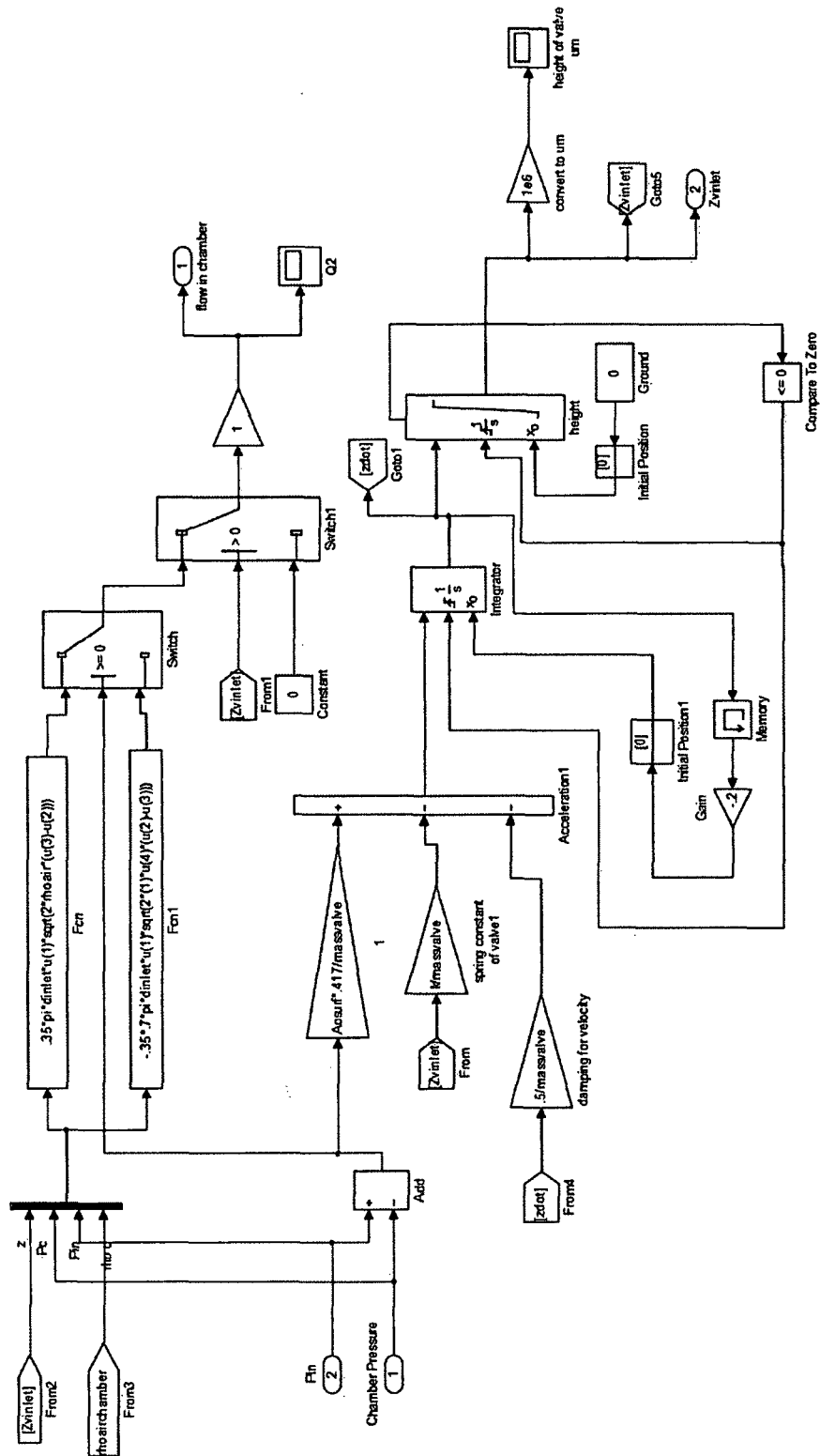


Figure B-2: Single-stage inlet microvalve sub-level model.

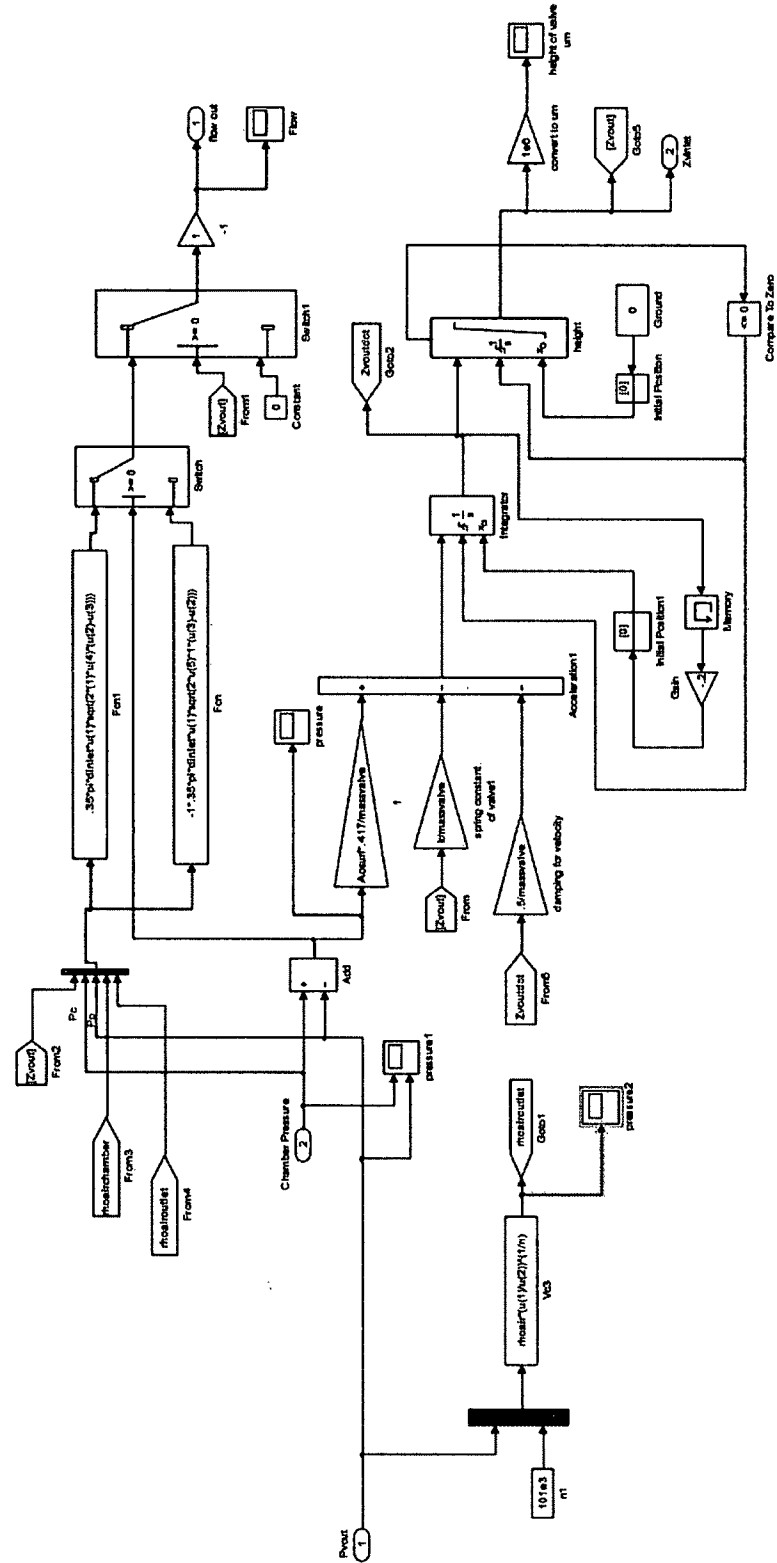


Figure B-3: Single-stage outlet microvalve Simulink sub-level model.

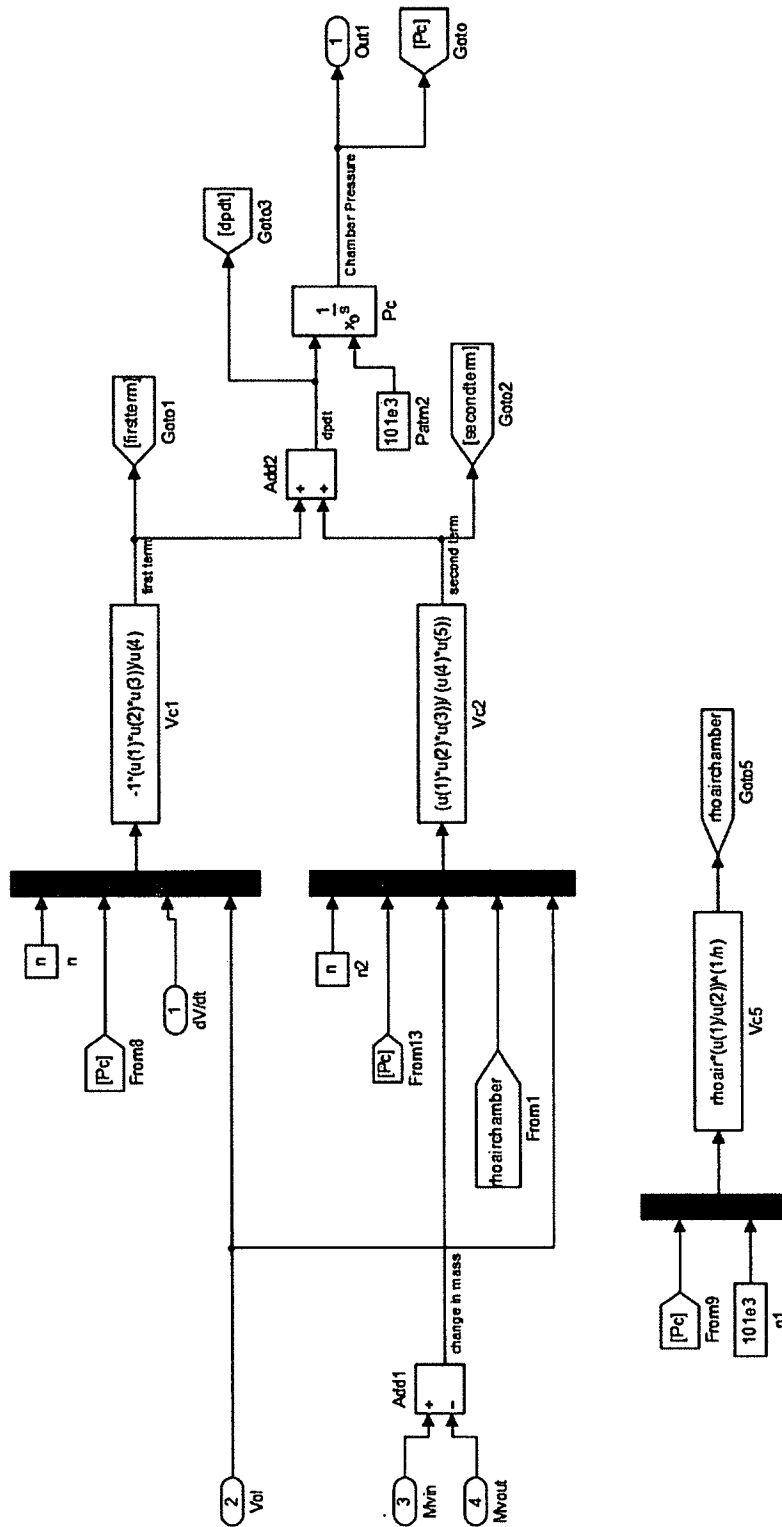


Figure B-4: Single-stage outlet microvalve Simulink sub-level model.

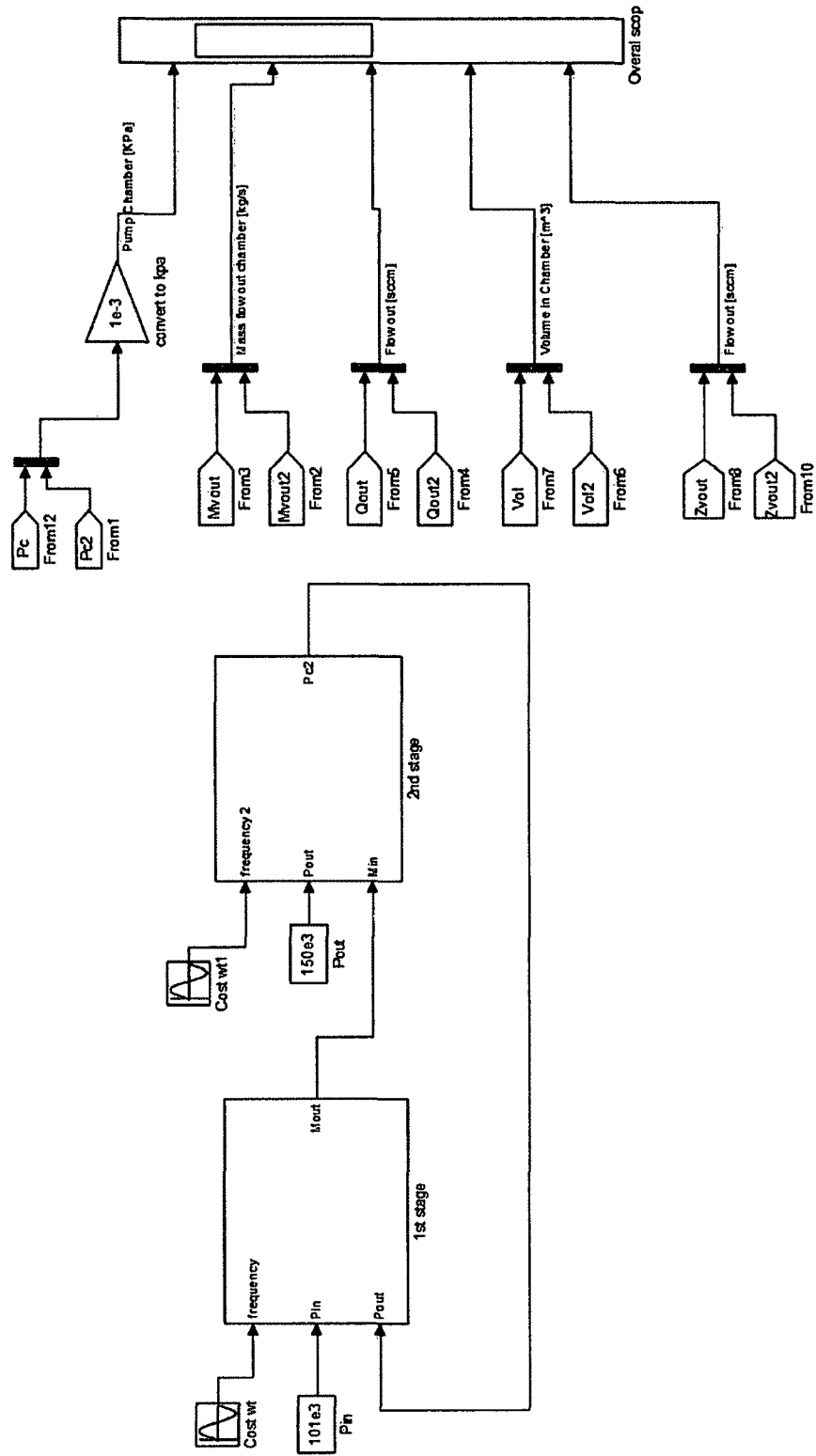


Figure B-5: Two-stage microcompressor Simulink top level model.

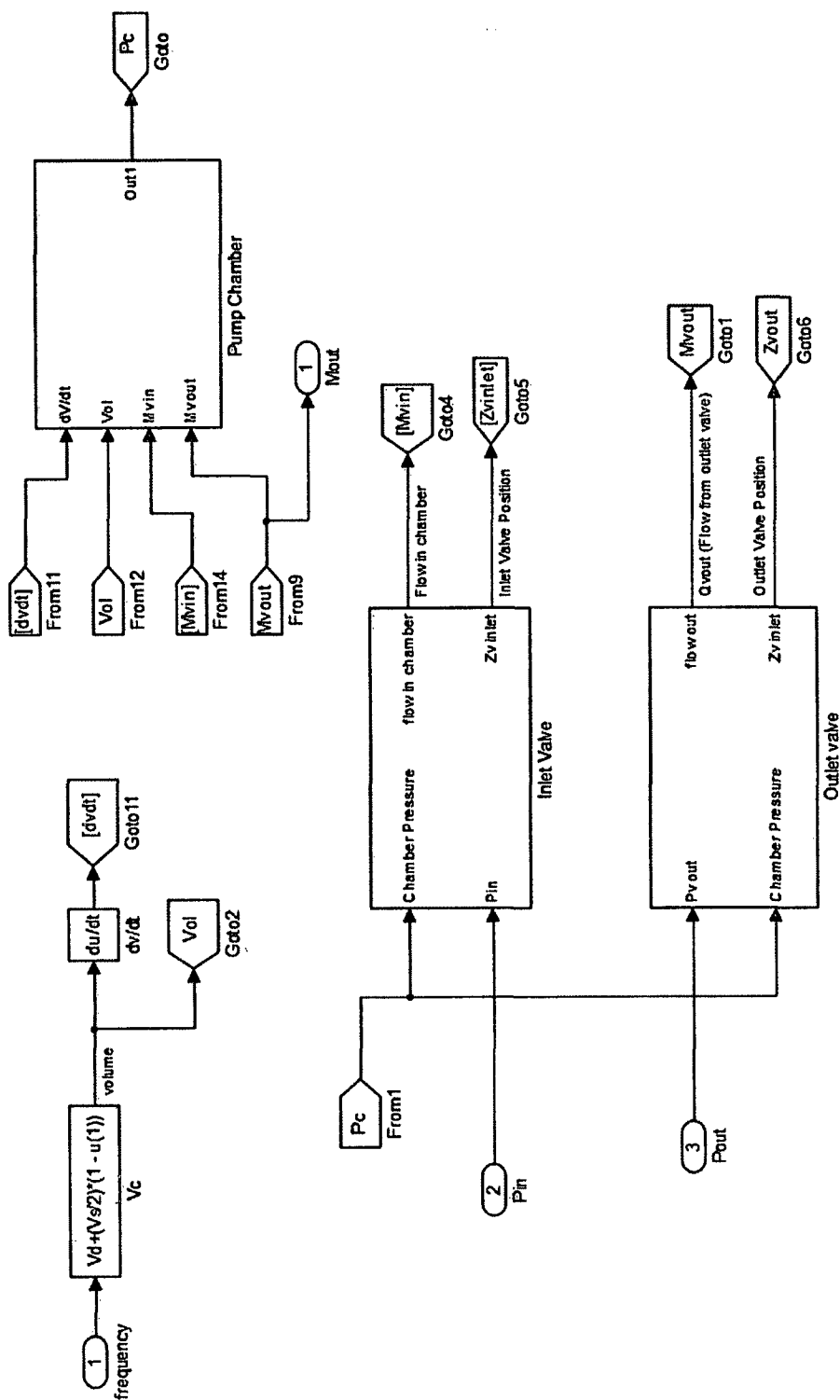


Figure B-6: 1st Stage Simulink model sub-level model of the two-stage model.

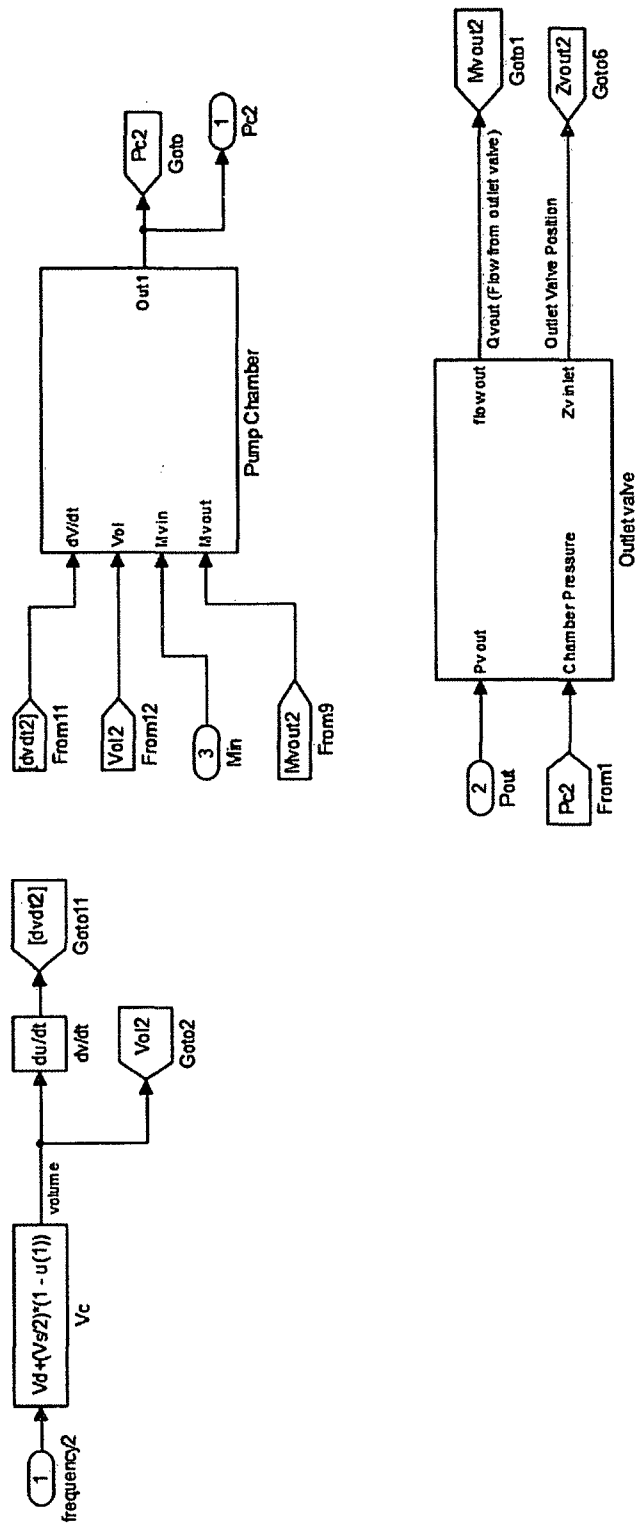


Figure B-7: 2nd Stage Simulink model sub-level model of the two-stage model.

APPENDIX C
MICROCOMPRESSOR DESIGN DRAWINGS



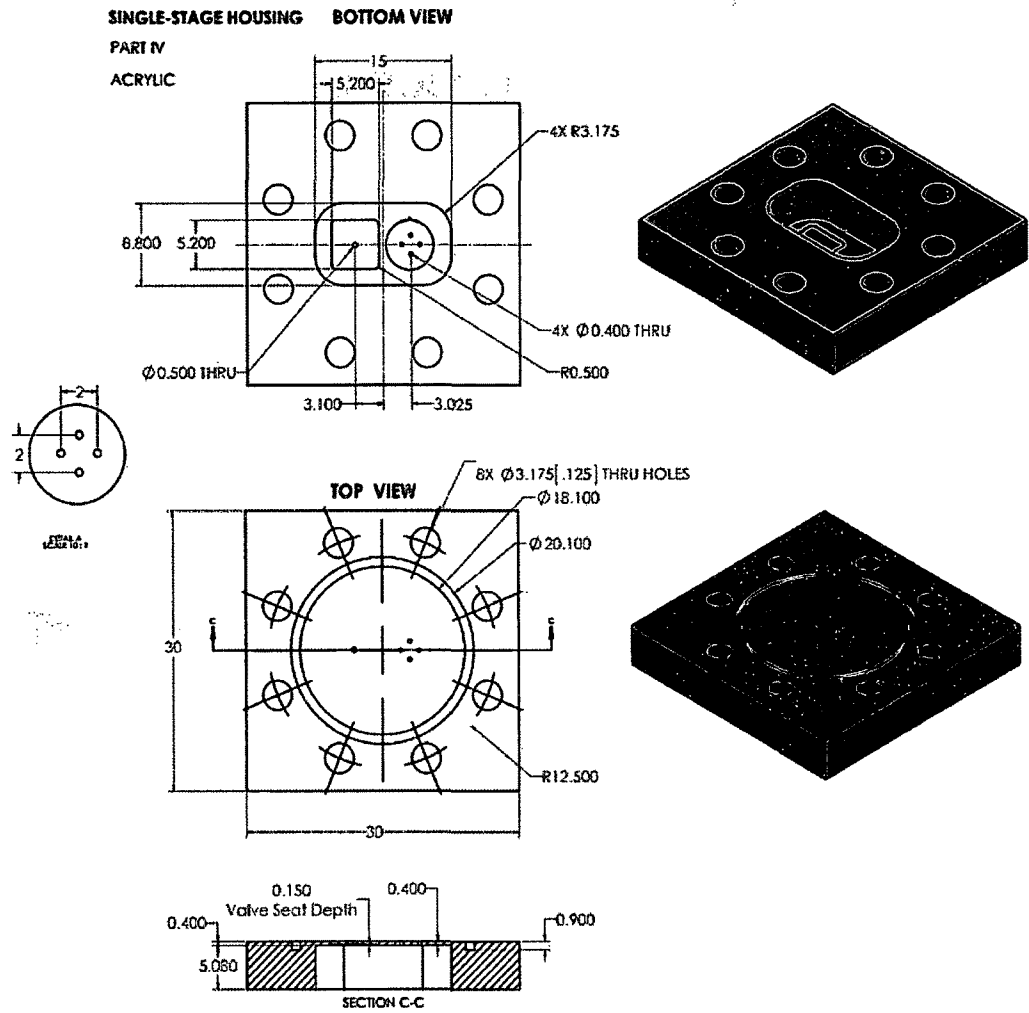


Figure C-1: Housing body of single-stage microcompressor, Part IV

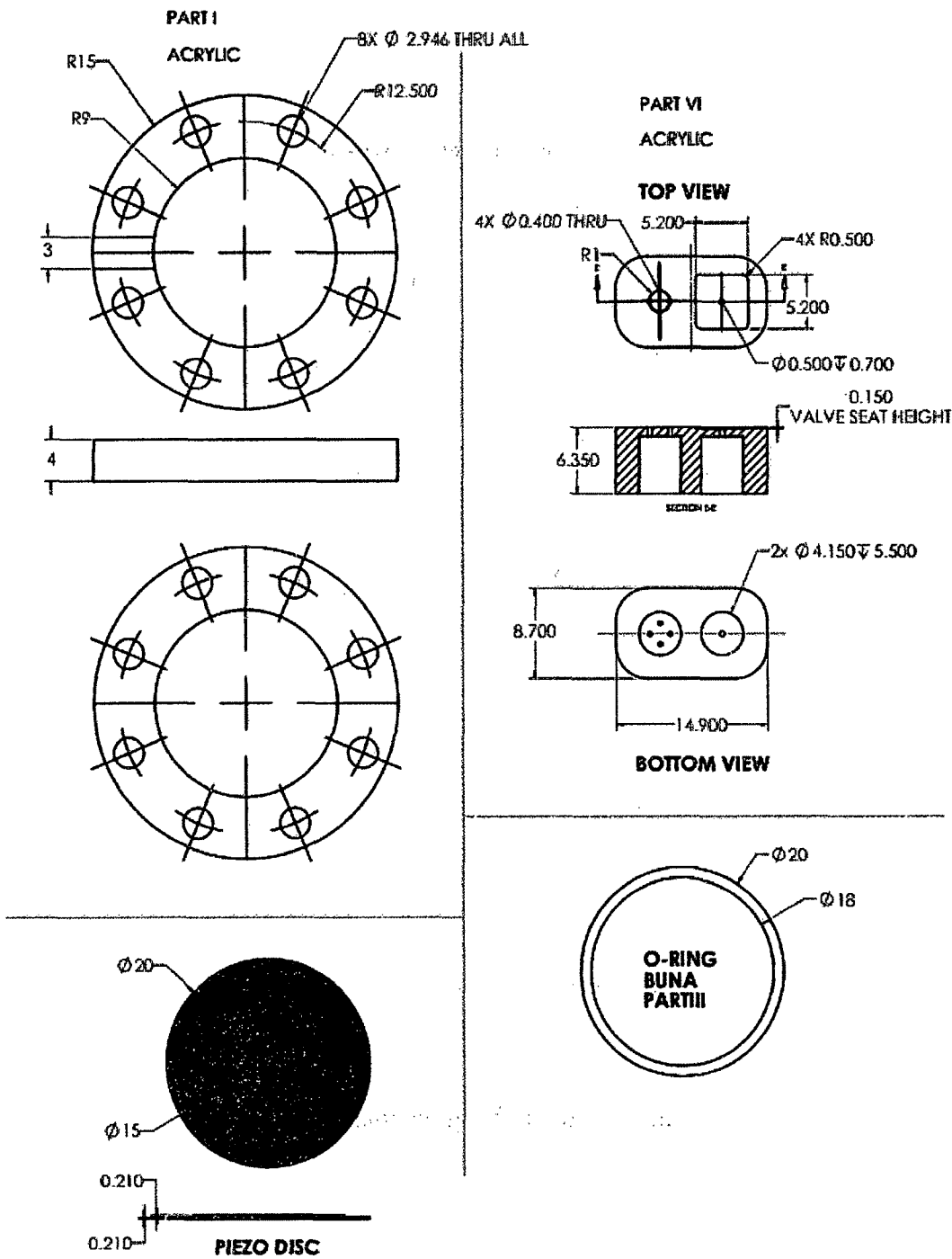


Figure C-2: Dimensions of single-stage microcompressor for part I, part VI, piezo disc and O-ring.

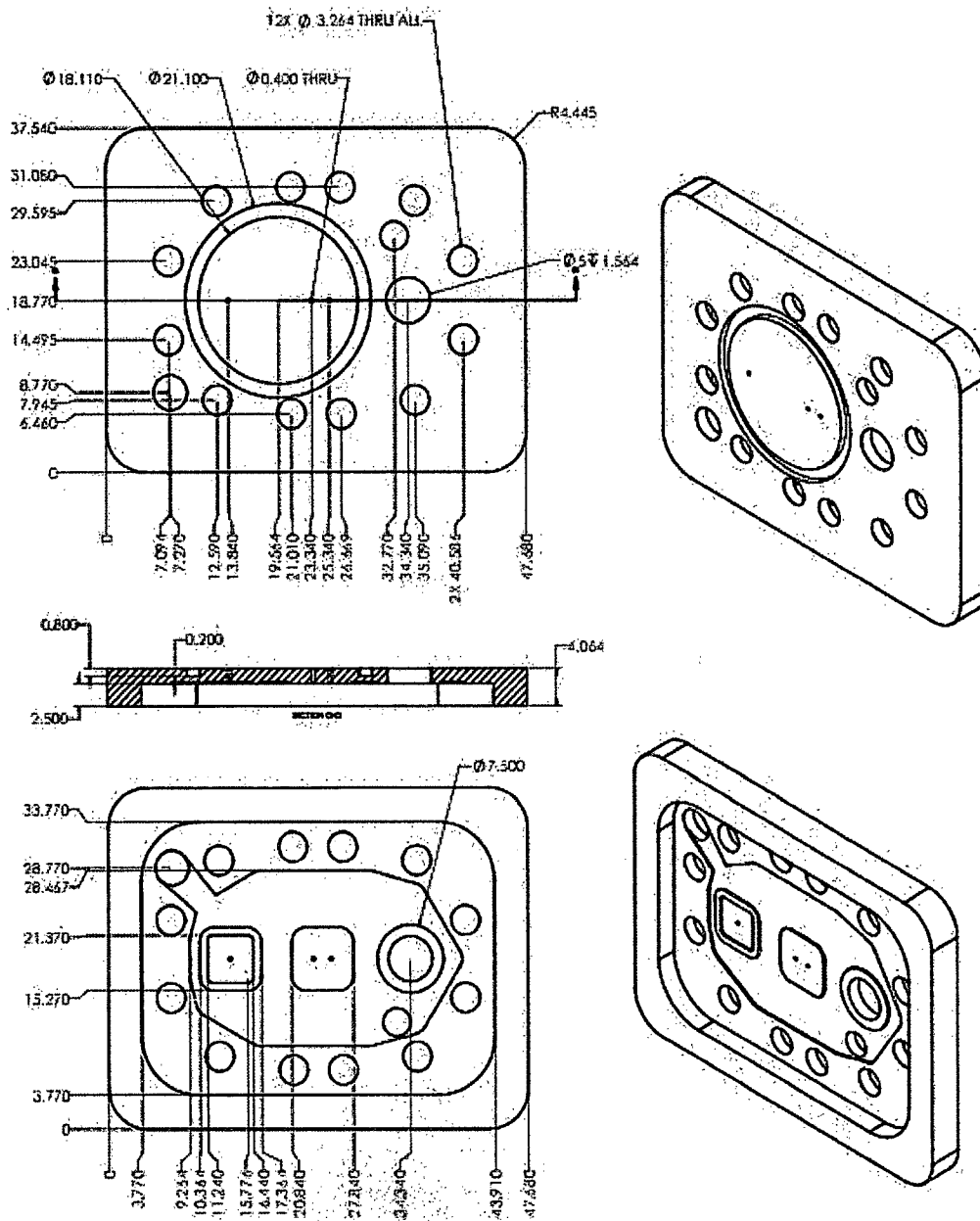


Figure C-3: Bottom housing of 2-stage microcompressor, body 3.

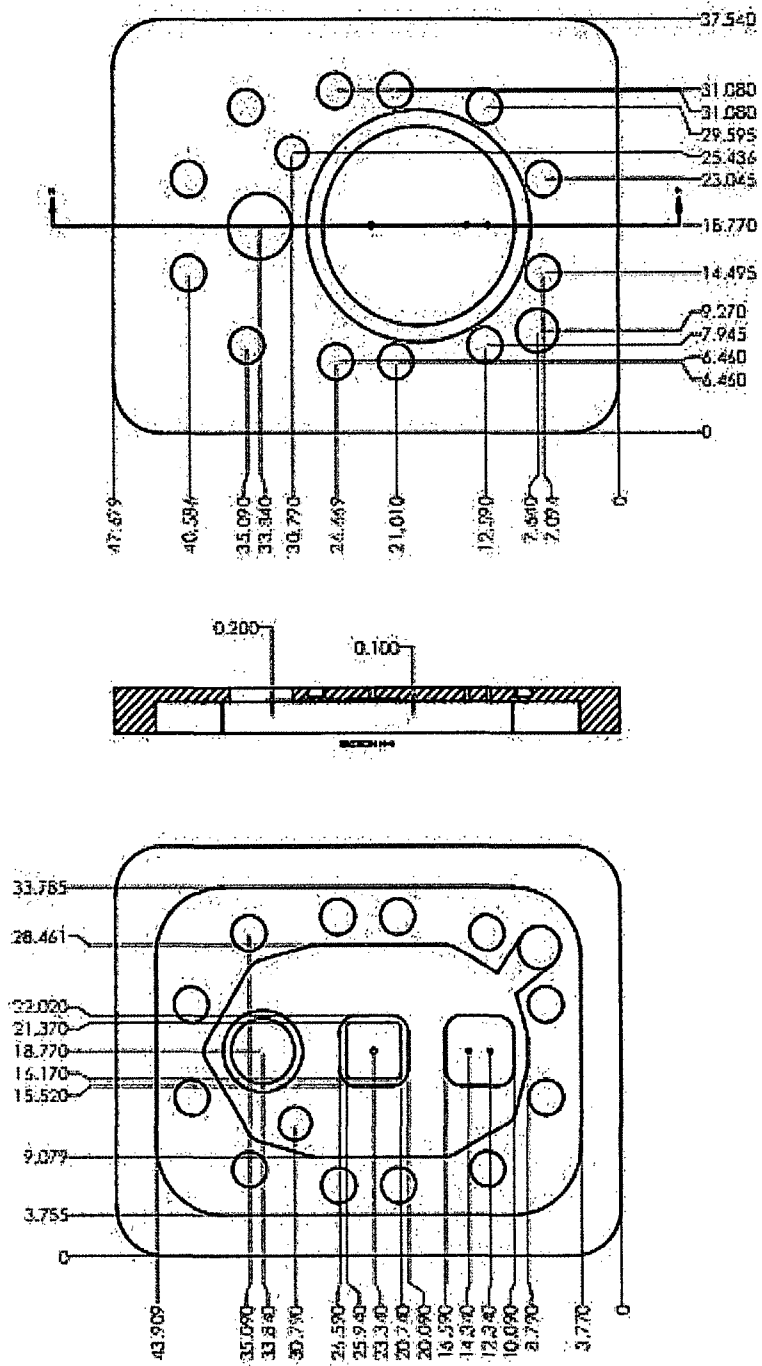


Figure C-4: Top housing of 2-stage microcompressor, body 1.

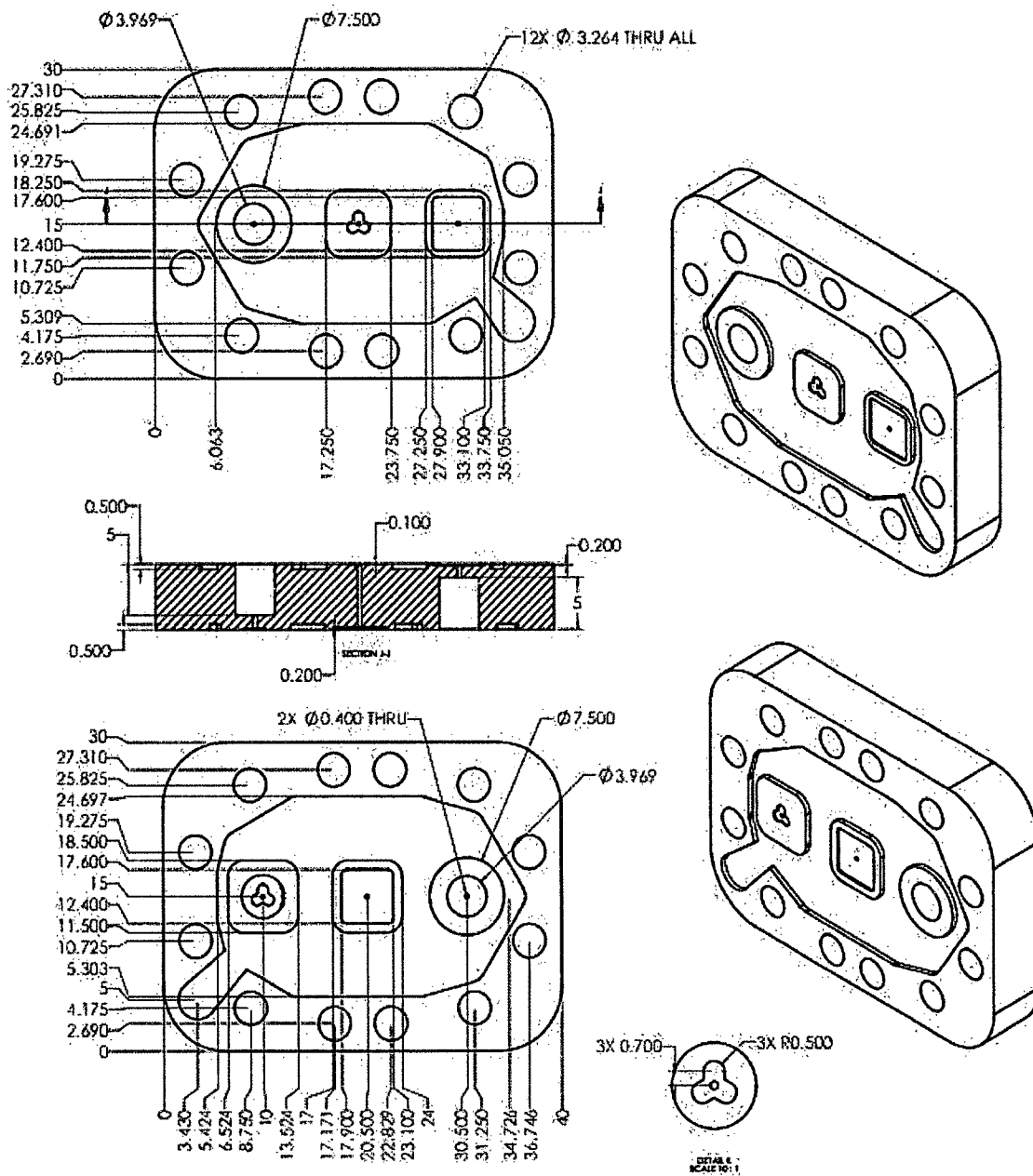


Figure C-5: Middle housing of 2-stage microcompressor, body 2.

BIBLIOGRAPHY

- [1] H. T. G. van Lintel, F. C. M. van De Pol, and S. Bouwstra, "A piezoelectric micropump based on micromachining of silicon," *Sensors and Actuators*, vol. 15, no. 2, pp. 153–167, 1988.
- [2] R. Linnemann and et al, "A self-priming and bubble-tolerant piezoelectric silicon micropump for liquids and gases," *Proceedings MEMS 98. IEEE. Eleventh Annual International Workshop on Micro Electro Mechanical Systems. An Investigation of Micro Structures, Sensors, Actuators, Machines and Systems (Cat. No.98CH36176)*, pp. 532–537, 1998.
- [3] N. K. Gupta, S. An, and Y. B. Gianchandani, "A monolithic 48-stage Si-micromachined Knudsen pump for high compression ratios," in *Proceedings of the IEEE International Conference on Micro Electro Mechanical Systems (MEMS)*, pp. 152–155, 2012.
- [4] E. Stemme and G. Stemme, "A valveless diffuser/nozzle-based fluid pump," *Sensors and Actuators A Physical*, vol. 39, no. 2, pp. 159–167, November 1993.
- [5] G.-H. Feng and E. S. Kim, "Micropump based on PZT unimorph and one-way parylene valves," *Journal of Micromechanics and Microengineering*, vol. 14, no. 4, pp. 429–435, April 2004.
- [6] H. Q. Li, D. C. Roberts, J. L. J. Steyn, K. T. K. Turner, J. A. J. Carretero, O. Yaglioglu, Y.-H. Y. Su, L. Saggere, N. W. Hagood, L. Spearing, S. Spearing, and others, "A High Frequency High Flow Rate Piezoelectrically Driven MEMS Micropump," in *Solid-State Sensor and Actuator Workshop*, pp. 69–72, June 2000.
- [7] K.-P. Kamper, J. Dopfer, W. Ehrfeld, and S. Oberbeck, "A self-filling low-cost membrane micropump," *Proceedings MEMS 98. IEEE. Eleventh Annual International Workshop on Micro Electro Mechanical Systems. An Investigation of Micro Structures, Sensors, Actuators, Machines and Systems (Cat. No.98CH36176)*, 1998.
- [8] H. Zhou, H. Q. Li, V. Sharma, and M. A. Schmidt, "A single-stage micromachined vacuum pump achieving 164 torr absolute pressure," in *Proceeding IEEE International Conference on Micro Electro Mechanical Systems (MEMS)*, pp. 1095–1098, 2011.

- [9] H. K. Ma, W. F. Luo, and H. C. Su, "Development of one-side actuating liquid cooling diaphragm micropump for a multimedia system," *2011 International Conference on Multimedia Technology*, pp. 6307–6310, July 2011.
- [10] M. Koch, N. Harris, A. G. R. Evans, N. M. White, and A. Brunnschweiler, "A novel micromachined pump based on thick-film piezoelectric actuation," *Sensors Actuators A: Physical*, vol. 70, no. 1–2, pp. 98–103, October 1998.
- [11] T.-Q. Truong and N.-T. Nguyen, "A polymeric piezoelectric micropump based on lamination technology," *Journal of Micromechanics Microengineering*, vol. 14, no. 4, pp. 632–638, April 2004.
- [12] J. Han, J. Yeom, G. Mensing, B. Flachsbarth, and M. a Shannon, "Characteristics of electrostatic gas micro-pump with integrated polyimide passive valves," *Journal of Micromechanics and Microengineering*, vol. 22, no. 9, p. 95007, September 2012.
- [13] T. T. Veenstra, J. W. Berenschot, J. G. E. Gardeniers, R. G. P. Sanders, M. C. Elwenspoek, and a. van den Berg, "Use of Selective Anodic Bonding to Create Micropump Chambers with Virtually No Dead Volume," *Journal of Electrochemical Society*, vol. 148, no. 2, p. G68, 2001.
- [14] T. Gerlach, "Pumping gases by a silicon micro pump with dynamic passive valves," *Proceeding of International Solid State Sensors Actuators Conference (Transducers '97)*, vol. 1, pp. 357–360, 1997.
- [15] A. Olsson, G. Stemme, and E. Stemme, "A numerical design study of the valveless diffuser pump using a lumped-mass model," *Journal of Micromechanics Microengineering*, vol. 9, no. 1, pp. 34–44, March 1999.
- [16] A. Olsson and E. Al., "A valve-less planar fluid pump with two pump chambers," *Sensors and Actuators A: Physical*, no. 46–47, pp. 549–556, 1995.
- [17] L.-S. Jang and Y.-C. Yu, "Peristaltic micropump system with piezoelectric actuators," *Microsystem Technologies*, vol. 14, no. 2, pp. 241–248, August 2007.
- [18] Y.-C. Hsu, J.-L. Hsu, and N. B. Le, "An experimental and numerical investigation into the effects of the PZT actuator shape in polymethylmethacrylate (PMMA) peristaltic micropumps," *Microsystem Technologies*, vol. 15, no. 4, pp. 565–571, January 2009.
- [19] K. N. Bhat, A. Das Gupta, P. R. S. Rao, N. Das Gupta, E. Bhattacharya, K. Sivakumar, V. V. Kumar, L. H. Anitha, J. D. Joseph, S. P. Madhavi, and K. Natarajan, "Wafer bonding — A powerful tool for MEMS," *Indian Journal of Pure & Applied Physics*, vol. 45, pp. 311–316, April 2007.
- [20] a. Berthold, B. Jakoby, and M. J. Vellekoop, "Wafer-to-wafer fusion bonding of oxidized silicon to silicon at low temperatures," *Sensors Actuators A. Physical*, vol. 68, no. 1–3, pp. 410–413, June 1998.

- [21] J. S. Yoon and et al, "Studies on the performance characteristics and improvements of the piezoelectrically-driven micro gas compressors," *Microelectronic Engineering*, vol. 86, no. 11, pp. 2297–2304, November 2009.
- [22] K.-N. Chen, A. Fan, and R. Reif, "Microstructure examination of copper wafer bonding," *Journal of Electronic Materials*, vol. 30, no. 4, pp. 331–335, April 2001.
- [23] Y. T. Cheng, L. Lin, and K. Najafi, "Localized silicon fusion and eutectic bonding for MEMS fabrication and packaging," *Journal of Microelectromechanical System*, vol. 9, no. 1, pp. 3–8, March 2000.
- [24] C. Cabuz, W. R. Herb, and E. I. Cabuz, "The dual diaphragm pump," *Technical Digest. MEMS 2001. 14th IEEE International Conference on Micro Electro Mechanical Systems (Cat. No.01CH37090)*, pp. 519–522, 2001.
- [25] G. Fu, N. H. Loh, S. B. Tor, and B. Yen Tay, "Chapter 11 Metal Injection Molding at Micro-Scales (μ MIM)," *Micro-Manufacturing*, pp. 347–369, 2011.
- [26] M. Hecke and W. K. Schomburg, "Review on micro molding of thermoplastic polymers," *Journal of Micromechanics and Microengineering*, vol. 14, no. 3, pp. R1–R14, 2003.
- [27] J. Fahrenberg, W. Bier, D. Maas, W. Menz, R. Ruprecht, and W. K. Schomburg, "A microvalve system fabricated by thermoplastic molding," *Journal of Micromechanics and Microengineering*, vol. 5, no. 2, pp. 169–171, 1995.
- [28] D. M. Cao, J. Jiang, W. J. Meng, J. C. Jiang, and W. Wang, "Fabrication of high-aspect-ratio microscale Ta mold inserts with micro electrical discharge machining," *Microsystem Technologies*, vol. 13, no. 5–6, pp. 503–510, 2007.
- [29] G. Bissacco, H. N. Hansen, P. T. Tang, and J. Fugl, "Precision manufacturing methods of inserts for injection molding of microfluidic systems Technical University of Denmark," pp. 1–7, 2012.
- [30] V. Sharma, C. Science, T. Supervisor, and T. P. Orlando, "MEMS Micropump for a Micro Gas Analyzer," Massachusetts Institute of Technology, 2009.
- [31] H. Kim, W. H. Steinecker, S. Reidy, G. R. Lambertus, A. A. Astle, K. Najafi, E. T. Zellers, L. P. Bernal, P. D. Washabaugh, and K. D. Wise, "A micropump-driven high-speed mems gas chromatography system," in *TRANSDUCERS and EUROSENSORS '07 - 4th International Conference Solid-State Sensors, Actuators and Microsystems*, pp. 1505–1508, 2007.
- [32] Shannon, M. A., Philpott, M. L., Miller, N. R., Bullard, C. W., Beebe, D. J., Jacobi, A. M., and Rockett, A., "Integrated mesoscopic cooler circuits (IMCCS)," in *American Society of Mechanical Engineers, Advanced Energy Systems Division (Publication) AES*, vol. 39, pp. 75–82, 1999.
- [33] A. a Sathe, E. a Groll, and S. V. Garimella, "Analytical model for an electrostatically actuated miniature diaphragm compressor," *Journal of Micromechanics and Microengineering*, vol. 18, no. 3, p. 35010, March 2008.

- [34] A. Sathe, "Design Optimization of Electrostatically Actuated Miniature Compressors for Electronics Cooling," 2008.
- [35] A. A. Sathe, A. Bajaj, D. Peroulis, E. Groll, and S. Garimella, "Miniature-scale Diaphragm Compressor for Electronics Cooling," Purdue, 2008.
- [36] H. Kim, A. A. Astle, K. Najafi, L. P. Bernal, and P. D. Washabaugh, "An Integrated Electrostatic Peristaltic 18-Stage Gas Micropump With Active Microvalves," *Journal of Microelectromechanical Systems*, January, pp. 131–134, 2014.
- [37] J. S. Yoon, J. W. Choi, and M. S. Kim, "Computational and experimental investigation on the performance characteristics of the micro gas compressor," *Microelectronic Engineering*, vol. 86, no. 10, pp. 1975–1982, Oct. 2009.
- [38] S. Vanapalli, H. J. M. ter Brake, H. V. Jansen, Y. Zhao, H. J. Holland, J. F. Burger, and M. C. Elwenspoek, "High frequency pressure oscillator for microcryocoolers.," *Review of Scientific Instruments*, vol. 79, no. 4, p. 45103, April 2008.
- [39] R. Lewis, C. J. Coolidge, P. J. Schroeder, V. M. Bright, and Y. C. Lee, "Fabrication, assembly, and testing of a MEMS-enabled micro gas compressor for a 4:1 pressure ratio," *Sensors Actuators A. Physical*, vol. 190, pp. 84–89, February 2013.
- [40] R. Zengerle, A. Richter, and H. Sandmaier, "A micro membrane pump with electrostatic actuation," [1992] *Proceedings IEEE Micro Electro Mechanical Systems*, pp. 19–24, 1992.
- [41] K. Kumar and et al, "Transient Performance & Coupled Acoustic Structural & Electrostatic Modeling of a Multistage Vacuum Micropump," in *ASME 2011 International Mechanical Engineering Congress & Exposition IMECE2011*, vol. i, 2011.
- [42] A. A. Astle, "Analysis and Design of Multistage Electrostatically-Actuated Micro Vacuum Pumps," in *ASME International Mechanical Engineering Congress & Exposition*, pp. 477–486.
- [43] A. a. Sathe, E. a. Groll, and S. V. Garimella, "Dynamic analysis of an electrostatic compressor," *International Journal of Refrigeration*, vol. 33, no. 5, pp. 889–896, August 2010.
- [44] A. Besharatian, K. Kumar, R. L. Peterson, L. P. Bernal, and K. Najafi, "A Scalable, Modular, Multi-stage, Peristaltic, Electrostatic Gas Micro-pump," *Proceeding IEEE International Conference Micro Electro Mechanical System*, pp. 1001–1004, February 2012.
- [45] A. Besharatian, K. Kumar, R. L. Peterson, L. P. Bernal, and K. Najafi, "A scalable, modular, multi-stage, peristaltic, electrostatic gas micro-pump," University of Michigan, 2012.

- [46] S. Lee and et al, "Adaptive Gas Pumping by Controlled Timing of Active Microvalves in Peristaltic Micropumps," *IEEE Transaction on Transducer*, pp. 2294–2297, 2009.
- [47] L. Saggere, N. W. Hagood, D. C. Roberts, H.-Q. Li, J. L. Steyn, K. Turner, J. A. Carretero, O. Yaglioglu, Y.-H. Su, R. Mlcak, S. M. Spearing, K. S. Breuer, and M. A. Schmidt, "Design, fabrication, and testing of a piezoelectrically driven high flow rate micro-pump," *ISAF 2000. Proceedings of the 2000 12th IEEE International Symposium on Applications of Ferroelectrics (IEEE Cat. No.00CH37076)*, vol. 1, 2000.
- [48] D. G. Lee, S. W. Or, and G. P. Carman, "Design of a Piezoelectric-hydraulic Pump with Active Valves," *Journal of Intelligent Materials Systems and Structures*, vol. 15, no. 2, pp. 107–115, 2004.
- [49] K. Pharas and S. McNamara, "Bi-directional gas pump driven by a thermoelectric material," *Proceedings of the IEEE International Conference on Micro Electro Mechanical Systems (MEMS)*, vol. 125032, pp. 1103–1106, 2010.
- [50] S. An, N. K. Gupta, and Y. B. Gianchandani, "A Si-micromachined 162-stage two-part knudsen pump for on-chip vacuum," *Journal of Micromechanics and Microengineering*, vol. 23, no. 2, pp. 406–416, 2014.
- [51] S. McNamara and Y. B. Gianchandani, "On-Chip Vacuum Generated by a Micromachined Knudsen Pump," *Journal of Microelectromechanical Systems*, vol. 4, no. 14, 2005.
- [52] J. Liu, N. K. Gupta, X. Fan, K. D. Wise, and Y. B. Gianchandani, "A pressure programmable gas chromatography microsystem utilizing motionless Knudsen pump, fiber-integrated optical detector, and silicon micromachined separation column," *2011 16th International Solid-State Sensors, Actuators and Microsystems Conference, Transducer*, pp. 803–806, 2011.
- [53] K. H. Gilchrist, R. P. McNabb, J. a Izatt, and S. Grego, "Piezoelectric scanning mirrors for endoscopic optical coherence tomography," *Journal of Micromechanics and Microengineering*, vol. 19, no. 9, p. 95012, September 2009.
- [54] H. Kim and K. Najafi, "An electrically-driven, large-deflection, high-force, micro piston hydraulic actuator array for large-scale microfluidic systems," *Proceedings of the IEEE International Conference on Micro Electro Mechanical Systems (MEMS)*, pp. 483–486, 2009.
- [55] T. Ninomiya, Y. Okayama, Y. Matsumoto, X. Arouette, K. Osawa, and N. Miki, "MEMS-based hydraulic displacement amplification mechanism with completely encapsulated liquid," *Sensors and Actuators A. Physical*, vol. 166, no. 2, pp. 277–282, 2011.

- [56] J. L. Steyn, H. Q. Li, D. C. Roberts, K. T. Turner, O. Yaglioglu, Y. Su, M. Schmidt, S. M. Spearing, N. W. Hagood, and R. Mlcak, "Hydraulic Amplification Devices for Microscale Actuation," *Solid-State Sensor, Actuator and Microsystems Workshop*, pp. 50–53, 2002.
- [57] X. Yang, "A MEMS Valve for the MIT Microengine by," Massachusetts Institute of Technology, 2001.
- [58] D. Accoto, M. C. Carrozza, and P. Dario, "Modelling of micropumps using unimorph piezoelectric actuator and ball valves," *Journal of Micromechanics and Microengineering*, vol. 10, no. 2, pp. 277–281, June 2000.
- [59] B. Li, Q. Chen, D. G. Lee, J. Woolman, and G. P. Carman, "Development of large flow rate, robust, passive micro check valves for compact piezoelectrically actuated pumps," *Sensors and Actuators A. Physical*, vol. 117, no. 2, pp. 325–330, 2005.
- [60] M. Hu, H. Du, S.-F. Ling, Y. Fu, Q. Chen, L. Chow, and B. Li, "A silicon-on-insulator based micro check valve," *Journal of Micromechanics and Microengineering*, vol. 14, no. 3, pp. 382–387, March 2004.
- [61] W. Y. Sim, H. J. Yoon, O. C. Jeong, and S. S. Yang, "A phase-change type micropump with aluminum flap valves," *Journal of Micromechanics and Microengineering*, vol. 13, no. 2, pp. 286–294, March 2003.
- [62] B. Yang, G. C. Lopez, Q. Lin, and A. J. Rosenbloom, "Microfabricated PDMS Check Valves," *Microelectromechanical Systems*, pp. 369–372, 2003.
- [63] N.-T. Nguyen, T.-Q. Truong, C. Lee-ngo, KK Wong, SS Ho, and CLN Low, "Micro checkvalves for integration into polymeric microfluidic devices," *Journal of Micromechanics and Microengineering*, 2004.
- [64] M. Sadeghi, H. Kim, and K. Najafi, "Electrostatically driven micro-hydraulic actuator arrays," *Proceedings of the IEEE International Conference on Micro Electro Mechanical Systems (MEMS)*, pp. 15–18, 2010.
- [65] A. Doll, M. Wischke, H.-J. Schrag, A. Geipel, F. Goldschmidtboeing, and P. Woias, "Characterization of active silicon microvalves with piezoelectric membrane actuators," *Microelectronic Engineering.*, vol. 84, no. 5–8, pp. 1202–1206, 2007.
- [66] H. Q. Li, D. C. Roberts, J. L. Steyn, K. T. Turner, and O. Yaglioglu, "Fabrication of a microvalve with piezoelectric actuation," *Proceedings of the IEEE Micro Electro Mechanical Systems*, pp. 92–95, 2003.
- [67] S. Jeong, "How difficult is it to make a micro refrigerator?," *International Journal of Refrigeration*, vol. 27, no. 3, pp. 309–313, May 2004.
- [68] B.-Z. Maytal and J. M. Pfotenhauer, *Miniature Joule-Thomson Cryocooling*. New York, NY: Springer New York, 2013.

- [69] P. P. P. M. Lerou, H. Jansen, G. C. F. Venhorst, J. F. Burger, T. T. Veenstra, H. J. M. ter Brake, H. J. M. ter Brake, M. Elwenspoek, and H. Rogalla, "Progress in Micro Joule-Thomson Cooling at Twente University," in *Cryocoolers 13*, 2004.
- [70] P. P. P. M. Lerou, H. J. M. Ter Brake, J. F. Burger, H. J. Holland, and H. Rogalla, "Characterization of micromachined cryogenic coolers," *Journal of Micromechanics and Microengineering*, vol. 17, no. 10, pp. 1956–1960, October 2007.
- [71] P. P. P. M. Lerou, G. C. F. Venhorst, C. F. Berends, T. T. Veenstra, M. Blom, J. F. Burger, H. J. M. Ter Brake, and H. Rogalla, "Fabrication of a micro cryogenic cold stage using MEMS-technology," *Journal of Micromechanics and Microengineering*, vol. 16, no. 10, pp. 1919–1925, October 2006.
- [72] R. Lewis, M.-H. Lin, Y. Wang, J. Cooper, P. Bradley, R. Radebaugh, M. Huber, and Y. C. Lee, "Performance Analysis of an Integrated Micro Cryogenic Cooler and Miniature Compressor for Cooling to 200 K," *Journal of Thermal Science and Engineering Applications*, vol. 5, no. 3, p. 31003, June 2013.
- [73] J. H. Derking, C. H. Vermeer, T. Tirolien, M. R. Crook, and H. J. M. ter Brake, "A mixed-gas miniature Joule–Thomson cooling system," *Cryogenics*, vol. 57, pp. 26–30, October 2013.
- [74] J. Burger, "Cryogenic microcooling: a micromachined cold stage operating with a sorption compressor in a vapor compression cycle," University of Twente, 2001.
- [75] R. A. Y. Radebaugh, "Refrigeration for Superconductors," *Proceedings of the IEEE*, vol. 92, no. 10, pp. 1719–1734, 2004.
- [76] R. Lewis, B. A. Physics, and W. College, "Fluid Flow Effects on Micro Cryogenic Coolers with Mixed Refrigerant by," University of Colorado, 2012.
- [77] M. H. Lin, P. E. Bradley, H. J. Wu, J. C. Booth, R. Radebaugh, and Y. C. Lee, "Design, fabrication, and assembly of a hollow-core fiber-based micro cryogenic cooler," in *Solid-State Sensors, Actuators and Microsystems Conference, 2009 Transducer*, pp. 1114–1117, 2009.
- [78] D. Guo, A. J. H. Mcgaughey, G. K. Fedder, S. Yao, and M. Moran, "DESIGN AND EVALUATION OF MEMS-BASED STIRLING CYCLE MICRO-REFRIGERATION SYSTEM," in *ASME 2011 International Mechanical Engineering Congress & Exposition*, pp. 1–8, 2011.
- [79] E. Hong, S. Trolier-mckinstry, S. Member, R. L. Smith, S. V. Krishnaswamy, and C. B. Freidhoff, "Design of MEMS PZT Circular Diaphragm Actuators to Generate Large Deflections," *Journal of Microelectromechanical Systems*, vol. 15, no. 4, pp. 832–839, 2006.

- [80] K. Yao, W. Zhu, E. Uchino, Z. Zhang, and L. C. Lim, "Design and fabrication of a high performance multilayer piezoelectric actuator with bending deformation," *IEEE Transactions on Ultrasonics, Ferroelectrics, and Frequency Control*, vol. 46, no. 4, pp. 1020–7, January 1999.
- [81] I.-J. Cho, S. Jang, and H.-J. Nam, "A Piezoelectrically Actuated MEMS Speaker with Polyimide Membrane and Thin Film Pb(Zr,Ti)O₃(PZT) Actuator," *Integrated Ferroelectrics*, vol. 105, no. 1, pp. 27–36, August 2009.
- [82] K.-I. Park, J. H. Son, G.-T. Hwang, C. K. Jeong, J. Ryu, M. Koo, I. Choi, S. H. Lee, M. Byun, Z. L. Wang, and K. J. Lee, "Highly-Efficient, Flexible Piezoelectric PZT Thin Film Nanogenerator on Plastic Substrates," *Advance Materials*, February 2014.
- [83] Z. Shen, M. Olfatnia, J. Miao, and Z. Wang, "Displacement and resonance behaviors of a piezoelectric diaphragm driven by a double-sided spiral electrode," *Smart Materials and Structures*, vol. 21, no. 5, p. 55001, May 2012.
- [84] O. J. Myers, M. Anjanappa, and C. Freidhoff, "Designing Piezoelectric Interdigitated Microactuators Using Finite Element Analysis," *Journal of Mechanical Design*, vol. 132, no. 6, p. 61004, 2010.
- [85] A. Arevalo and I. G. Foulds, "Parametric Study of Polyimide – Lead Zirconate Titanate Thin Film Cantilevers for Transducer Applications," pp. 1–5, 2013.
- [86] E. Hong, S. Trolier-McKinstry, R. Smith, S. V. Krishnaswamy, and C. B. Freidhoff, "Vibration of micromachined circular piezoelectric diaphragms," *IEEE Transactions on Ultrasonics, Ferroelectrics, and Frequency Control*, vol. 53, no. 4, pp. 697–706, April 2006.
- [87] F. Dauchy and R. A. Dorey, "Patterned multilayer thick film electroceramic structures for micro electromechanical systems," *Multi-Material Micro Manufacture*, pp. 1–4, 2008.
- [88] M. Sayer, "Characterization of thick lead zirconate titanate films fabricated using a new sol gel based process," *Journal of Applied Physics*, vol. 81, no. 2, 2001.
- [89] P. K. Sekhar, "Process development and characterization of sol- gel lead zirconate titanate films for fabrication of flexural plate wave devices," 2005.
- [90] S. P. Beeby, A. Blackburn, and E. Al., "Processing of PZT piezoelectric thick films on silicon for microelectromechanical systems," *Journal of Micromechanics and Microengineering*, vol. 218, no. 9, 1999.
- [91] J. H. We, S. J. Kim, G. S. Kim, and B. J. Cho, "Improvement of thermoelectric properties of screen-printed Bi₂Te₃ thick film by optimization of the annealing process," *Journal of Alloys and Compounds*, vol. 552, pp. 107–110, 2013.
- [92] T. Hedegaard, T. Pedersen, E. V. Thomsen, R. Lou-Moeller, K. Hansen, and T. Zawada, "Screen printed thick film based pMUT arrays," *2008 IEEE Ultrasonics Symposium*, pp. 2126–2129, November 2008.

- [93] M. Allahverdi, A. Safari, and A. A. P. Z. T. T. Films, "Direct-Write of PZT Thick Films," in *Applications of Ferroelectrics: 2004. ISAF-04. 2004 14th IEEE International Symposium*, vol. 0, no. c, pp. 250–253, 2004.
- [94] X.-Y. Wang, C.-Y. Lee, Y.-C. Hu, W.-P. Shih, C.-C. Lee, J.-T. Huang, and P.-Z. Chang, "The fabrication of silicon-based PZT microstructures using an aerosol deposition method," *Journal of Micromechanics and Microengineering*, vol. 18, no. 5, p. 55034, May 2008.
- [95] J. Sun, M. Vittadello, E. K. Akdogan, a. Hall, N. M. Hagh, and a. Safari, "Direct-Write Deposition of PZT Thick Films Derived from Modified Sol-Gel Process," 2006 15th IEEE International Symposium on the Applications of Ferroelectrics, pp. 57–60, July 2006.
- [96] N. Futai, K. Matsumoto, and I. Shimoyama, "Fabrication of high-aspect-ratio PZT thick film structure using sol-gel technique and SU-8 photoresist," *Technical Digest: MEMS 2002 IEEE International Conference. Fifteenth IEEE International Conference on Micro Electro Mechanical Systems (Cat. No.02CH37266)*, no. 4, pp. 168–171, 2002.
- [97] R. a. Dorey, R. W. Whatmore, S. P. Beeby, R. N. Torah, and N. M. White, "Screen Printed PZT Composite Thick Films," *Integrated Ferroelectrics*, vol. 63, no. 1, pp. 89–92, January 2004.
- [98] R. Lou-Moeller, C. C. Hindrichsen, L. H. Thamdrup, T. Bove, E. Ringgaard, a. F. Pedersen, and E. V. Thomsen, "Screen-printed piezoceramic thick films for miniaturised devices," *Journal of Electroceramics*, vol. 19, no. 4, pp. 333–338, March 2007.
- [99] R. Maas, M. Koch, N. R. Harris, N. M. White, and A. G. R. Evans, "Thick-film printing of PZT onto silicon," April 1996.
- [100] M. Sauer, S. Meilchen, A. Kalleder, M. Mennig, and H. Schmidt, "Screen printing," *Sol-Gel Technologies for Glass Producers and Users*, pp. 117–122, 2004.
- [101] J. Akedo, S. Nakano, J. Park, S. Baba, and K. Ashida, "The aerosol deposition method," *Synthesiology English edition.*, vol. 1, no. 2, pp. 121–130, 2008.
- [102] C. Mo, R. Wright, W. S. Slaughter, and W. W. Clark, "Behaviour of a unimorph circular piezoelectric actuator," *Smart Materials and Structures*, vol. 15, no. 4, pp. 1094–1102, August 2006.
- [103] M. Herz, D. Horsch, G. Wachutka, T. C. Lueth, and M. Richter, "Design of ideal circular bending actuators for high performance micropumps," *Sensors and Actuators A. Physical*, vol. 163, no. 1, pp. 231–239, September 2010.

- [104] M. Deshpande and L. Saggere, "An analytical model and working equations for static deflections of a circular multi-layered diaphragm-type piezoelectric actuator," *Sensors and Actuators A Physical*, vol. 136, no. 2, pp. 673–689, May 2007.
- [105] J. L. Livesey, "Inertia effects in viscous flows," *International Journal of Mechanical Sciences*, vol. 1, pp. 84–88, 1959.
- [106] A. F. Elkouh, "Inertia Effect in Laminar Radial Flow between Parallel Plates," *International Journal of Mechanical Sciences*, pp. 253–255, 1967.
- [107] B. J. Kirby, "Hydraulic Circuit Analysis," in *Micro- and Nanoscale Fluid Mechanics. Transport in Microfluidic Devices*, pp. 60–78, 2013.
- [108] a Doll, M. Heinrichs, F. Goldschmidtboeing, H. Schrag, U. Hopt, and P. Woias, "A high performance bidirectional micropump for a novel artificial sphincter system," *Sensors and Actuators A: Physical*, vol. 130–131, pp. 445–453, 2006.
- [109] S. Chung and S. Park, "Effects of temperature on mechanical properties of SU-8 photoresist material," *Journal of Mechanical Science and Technology*, vol. 27, no. 9, pp. 2701–2707, 2013.
- [110] J. Ulrich and R. Zengerle, "Static and dynamic flow simulation of a KOH-etched microvalve using the finite-element method," *Sensors and Actuators A: Physical*, vol. 53, pp. 379–385, 1996.
- [111] M. Koch et al, "Coupled FEM simulation for the characterization of the fluid flow within a micromachined cantilever valve," *Journal of Micromechanics and Microengineering*, vol. 6, no. 1, 1996.
- [112] X.-Q. Wang, Q. L. Q. Lin, and Y.-C. T. Y.-C. Tai, "A Parylene micro check valve," *Technical Digest. IEEE International MEMS 99 Conference. Twelfth IEEE International Conference on Micro Electro Mechanical Systems (Cat. No.99CH36291)*, vol. 93, 1999.
- [113] M. N. Srinivas and C. Padmanabhan, "Computationally efficient model for refrigeration compressor gas dynamics," *International Journal of Refrigeration*, vol. 25, no. 8, pp. 1083–1092, 2002.
- [114] R. A. Habing, "Flow and Plate Motion in Compressor Valves," University of Twente, 2005.
- [115] J. F. T. Maclaren, "Review of Simple Mathematical Models of Valves in Reciprocating Compressors," *International Compressor Engineering Conference*, Purdue University, 1972.
- [116] H. Bukac, "Understanding Valve Dynamics," *International Compressor Engineering Conference*, p. 1564, 2002.

- [117] a Geipel, a Doll, P Jantscheff, N. Esser, U. Massing, P. Woias, and F Goldschmidtboeing, "A novel two-stage backpressure-independent micropump: modeling and characterization," *Journal of Micromechanics and Microengineering*, vol. 17, no. 5, pp. 949–959, May 2007.
- [118] S. Le, "Active vibration control of a flexible beam," San Jose State, 2009.
- [119] T. Jordan, Z. Ounaies, J. Tripp, and P. Tcheng, "Electrical Properties and Power Considerations of a Piezoelectric Actuator," pp. 0–8, 2000.
- [120] M. R. Hart, R. A. Conant, K. Y. Lau, and R. S. Muller, "Stroboscopic interferometer system for dynamic MEMS characterization," *Journal of Microelectromechanical Systems*, vol. 9, no. 4, pp. 409–418, 2000.
- [121] W.-J. Lin, J. P. Khatait, W. Lin, and H. Li, "Modelling of an Orifice-type Aerostatic Thrust Bearing," *Proceedings of the 9th International Conference on Control, Automation, Robotics and Vision*, pp. 1–6, 2006.
- [122] J. P. Khatait and W. J. Lin, "Design of orifice-type aerostatic thrust bearing," SIMTech technical reports, vol. 6, no. 1, pp. 7-12, January 2005.
- [123] S.B.Savage, "Laminar Radial Flow between Parallel Plates," *Journal of Applied Mechanics*. 1964.
- [124] S. K. Padhy and S. N. Dwivedi, "Inertia Effect of the Fluid Particles on the Lubricant Flow in a Dynamic Thrust Bearings," *International Compressor Engineering Conference*, Purdue University, 1992.
- [125] S. I. En Lin, "Investigation on packaging parameters of a circular multi-layered diaphragm-type piezoelectric actuator," *Computers & Structures*, vol. 89, no. 3–4, pp. 371–379, February 2011.